Experimental Nonlinear Dynamics and Snap-Through of Post-Buckled Thin Laminated Composite Plates

Han-Gyu Kim

A thesis
submitted in partial fulfillment of the
requirements for the degree of

Master of Science in Civil Engineering

University of Washington

2017

Supervisory Committee:

Richard Wiebe, Chair

Gregory R. Miller

I. Y. (Steve) Shen

Mark E. Tuttle

Program Authorized to Offer Degree:
Civil and Environmental Engineering

University of Washington

Abstract

Experimental Nonlinear Dynamics and Snap-Through of Post-Buckled Thin Laminated Composite Plates

Han-Gyu Kim

Chair of the Supervisory Committee:
Richard Wiebe
Civil and Environmental Engineering

Modern aerospace systems are increasingly being designed with composite panels and plates to achieve light weight and high specific strength and stiffness. For constrained panels, thermally-induced axial loading may cause buckling of the structure, which can lead to nonlinear and potentially chaotic behavior. When post-buckled composite plates experience snap-through, they are subjected to large-amplitude deformations and in-plane compressive loading. These phenomena pose a potential threat to the structural integrity of composite structures.

In this work, the nonlinear dynamic behavior of post-buckled composite plates was investigated experimentally and computationally. For the experimental work, an electrodynamic shaker was used to apply harmonic loads and the dynamic response of plate specimens was measured using a single-point displacement-sensing laser, a double-point laser vibrometer (velocity-sensing), and a set of digital image correlation cameras. Both chaotic and periodic steady-state snap-through behaviors were investigated. The experimental data were used to characterize snap-through behaviors of the post-buckled specimens and their boundaries in the harmonic forcing parameter space.

The nonlinear behavior of post-buckled plates was modeled using the classical laminated plate theory (CLPT) and the von Kármán strain-displacement relations. The static equi-

librium paths of the post-buckled plates were analyzed using an arc-length method with a branch-switching technique. For the dynamic analysis, the nonlinear equations of motion were derived based on CLPT and the nonlinear finite element model of the equations was constructed using the Hermite cubic interpolation functions for both conforming and non-conforming elements. The numerical analyses were conducted using the model and were compared with the experimental data.

TABLE OF CONTENTS

Page

List of Figures iii

Chapter 1: Introduction 1
1.1 Overview 1
1.2 Motivation 2
1.3 Nonlinear dynamics 5

Chapter 2: Nonlinear Equations of Motion and Finite Element Model using Classical Laminated Plate Theory 8
2.1 Introduction 8
2.2 Lamina and laminate constitutive relations 10
2.3 Kirchhoff hypothesis and von Kármán strains 13
2.4 Nonlinear equations of motion in CLPT 18
2.5 Nonlinear Finite Element Model of CLPT 25
2.6 Summary 34

Chapter 3: Experiment of Snap-Through of Post-Buckled Thin Laminated Composite Plates 35
3.1 Introduction 35
3.2 Fabrication of Laminated Composite Plate Specimens 36
3.3 Evaluation and verification of material properties 38
3.4 Exploratory investigation of snap-through boundaries 48
3.5 Full-field measurement of the nonlinear dynamic response of a post-buckled plate 53
3.6 Summary 72

Chapter 4: Modeling of Snap-Through of Post-Buckled Thin Laminated Composite Plates 75

4.1 Introduction . . . 75
4.2 High-precision cubic Hermite elements . . . 76
4.3 Solution methods for the nonlinear static analysis of post-buckled plates . . . 81
4.4 Nonlinear static analysis of post-buckled plates: conforming elements . . . 84
4.5 Solution method for the nonlinear dynamic analysis of post-buckled plates . 91
4.6 Nonlinear dynamic analysis of post-buckled plates: conforming elements . . . 94
4.7 Nonlinear dynamic analysis of post-buckled plates: nonconforming elements . 101
4.8 Summary . . . 111

Chapter 5: Comparison of Experimental Data and Modeling Results . . . 112
5.1 Introduction . . . 112
5.2 Vibrometer: frequency-sweep experiments . . . 112
5.3 Model: forcing amplitude-ramp analyses . . . 116
5.4 Model: forcing frequency-sweep analyses . . . 119
5.5 Comparison of snap-through boundaries . . . 126

Chapter 6: Summary and Future Work . . . 130
6.1 Summary . . . 130
6.2 Future work . . . 132

Bibliography . . . 135

LIST OF FIGURES

1.1 Composite material applications in the aerospace and civil engineering industries. . . . 3

1.2 SR-71 Blackbird and the buckled surface on the underside of its wing after several high speed flights. . . . 4

1.3 Nonlinear dynamic response of bi-stable systems. . . . 6

1.4 Harmonic loading input and corresponding chaotic response output. . . . 7

2.1 Coordinate system and dimensions of plates. . . . 9

2.2 Specially and generally orthotropic laminae. . . . 10

2.3 Coordinate system on the curved boundary. . . . 19

2.4 Real and reference elements for isoparametric mapping. . . . 33

3.1 In-house fabrication of laminated composite plates in the Composites Lab at the University of Washington. . . . 37

3.2 *UW plate* and *AFRL plate* specimens. . . . 38

3.3 Plain weave prepreg TORAYCA T800H-6K/3900-2 (BMS 8-276). . . . 39

3.4 A symmetric laminate consisting of n unidirectional laminae and its corresponding weave lamina. . . . 40

3.5 Tensile load test using an Instron 5585H and an extensometer. . . . 43

3.6 Experimental setup of the static cantilever test. . . . 44

3.7 Modeling results of the static cantilever test. 45

3.8 Load vs. transverse displacement curves from the experimental data and modeling results. 46

3.9 Free vibration test results. 47

3.10 Experimental setup in the UW Lab. 49

3.11 Boundary conditions of the specimen, the UW plate. 49

3.12 Buckling process and measurement of axial loads with a load cell. 50

3.13 Dynamic response under 105 Hz harmonic loading. 51

3.14 Snap-through boundaries under 105 Hz harmonic loading: (↑) indicates the boundaries found while increasing the loading amplitude while (↓) indicates the ones observed while decreasing the amplitude. 52

3.15 Snap-through boundaries in the harmonic forcing parameter space (loading amplitude vs. loading frequency): (↑) indicates the boundaries found while increasing the loading amplitude while (↓) indicates the ones observed while decreasing the amplitude. 53

3.16 Experimental setup for the full-field measurement. 55

3.17 Equipment employed for the full-field measurement. 55

3.18 DIC controller screens: digital images of the specimen taken by the two cameras (top pictures) and sampling points on the images (bottom pictures). . . 56

3.19 Static full-field measurement of the buckled shape of the specimen. 57

3.20 Superposition of the specimen plate (pink line), 95 sampling points on the plate (blue empty circles), and 4 sampling points on the clamp (cyan-filled circles) for the dynamic full-field measurement. 58

3.21 Full-field measurement of the dynamic response of the specimen subjected to harmonic loading. 59

3.22 Transverse displacement of the midpoint (sampling point number 51 in Figure 3.20) w_{mid} subjected to 5 g-85 Hz harmonic loading. 60

3.23 State-space of the midpoint subjected to 5 g-85 Hz harmonic loading. 61

3.24 Chaotic dynamic response of the plate subjected to 5 g-85 Hz harmonic loading and snapshots of corresponding interpolated deflected shapes. 63

3.25 w_{mid} subjected to 7 g-75 Hz harmonic loading. 64

3.26 State-space of the midpoint subjected to 7 g-75 Hz harmonic loading. 64

3.27 w_{mid} subjected to 4 g-180 Hz harmonic loading. 65

3.28 State-space of the midpoint subjected to 4 g-180 Hz harmonic loading. . . . 66

3.29 Vibrometer sampling point on the specimen surface. 67

3.30 Harmonic forcing amplitude 5 g vs. time. 67

3.31 Stepped forcing frequencies of the frequency-sweep experiment (5 g). 68

3.32 Measured velocity and integrated displacement of the frequency-sweep experiment (5 g). 69

3.33 Numerically integrated displacement shifted by removing the drift from Figure 3.32b. The buckled depth is demarcated as red dotted lines and the data points exceeding the buckled depth are colored as purple. 69

3.34 Snap-through boundary of 5 g forcing amplitude in the harmonic forcing parameter space. 70

3.35 Displacement of the vib-point measured by the vibrometer (w_{vibro}) when the plate was subjected to 5 g-85 Hz harmonic forcing. The red dotted lines indicate the buckled depth of the vib-point. 71

3.36 Comparison between the data of 5 g-85 Hz harmonic forcing collected by the vibrometer (w_{vibro}) and by the DIC cameras (w_{DIC}) simultaneously. The red dotted lines in the top figure indicate the buckled depth of the vib-point. . . 72

3.37 Comparison between the data of 7 g-75 Hz harmonic forcing collected by the vibrometer and by the DIC cameras simultaneously. 73

3.38 Comparison between the data of 4 g-180 Hz harmonic forcing collected by the vibrometer and by the DIC cameras simultaneously. 74

4.1 Conforming elements and transverse nodal variables. 77

4.2 Visualization of Hermite interpolation functions at node 1 ($(\xi, \eta) = (-1, -1)$). 78

4.3 Nonconforming elements and transverse nodal variables. 79

4.4 FEM mesh for the modeling plate with 231 nodes and 200 rectangular elements. 86

4.5 Equilibrium path of the initially-flat modeling plate under distributed axial loading. $\lambda = 1$ corresponds to the axial load for the first buckling mode, 695.5 N/m. 86

4.6 Equilibrium path and snapshots of corresponding deflected shapes of the post-buckled modeling plate (1 mm). 88

4.7 Equilibrium path and snapshots of corresponding deflected shapes of the post-buckled modeling plate (2 mm). 90

4.8 Comparison of the buckled shapes between the DIC reconstruction of the AFRL plate and the conforming element model of the modeling plate (the CF model). 97

4.9 w_{mid} and snapshots of corresponding deflected shapes when the CF model was subjected to 4 g-75 Hz harmonic loading. 98

4.10 w_{mid} and snapshots of corresponding deflected shapes when the CF model was subjected to 8 g-75 Hz harmonic loading. 99

4.11 w_{mid} and snapshots of corresponding deflected shapes when the CF model was subjected to 10 g-75 Hz harmonic loading. 100

4.12 FEM mesh for the NCF model with 242 nodes and 210 elements. The narrow elements consisting of the nodes number 221 to 242 are enlarged in Figure 4.13.101

4.13 Enlarged mesh of the edge of the initially-flat and buckled NCF models. . . . 102

4.14 Superposition of the clamp (grey block) and the deformed free edge. 103

4.15 Comparison of the buckled shapes between the DIC reconstruction of the AFRL plate and the NCF model. 105

4.16 Superposition of the buckled shapes of the AFRL plate and NCF model. . . 106

4.17 Cross-section view of the superposition shown in Figure 4.16. The circles are the positions of the nodes on the cross sections while the lines indicate buckled depth of the nodes. The blue lines are the cross sections of the DIC measurement of the AFRL plate while the red lines are the cross sections of the NCF model. The numbers written around the nodes indicate the discrepancy as a percentage (%). 107

4.18 Dynamic response of the midpoint when the NCF model was subjected to the harmonic forcing (amplitude-ramp from 2 g- to 5.2 g-85 Hz). 108

4.19 Enlarged chaotic snap-through part of Figure 4.18 and snapshots of corresponding deflected shapes. 109

4.20 Enlarged nearly periodic snap-through part of Figure 4.18 and snapshots of corresponding deflected shapes. 110

5.1 Response of the vib-point (w_{vib}) when 2 g harmonic loading was applied. . . 113

5.2 Response of the vib-point (w_{vib}) when 3 g harmonic loading was applied. . . 113

5.3 Response of the vib-point (w_{vib}) when 4 g harmonic loading was applied. . . 113

5.4 Response of the vib-point (w_{vib}) when 5 g harmonic loading was applied. . . 114

5.5 Response of the vib-point (w_{vib}) when 6 g harmonic loading was applied. . . 114

5.6 Response of the vib-point (w_{vib}) when 7 g harmonic loading was applied. . . 114

5.7 Snap-through boundaries of the post-buckled AFRL plate in the harmonic forcing parameter space. 115

5.8 Response of the NCF model for 1.6 g- to 2.6 g-60 Hz harmonic loading. . . . 117

5.9 Response of the NCF model for 1.8 g- to 3.2 g-90 Hz harmonic loading. . . . 117

5.10 Response of the NCF model for 2.8 g- to 4.4 g-110 Hz harmonic loading. . . 118

5.11 Response of the NCF model for 3 g- to 3.8 g-120 Hz harmonic loading. . . . 118

5.12 Response of the NCF model for 5.8 g- to 7.6 g-180 Hz harmonic loading. . . 119

5.13 Response of the NCF model for 2 g-50 Hz to -160 Hz harmonic loading. . . . 120

5.14 Response of the NCF model for 2.5 g-50 Hz to -135 Hz harmonic loading. . . 120

5.15 Response of the NCF model for 3 g-50 Hz to -155 Hz harmonic loading. . . . 121

5.16 Response of the NCF model for 3.5 g-50 Hz to -130 Hz harmonic loading. . . 121

5.17 Response of the NCF model for 4 g-50 Hz to -150 Hz harmonic loading. . . . 122

5.18 Response of the NCF model for 4.5 g-50 Hz to -65 Hz harmonic loading. . . 122

5.19 Response of the NCF model for 5 g-50 Hz to -80 Hz harmonic loading. . . . 123

5.20 Response of the NCF model for 5.5 g-50 Hz to -100 Hz harmonic loading. . . 123

5.21 Response of the NCF model for 6 g-50 Hz to -75 Hz harmonic loading. . . . 124

5.22 Response of the NCF model for 6.5 g-50 Hz to -70 Hz harmonic loading. . . 124

5.23 Response of the NCF model for 7 g-50 Hz to -70 Hz harmonic loading. . . . 125

5.24 Superposition of the snap-through points observed from the forcing amplitude-ramp simulations and the experimental snap-through boundaries. 126

5.25 Superposition of the snap-through points observed from the forcing frequency-sweep simulations and the experimental snap-through boundaries. 127

5.26 Comparison of the experimental and modeled snap-through boundaries. . . . 127

6.1 3-D CT scan system and scanned delamination. 134

ACKNOWLEDGMENTS

I would first like to thank Professor Richard Wiebe for all his great support and guidance, which was essential to the completion of this work. It has been my fortune and pleasure to work with him and he showed a perfect example of both a researcher and an adviser. I would also like to thank my committee members, Professors Gregory R. Miller, I. Y. (Steve) Shen, and Mark E. Tuttle for their valuable insights and suggestions on this work.

I would like to express my gratitude to Dr. S. Michael Spottswood for granting access to the Air Force Research Laboratory (AFRL) equipment and giving helpful suggestions, and to Dr. David A. Ehrhardt and Dr. Ricardo A. Perez for their support for experimental data acquisition at AFRL.

I would like to thank Michelle Hickner for her support at the Composites Lab, Bill Kuykendall for his help in operating the Instron machine, and Nasser Marafi for his help in running Hyak. I would also like to thank our research group, Pavel F. Babuska, Smit Kamal, Chi-Pu Lin, and Tianye Yang for their help at the Structural Vibrations Lab and having been great research colleagues, and my friends and colleagues, Kamal A. Ahmed, Carson G. Baker, Solomon A. Haile, Minyong Lee, Huy Si Nguyen, Kristina Tsvetanova, and Andrew O. Winter for their great help through my thesis program.

I would like to extend my thanks to Professors Sung-Uk Choi, JunHwan Lee, Sang-Ho Lee, Yun Mook Lim, and Hong-Gyoo Sohn at Yonsei University for their support for and advice on my academic career decision.

Finally, I would like to thank my lovely family and my wonderful wife, Jieun for their understanding, support, and love.

DEDICATION

to my parents, Heesung and Kwisook, and to my wife, Jieun

Chapter 1

INTRODUCTION

1.1 Overview

The primary focus of this work is the characterization of dynamic snap-through of post-buckled thin laminated composite plates under harmonic loads. Snap-through behaviors can be categorized as chaotic and periodic snap-through [1, 2, 3, 4]. When a post-buckled plate is subjected to a relatively small amplitude harmonic loading, the plate oscillates around one of its stable equilibria (i.e., a single-well response). As the forcing amplitude increases, the plate begins to show chaotic snap-through behavior (i.e., a cross-well response) and with a further increase in the load, the response shifts to periodic snap-through. The first and second thresholds are labeled chaotic and periodic snap-through boundaries, respectively [1, 3, 4, 5, 6, 7].

Chapter 2 introduces lamina and laminate constitutive relations and develops nonlinear equations of motion using the classical laminated plate theory (CLPT) and von Kármán strains. To solve those coupled equations, a nonlinear finite element model (FEM) was constructed using the Hermite cubic interpolation functions as discussed in Chapter 4. Using the model, the static equilibrium paths of post-buckled plates were found for the cases of both shallow and deep arches. In those analyses, an arc-length method and a branch-switching technique were adopted. For the dynamic analysis, the Newmark-beta method was applied to the nonlinear FEM in conjunction with the Newton-Raphson method for intra-time step

solving.

Chapter 3 describes the in-house fabrication of laminated composite plate specimens and the process of validating the material properties of the specimens. Then, an exploratory experiment investigating the nonlinear dynamics of a post-buckled plate using a single-point displacement-sensing laser is introduced. Since the full-field measurement of the buckled and deflected shapes of the specimen could not be obtained from the experiment, the data collected from the exploration was not used for modeling; however, the analysis of the experiment demonstrates the important characteristics of the snap-through boundaries of the post-buckled plate specimen. Subsequently, another set of experimental data obtained using a laser vibrometer (velocity-sensing) and a set of digital image correlation (DIC) cameras are analyzed. The full-field measurement of the buckled shape and nonlinear dynamic behaviors of a post-buckled specimen was obtained using a DIC technique. In addition, the snap-through boundary of the specimen was investigated using the data collected by the vibrometer. In Chapter 5, the experimental data are compared with the numerical analysis results of the nonlinear FEM.

1.2 Motivation

There are two key topics in this work: (i) laminated composite plates, and (ii) nonlinear dynamics and snap-through of post-buckled plates. In this section, the motivations behind the selection of these topics are introduced.

1.2.1 Composite material applications

The industrial applications of composite materials have grown significantly during the last half century due to their high strength and low density [10]. The Boeing 787, which is the first commercial airliner having a composite fuselage and composite wings, is a compelling example of the structural application of composite materials in the aerospace industry. As shown in Figure 1.1a, fifty percent of its primary structures, including the fuselage and

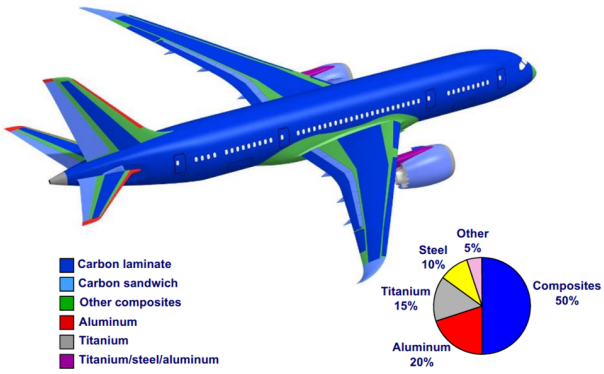

(a) Boeing 787 Dreamliner (photo courtesy of Boeing Company [8]).

(b) Carbon-fiber composite application to a bridge repair (photo courtesy of StablWall [9]).

Figure 1.1: Composite material applications in the aerospace and civil engineering industries.

wings, is made up of carbon fiber reinforced polymer (CFRP) [11]. This design has led to a 20 percent reduction of weight and a 30 percent reduction in airframe maintenance costs [8]. In the civil engineering industry, all-composite bridge deck systems are currently available and fiber reinforced polymer (FRP) is being used for rehabilitation of old bridges (Figure 1.1b) and as tendons for prestressed concrete structures [12].

Despite the increasing demands for and applications of the composite structures, their failure mechanisms are still difficult to determine in many applications. Considerable efforts to develop accurate failure theories of composites and to prove their validity have been made in the so-called World Wide Failure Exercise (WWFE-I: 1996-2004, WWFE-II: 2007-2013, and WWFE-III: 2013-Present); however, no composite material failure criteria are making accurate predictions of damage and failure of composite materials, and a global consensus about the validity of the leading theories has yet to be reached [11, 13]. Thus, the investigation of micro- and macro-mechanics of composite materials is still regarded as a challenging research area.

(a) SR-71 Blackbird.

(b) Permanently buckled surface panel on the underside of the wing of a SR-71 Blackbird (photo courtesy of the United States Air Force).

Figure 1.2: SR-71 Blackbird and the buckled surface on the underside of its wing after several high speed flights.

1.2.2 Nonlinear dynamics and snap-through of post-buckled plates

For constrained panels, thermally-induced axial loading such as aerodynamic heating during flight may cause buckling of those panels [14, 15]. For example, it was observed that after its multiple high-temperature flights due to Mach 3 speed, an SR-71 Blackbird (Figure 1.2a) had permanently buckled surface panels on the underside of its wing due to the deformation of the structure as shown in Figure 1.2b. It had remained uncertain for a long time whether such post-buckled panels as observed on the SR-71 exhibit snap-through during high speed flights. A research team at the Air Force Research Laboratory, however, recently succeeded in observing dynamic snap-through of a thermally buckled alloy steel plate inside a Mach 2 wind tunnel [16, 17].

When such post-buckled composite plates experience snap-through, they are subjected to large-amplitude deformations and significant in-plane compressive loading. These phenomena pose a potential threat to the structural integrity of composite structures; for example, axial compression may accelerate delamination growth which can lead to loss of global sta-

bility [18]. Delamination, which appears as a debonding of adjacent layers in laminated composites, is a very important failure mode in composite laminates [11] and one of the most frequently occurring failures of laminated composite structures [19]. In addition, snap-through makes abrupt curvature changes, which possibly lead to a considerable decrease in fatigue life [1, 2]. Therefore, understanding the post-buckled behavior of composite structures and the circumstances where the snap-through is likely to occur can be a pivotal step to guarantee the safety of these structures.

1.3 Nonlinear dynamics

Nonlinear systems possess distinctive characteristics which are not observed in familiar linear systems. In this section, some of the characteristics of nonlinear dynamics systems relevant to this work are discussed.

1.3.1 Single-well and cross-well responses of bi-stable systems

A post-buckled structure can demonstrate nonlinear and potentially chaotic behavior, including snap-through between its stable equilibria as shown in Figure 1.3a. The characteristics of the bi-stability of such post-buckled structure are illustrated on the energy plot of Strogatz [20] in Figure 1.3b, where there are two basins of attraction around the two stable equilibria. With a small energy input (i.e., a small amplitude loading), the system oscillates around the equilibrium in one of the basins. That oscillation can be plotted as a single-well response on the phase plane. With a larger energy input, the response may move to the other basin and oscillate around the other stable equilibrium within the basin. For a very large energy input, the response travels above the two basins and continuously oscillates between the two stable equilibria. This response can be observed as periodic snap-through (i.e., a cross-well response).

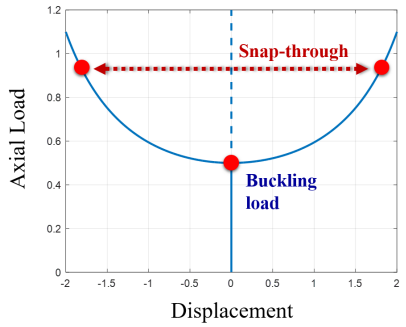

(a) Equilibirum path of a bi-stable post-buckled structure.

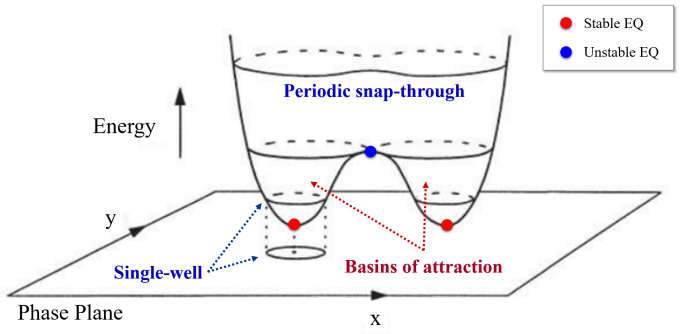

(b) Energy contour and phase plane of bi-stable system. The describtions are illustrated on the energy contour plot courtesy of Strogatz [20]. EQ on the legend denotes equilibrium.

Figure 1.3: Nonlinear dynamic response of bi-stable systems.

1.3.2 Chaotic response and post-buckled snap-through

Linear systems under harmonic loading generate harmonic response having the frequency same as the loading frequency with a phase shift. On the other hand, nonlinear systems under harmonic loading can generate non-harmonic response with the frequency different from the loading frequency. Chaotic response is a representative example of such phenomenon. One of the degrees of freedom of a post-buckled specimen with bi-stable equilibria may oscillate within one of the two basins (i.e., a single-well response in Figure 1.3b) over short time spans, occasionally jumping to the other basin (i.e., a cross-well response), which is observed as snap-through. The average frequency of the chaotic snap-through is typically lower (and unpredictable) than persistent periodic snap-through.

The experimental observation of this phenomenon is shown in Figure 1.4, which was obtained from an experiment of a post-buckled plate specimen in the Structural Vibrations Lab at the University of Washington. The transverse displacement degree of freedom of the midpoint of the specimen had two stable equilibria approximately at +1.1 and -1.1 mm as shown in Figure 1.4b. The 14.3 g-105 Hz harmonic loads (Figure 1.4a) which were inertially applied to the specimen generated the chaotic response of the degree of freedom

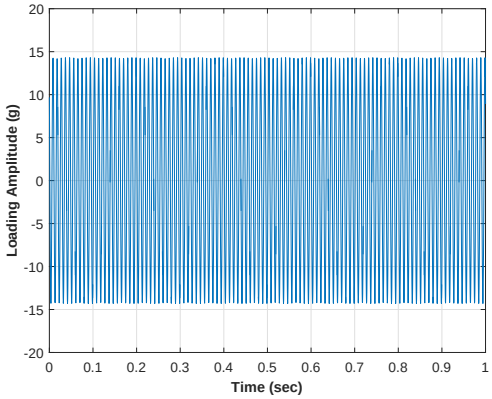

(a) Time-loading amplitude plot of a 14.3 g-105 Hz harmonic loading input.

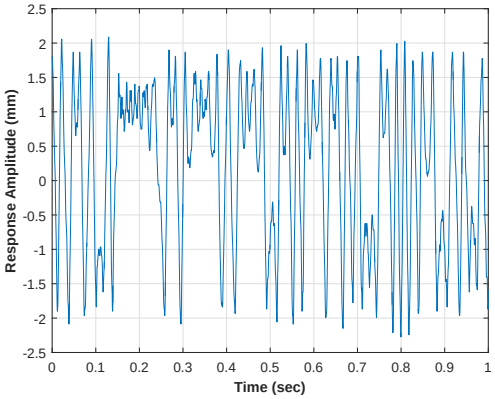

(b) Time-response amplitude of a chaotic output corresponding to the input in Figure 1.4a. The response was observed from oscillation of the mid-point of the specimen.

Figure 1.4: Harmonic loading input and corresponding chaotic response output.

with intermittent snap-through as shown in Figure 1.4b.

Chapter 2

NONLINEAR EQUATIONS OF MOTION AND FINITE ELEMENT MODEL USING CLASSICAL LAMINATED PLATE THEORY

2.1 Introduction

The structural behaviors of plates have been investigated by many well-known researchers. For static analysis, Timoshenko presented robust analytic analyses of various shapes of both isotropic and anisotropic plates in his monograph [21]. Whitney further developed theories on anisotropic plates in [22]. Regarding dynamic analysis, Leissa, in collaboration with National Aeronautics and Space Administration (NASA), reviewed and analyzed various analytic solutions for linear dynamic behaviors of isotropic plates in [23]. Chia exhaustively discussed the nonlinear static and dynamic behaviors of both isotropic and anisotropic plates in [24]. Although many new works have been added since these works were published, most of current researches still rely on these classical developments.

Many different types of laminated composite plate theories have been proposed or discussed in the literature, such as the classical laminated plate theory (CLPT), first-order shear deformation theory (FSDT), higher-order shear deformation theories (HOSDTs), and layerwise theory (LT) [10]. Reddy comprehensively explored linear and nonlinear static and dynamic response of these theories in [25], where he categorized the first three as the equivalent single layer (ESL) plate theories and the last one as the three-dimensional (3-D) elasticity theory. Following his description, the ESL plate theories make assumptions for the kinematics of deformation or the stress states along the thickness of plates and then reduce

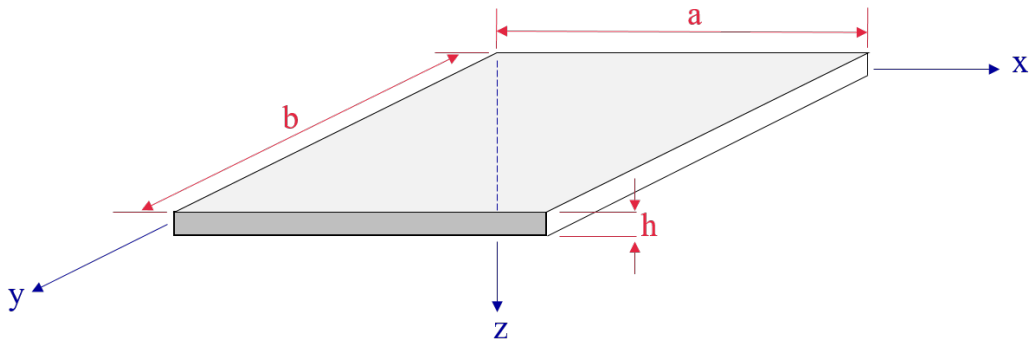

Figure 2.1: Coordinate system and dimensions of plates.

a 3-D problem to a two-dimensional (2-D) one based on the 3-D elasticity theory.

CLPT is based on the Kirchhoff plate hypothesis and some of its major assumptions are [11]:

- The thickness h of the plate is much smaller than the length along plate edges, a and b. The dimensions of plates are illustrated in Figure 2.1.
- The displacements u, v, and w are small compared with h.
- The in-plane strains ε_{xx}, ε_{yy}, and γ_{xy} are small compared with unity.
- The transverse shear strains (γ_{xz} and γ_{yz}) and the transverse normal strain (ε_{zz}) are negligible.
- The transverse shear stresses τ_{xz} and τ_{yz} vanish on the plate surface.

One of the key limitations of CLPT is the disregard of interlaminar stresses (τ_{xz}, τ_{yz}, σ_{zz}) that are responsible for delamination which is an important failure mode in composite structures. Interlaminar stresses of CLPT, however, may be computed using the equilibrium equations of 3-D elasticity [11, 25].

FSDT allows the computation of interlaminar shear stresses directly through constitutive equations; however, the stresses do not match in general those derived from equilibrium while HOSDTs can yield more accurate interlaminar stress distribution although they require considerably more computational effort [25]. Thus, despite the advantages of other theories,

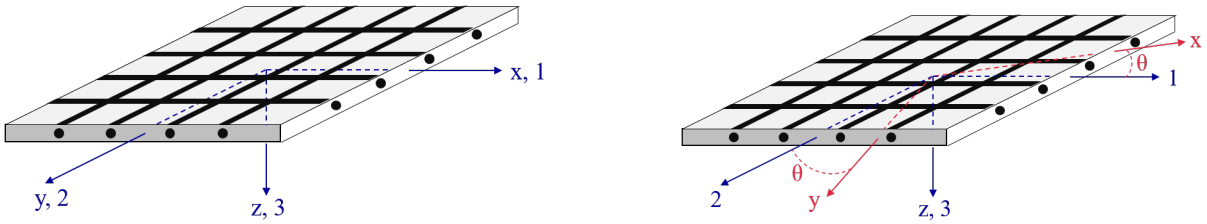

(a) Specially orthotropic lamina.

(b) Generally orthotropic lamina.

Figure 2.2: Specially and generally orthotropic laminae.

CLPT is still frequently preferred to model behaviors of thin laminated composite plates since their global response can often be accurately determined by CLPT [10, 25]. In this work, CLPT was adopted to model the nonlinear dynamic behaviors of thin laminated composite plate specimens.

2.2 Lamina and laminate constitutive relations

In this section, the lamina and laminate constitutive relations are presented following the description of Gibson in [11]. For the experiment described in Chapter 3, a plain weave prepreg[1], which has orthotropic material properties, was used to fabricate the plate specimens. In a specially orthotropic lamina (Figure 2.2a), the directions of fibers (1-2 axes) are coincident with the directions of loading (x-y axes). On the other hand, in a generally orthotropic lamina (Figure 2.2b), the directions of fibers are not parallel to the directions of loading [27].

[1]Following the definition in [26], a prepreg is an abbreviation of pre-impregnated fibers. Prepregs are manufactured maintaining specified resin and fiber contents, and fiber orientations. Prepreg sheets can be produced by impregnating woven/braided/knitted fabric, cloth, and unidirectional fibers with resin.

2.2.1 Lamina constitutive relation of a specially orthotropic lamina

The lamina constitutive relation of a specially orthotropic lamina is given by

$$\begin{Bmatrix} \varepsilon_1 \\ \varepsilon_2 \\ \gamma_{12} \end{Bmatrix} = \begin{bmatrix} S_{11} & S_{12} & 0 \\ S_{21} & S_{22} & 0 \\ 0 & 0 & S_{66} \end{bmatrix} \begin{Bmatrix} \sigma_1 \\ \sigma_2 \\ \tau_{12} \end{Bmatrix} = \begin{bmatrix} \frac{1}{E_{11}} & -\frac{\nu_{12}}{E_{11}} & 0 \\ -\frac{\nu_{21}}{E_{22}} & \frac{1}{E_{22}} & 0 \\ 0 & 0 & \frac{1}{G_{12}} \end{bmatrix} \begin{Bmatrix} \sigma_1 \\ \sigma_2 \\ \tau_{12} \end{Bmatrix}, \tag{2.1}$$

or

$$\begin{Bmatrix} \sigma_1 \\ \sigma_2 \\ \tau_{12} \end{Bmatrix} = \begin{bmatrix} Q_{11} & Q_{12} & 0 \\ Q_{21} & Q_{22} & 0 \\ 0 & 0 & 2Q_{66} \end{bmatrix} \begin{Bmatrix} \varepsilon_1 \\ \varepsilon_2 \\ \frac{\gamma_{12}}{2} \end{Bmatrix}, \tag{2.2}$$

in which

$$\begin{aligned} Q_{11} =& \frac{S_{22}}{S_{11}S_{22} - S_{12}^2} = \frac{E_{11}}{1 - \nu_{12}\nu_{21}}, \\ Q_{12} =& -\frac{S_{12}}{S_{11}S_{22} - S_{12}^2} = \frac{\nu_{12}E_{22}}{1 - \nu_{12}\nu_{21}} = Q_{21}, \\ Q_{22} =& \frac{S_{11}}{S_{11}S_{22} - S_{12}^2} = \frac{E_{22}}{1 - \nu_{12}\nu_{21}}, \\ Q_{66} =& \frac{1}{S_{66}} = G_{12}. \end{aligned} \tag{2.3}$$

2.2.2 Lamina constitutive relation of a generally orthotropic lamina

The lamina constitutive relation of a generally orthotropic lamina is given by

$$\begin{Bmatrix} \varepsilon_{xx} \\ \varepsilon_{yy} \\ \gamma_{xy} \end{Bmatrix} = \begin{bmatrix} \bar{S}_{11} & \bar{S}_{12} & \bar{S}_{16} \\ \bar{S}_{12} & \bar{S}_{22} & \bar{S}_{26} \\ \bar{S}_{16} & \bar{S}_{26} & \bar{S}_{66} \end{bmatrix} \begin{Bmatrix} \sigma_{xx} \\ \sigma_{yy} \\ \tau_{xy} \end{Bmatrix}, \tag{2.4}$$

in which

$$\begin{aligned}
\bar{S}_{11} =& S_{11}c^4 + (2S_{12} + S_{66})s^2c^2 + S_{22}s^4, \\
\bar{S}_{12} =& S_{12}(s^4 + c^4) + (S_{11} + S_{22} - S_{66})s^2c^2, \\
\bar{S}_{22} =& S_{11}s^4 + (2S_{12} + S_{66})s^2c^2 + S_{22}c^4, \\
\bar{S}_{16} =& (2S_{11} - 2S_{12} - S_{66})sc^3 - (2S_{22} - 2S_{12} - S_{66})s^3c, \\
\bar{S}_{26} =& (2S_{11} - 2S_{12} - S_{66})s^3c - (2S_{22} - 2S_{12} - S_{66})sc^3, \\
\bar{S}_{66} =& 2(2S_{11} + 2S_{22} - 4S_{12} - S_{66})s^2c^2 + S_{66}(s^4 + c^4),
\end{aligned} \tag{2.5}$$

in which $s = \sin\theta$, $c = \cos\theta$, and θ is an angle between the 1-2 axes and the x-y axes as shown in Figure 2.2b. The relation in Equation (2.4) can be expressed as

$$\begin{Bmatrix} \sigma_{xx} \\ \sigma_{yy} \\ \tau_{xy} \end{Bmatrix} = \begin{bmatrix} \bar{Q}_{11} & \bar{Q}_{12} & \bar{Q}_{16} \\ \bar{Q}_{12} & \bar{Q}_{22} & \bar{Q}_{26} \\ \bar{Q}_{16} & \bar{Q}_{26} & \bar{Q}_{66} \end{bmatrix} \begin{Bmatrix} \varepsilon_{xx} \\ \varepsilon_{yy} \\ \gamma_{xy} \end{Bmatrix}, \tag{2.6}$$

in which

$$\begin{aligned}
\bar{Q}_{11} =& Q_{11}c^4 + 2(Q_{12} + 2Q_{66})s^2c^2 + Q_{22}s^4, \\
\bar{Q}_{12} =& Q_{12}(s^4 + c^4) + (Q_{11} + Q_{22} - 4Q_{66})s^2c^2, \\
\bar{Q}_{22} =& Q_{11}s^4 + 2(Q_{12} + 2Q_{66})s^2c^2 + Q_{22}c^4, \\
\bar{Q}_{16} =& (Q_{11} - Q_{12} - 2Q_{66})sc^3 - (Q_{22} - Q_{12} - 2Q_{66})s^3c, \\
\bar{Q}_{26} =& (Q_{11} - Q_{12} - 2Q_{66})s^3c - (Q_{22} - Q_{12} - 2Q_{66})sc^3, \\
\bar{Q}_{66} =& (Q_{11} + Q_{22} - 2Q_{12} - 2Q_{66})s^2c^2 + Q_{66}(s^4 + c^4).
\end{aligned} \tag{2.7}$$

2.3 Kirchhoff hypothesis and von Kármán strains

In this section, the Kirchhoff hypothesis and von Kármán strains are introduced following the description of Reddy in [25, 28]. The Kirchhoff hypothesis requires that the strains of plates vary linearly through the plate thickness and that the stresses in the direction normal to the plate middle surface (i.e., σ_{xz}, σ_{yz}, and σ_{zz}) are negligible. Thus, the hypothesis requires the displacements (u, v, w) to be such that

$$\begin{aligned} u(x,y,z,t) &= u_0(x,y,z) - z\frac{\partial w_0}{\partial x}, \\ v(x,y,z,t) &= v_0(x,y,z) - z\frac{\partial w_0}{\partial y}, \\ w(x,y,z,t) &= w_0(x,y,t), \end{aligned} \tag{2.8}$$

in which (u_0, v_0, w_0) are the displacements along the coordinate lines of a material point on the x-y plane (i.e., the midplane displacements).

The nonlinear strains based on the Green-Lagrange strain tensor are

$$\begin{aligned} E_{xx} &= \frac{\partial u}{\partial x} + \frac{1}{2}[(\frac{\partial u}{\partial x})^2 + (\frac{\partial v}{\partial x})^2 + (\frac{\partial w}{\partial x})^2], \\ E_{yy} &= \frac{\partial v}{\partial y} + \frac{1}{2}[(\frac{\partial u}{\partial y})^2 + (\frac{\partial v}{\partial y})^2 + (\frac{\partial w}{\partial y})^2], \\ E_{zz} &= \frac{\partial w}{\partial z} + \frac{1}{2}[(\frac{\partial u}{\partial z})^2 + (\frac{\partial v}{\partial z})^2 + (\frac{\partial w}{\partial z})^2], \\ E_{xy} &= \frac{1}{2}(\frac{\partial u}{\partial y} + \frac{\partial v}{\partial x} + \frac{\partial u}{\partial x}\frac{\partial u}{\partial y} + \frac{\partial v}{\partial x}\frac{\partial v}{\partial y} + \frac{\partial w}{\partial x}\frac{\partial w}{\partial y}), \\ E_{xz} &= \frac{1}{2}(\frac{\partial u}{\partial z} + \frac{\partial w}{\partial x} + \frac{\partial u}{\partial x}\frac{\partial u}{\partial z} + \frac{\partial v}{\partial x}\frac{\partial v}{\partial z} + \frac{\partial w}{\partial x}\frac{\partial w}{\partial z}), \\ E_{yz} &= \frac{1}{2}(\frac{\partial v}{\partial z} + \frac{\partial w}{\partial y} + \frac{\partial u}{\partial y}\frac{\partial u}{\partial z} + \frac{\partial v}{\partial y}\frac{\partial v}{\partial z} + \frac{\partial w}{\partial y}\frac{\partial w}{\partial z}), \end{aligned} \tag{2.9}$$

or in the index form [29],

$$E_{ij} = \frac{1}{2}(\frac{\partial u_i}{\partial x_j} + \frac{\partial u_j}{\partial x_i} + \frac{\partial u_k}{\partial x_i}\frac{\partial u_k}{\partial x_j}). \tag{2.10}$$

Based on the aforementioned assumption of CLPT, in case the terms $\frac{\partial u}{\partial x}$, $\frac{\partial u}{\partial y}$, $\frac{\partial v}{\partial x}$, $\frac{\partial v}{\partial y}$, and $\frac{\partial w}{\partial z}$ are of the order of small strains $\varepsilon \ll 1$ (i.e., $O(\varepsilon)$), the terms of $O(\varepsilon^2)$ in Equation (2.9) are negligible. However, for moderate rotations (10^o to 15^o) of transverse normals ($\frac{\partial w_0}{\partial x}$ and $\frac{\partial w_0}{\partial y}$), the terms $(\frac{\partial w}{\partial x})^2$, $(\frac{\partial w}{\partial y})^2$, and $\frac{\partial w}{\partial x}\frac{\partial w}{\partial y}$ of $O(\varepsilon^2)$ are not negligible. Thus, the strain-displacement relations for small strains and moderate rotations can be given by

$$\begin{aligned}
\varepsilon_{xx} &= \frac{\partial u}{\partial x} + \frac{1}{2}(\frac{\partial w}{\partial x})^2, \\
\varepsilon_{yy} &= \frac{\partial v}{\partial y} + \frac{1}{2}(\frac{\partial w}{\partial y})^2, \\
\varepsilon_{zz} &= \frac{\partial w}{\partial z}, \\
\varepsilon_{xy} &= \frac{1}{2}(\frac{\partial u}{\partial y} + \frac{\partial v}{\partial x} + \frac{\partial w}{\partial x}\frac{\partial w}{\partial y}), \\
\varepsilon_{xz} &= \frac{1}{2}(\frac{\partial u}{\partial z} + \frac{\partial w}{\partial x}), \\
\varepsilon_{yz} &= \frac{1}{2}(\frac{\partial v}{\partial z} + \frac{\partial w}{\partial y}).
\end{aligned} \tag{2.11}$$

Substituting Equation (2.8) into Equation (2.11) yields

$$\begin{aligned}
\varepsilon_{xx} &= \frac{\partial u_0}{\partial x} + \frac{1}{2}(\frac{\partial w_0}{\partial x})^2 - z\frac{\partial^2 w_0}{\partial x^2}, \\
\varepsilon_{yy} &= \frac{\partial v_0}{\partial y} + \frac{1}{2}(\frac{\partial w_0}{\partial y})^2 - z\frac{\partial^2 w_0}{\partial y^2}, \\
\varepsilon_{zz} &= 0, \\
\varepsilon_{xy} &= \frac{1}{2}(\frac{\partial u_0}{\partial y} + \frac{\partial v_0}{\partial x} + \frac{\partial w_0}{\partial x}\frac{\partial w_0}{\partial y}) - z\frac{\partial^2 w_0}{\partial x \partial y}, \\
\varepsilon_{xz} &= \frac{1}{2}(-\frac{\partial w_0}{\partial x} + \frac{\partial w_0}{\partial x}) = 0, \\
\varepsilon_{yz} &= \frac{1}{2}(-\frac{\partial w_0}{\partial y} + \frac{\partial w_0}{\partial y}) = 0.
\end{aligned} \tag{2.12}$$

The strains in Equation (2.12) are called the von Kármán strains, which are accurate enough for moderately large vibrations of plates. The expressions in Equation (2.12) can be categorized as

$$\begin{Bmatrix} \varepsilon_{xx} \\ \varepsilon_{yy} \\ \gamma_{xy} \end{Bmatrix} = \begin{Bmatrix} {\varepsilon_{xx}}^{(0)} \\ {\varepsilon_{yy}}^{(0)} \\ {\gamma_{xy}}^{(0)} \end{Bmatrix} + z \begin{Bmatrix} \kappa_{xx} \\ \kappa_{yy} \\ 2\kappa_{xy} \end{Bmatrix}, \tag{2.13}$$

in which the membrane strains $({\varepsilon_{xx}}^{(0)}, {\varepsilon_{yy}}^{(0)}, {\gamma_{xy}}^{(0)})$ are given by

$$\begin{Bmatrix} {\varepsilon_{xx}}^{(0)} \\ {\varepsilon_{yy}}^{(0)} \\ {\gamma_{xy}}^{(0)} \end{Bmatrix} = \begin{Bmatrix} \frac{\partial u_0}{\partial x} + \frac{1}{2}(\frac{\partial w_0}{\partial x})^2 \\ \frac{\partial v_0}{\partial y} + \frac{1}{2}(\frac{\partial w_0}{\partial y})^2 \\ \frac{\partial u_0}{\partial y} + \frac{\partial v_0}{\partial x} + \frac{\partial w_0}{\partial x}\frac{\partial w_0}{\partial y} \end{Bmatrix}, \tag{2.14}$$

and the flexural (or bending) strains $(\kappa_{xx}, \kappa_{yy}, \kappa_{xy})$, known as the curvatures, are given by

$$\begin{Bmatrix} \kappa_{xx} \\ \kappa_{yy} \\ \kappa_{xy} \end{Bmatrix} = \begin{Bmatrix} -\frac{\partial^2 w_0}{\partial x^2} \\ -\frac{\partial^2 w_0}{\partial y^2} \\ -\frac{\partial^2 w_0}{\partial x \partial y} \end{Bmatrix}. \tag{2.15}$$

2.3.1 Laminate constitutive relation

The in-plane force (or membrane stress) resultants N_{ij} and the flexural (or bending) moment resultants M_{ij} are given by

$$\begin{Bmatrix} N_{xx} \\ N_{yy} \\ N_{xy} \end{Bmatrix} = \int_{-h/2}^{h/2} \begin{Bmatrix} \sigma_{xx} \\ \sigma_{yy} \\ \sigma_{xy} \end{Bmatrix} dz, \tag{2.16}$$

$$\begin{Bmatrix} M_{xx} \\ M_{yy} \\ M_{xy} \end{Bmatrix} = \int_{-h/2}^{h/2} \begin{Bmatrix} \sigma_{xx} \\ \sigma_{yy} \\ \sigma_{xy} \end{Bmatrix} z \; dz. \tag{2.17}$$

Applying the aforementioned lamina constitutive relations to Equations (2.16) and (2.17), the laminate constitutive relation can be defined as

$$\begin{Bmatrix} N_{xx} \\ N_{yy} \\ N_{xy} \\ M_{xx} \\ M_{yy} \\ M_{xy} \end{Bmatrix} = \begin{bmatrix} A_{11} & A_{12} & A_{16} & B_{11} & B_{12} & B_{16} \\ A_{12} & A_{22} & A_{26} & B_{12} & B_{22} & B_{26} \\ A_{16} & A_{26} & A_{66} & B_{16} & B_{26} & B_{66} \\ B_{11} & B_{12} & B_{16} & D_{11} & D_{12} & D_{16} \\ B_{12} & B_{22} & B_{26} & D_{12} & D_{22} & D_{26} \\ B_{16} & B_{26} & B_{66} & D_{16} & D_{26} & D_{66} \end{bmatrix} \begin{Bmatrix} \varepsilon^0_{xx} \\ \varepsilon^0_{yy} \\ \gamma^0_{xy} \\ \kappa_{xx} \\ \kappa_{yy} \\ \kappa_{xy} \end{Bmatrix}, \tag{2.18}$$

in which the laminate extensional stiffnesses are given by

$$A_{ij} = \int_{-t/2}^{t/2} \bar{Q}_{ij} dz = \sum_{k=1}^{N} (\bar{Q}_{ij})_k (z_k - z_{k-1}), \tag{2.19}$$

the laminate bending-extensional coupling stiffnesses are given by

$$B_{ij} = \int_{-t/2}^{t/2} \bar{Q}_{ij} z dz = \frac{1}{2} \sum_{k=1}^{N} (\bar{Q}_{ij})_k (z_k^2 - z_{k-1}^2), \tag{2.20}$$

and the laminate-bending stiffnesses are given by

$$D_{ij} = \int_{-t/2}^{t/2} \bar{Q}_{ij} z^2 dz = \frac{1}{3} \sum_{k=1}^{N} (\bar{Q}_{ij})_k (z_k^3 - z_{k-1}^3). \tag{2.21}$$

Inverting Equation (2.18) yields

$$\begin{Bmatrix} \varepsilon_{xx}^0 \\ \varepsilon_{yy}^0 \\ \gamma_{xy}^0 \\ \kappa_{xx} \\ \kappa_{yy} \\ \kappa_{xy} \end{Bmatrix} = \begin{bmatrix} a_{11} & a_{12} & a_{16} & b_{11} & b_{12} & b_{16} \\ a_{12} & a_{22} & a_{26} & b_{12} & b_{22} & b_{26} \\ a_{16} & a_{26} & a_{66} & b_{16} & b_{26} & b_{66} \\ b_{11} & b_{12} & b_{16} & d_{11} & d_{12} & d_{16} \\ b_{12} & b_{22} & b_{26} & d_{12} & d_{22} & d_{26} \\ b_{16} & b_{26} & b_{66} & d_{16} & d_{26} & d_{66} \end{bmatrix} \begin{Bmatrix} N_{xx} \\ N_{yy} \\ N_{xy} \\ M_{xx} \\ M_{yy} \\ M_{xy} \end{Bmatrix}. \tag{2.22}$$

Applying the von Kármán strains in Equation (2.13), (2.14), and (2.15) to the laminate constitutive relation in Equation (2.18) yields

$$\begin{Bmatrix} N_{xx} \\ N_{yy} \\ N_{xy} \end{Bmatrix} = \begin{bmatrix} A_{11} & A_{12} & A_{16} \\ A_{12} & A_{22} & A_{26} \\ A_{16} & A_{26} & A_{66} \end{bmatrix} \begin{Bmatrix} \frac{\partial u_0}{\partial x} + \frac{1}{2}(\frac{\partial w_0}{\partial x})^2 \\ \frac{\partial v_0}{\partial y} + \frac{1}{2}(\frac{\partial w_0}{\partial y})^2 \\ \frac{\partial u_0}{\partial y} + \frac{\partial v_0}{\partial x} + \frac{\partial w_0}{\partial x}\frac{\partial w_0}{\partial y} \end{Bmatrix} + \begin{bmatrix} B_{11} & B_{12} & B_{16} \\ B_{12} & B_{22} & B_{26} \\ B_{16} & B_{26} & B_{66} \end{bmatrix} \begin{Bmatrix} -\frac{\partial^2 w_0}{\partial x^2} \\ -\frac{\partial^2 w_0}{\partial y^2} \\ -2\frac{\partial^2 w_0}{\partial x \partial y} \end{Bmatrix},$$

$$\begin{Bmatrix} M_{xx} \\ M_{yy} \\ M_{xy} \end{Bmatrix} = \begin{bmatrix} B_{11} & B_{12} & B_{16} \\ B_{12} & A_{22} & B_{26} \\ B_{16} & B_{26} & B_{66} \end{bmatrix} \begin{Bmatrix} \frac{\partial u_0}{\partial x} + \frac{1}{2}(\frac{\partial w_0}{\partial x})^2 \\ \frac{\partial v_0}{\partial y} + \frac{1}{2}(\frac{\partial w_0}{\partial y})^2 \\ \frac{\partial u_0}{\partial y} + \frac{\partial v_0}{\partial x} + \frac{\partial w_0}{\partial x}\frac{\partial w_0}{\partial y} \end{Bmatrix} + \begin{bmatrix} D_{11} & D_{12} & D_{16} \\ D_{12} & D_{22} & D_{26} \\ D_{16} & D_{26} & D_{66} \end{bmatrix} \begin{Bmatrix} -\frac{\partial^2 w_0}{\partial x^2} \\ -\frac{\partial^2 w_0}{\partial y^2} \\ -2\frac{\partial^2 w_0}{\partial x \partial y} \end{Bmatrix}. \tag{2.23}$$

2.4 Nonlinear equations of motion in CLPT

In this section, the derivation of the nonlinear equations of motion is presented based on Reddy's work in [25, 28]. Based on Hamilton's principle, the principle of virtual displacements can be stated as: *if a system, which is in equilibrium under the action of a set of forces, is subjected to a virtual displacement, then the total work done by the forces will be zero* [30], i.e.,

$$\delta U + \delta V = \delta W = 0, \tag{2.24}$$

in which the virtual strain energy δU is given by

$$\begin{aligned}
\delta U &= \int_{\Omega_0} \int_{-\frac{h}{2}}^{\frac{h}{2}} (\sigma_{xx}\delta\varepsilon_{xx} + \sigma_{yy}\delta\varepsilon_{yy} + 2\sigma_{xy}\delta\varepsilon_{xy}) dz dx dy \\
&= \int_{\Omega_0} \Big\{ \int_{-\frac{h}{2}}^{\frac{h}{2}} \Big[\sigma_{xx}\big(\delta\epsilon_{xx}^{(0)} + z\delta\kappa_{xx}\big) + \sigma_{yy}\big(\delta\epsilon_{yy}^{(0)} + z\delta\kappa_{yy}\big) \\
&\quad + \sigma_{xy}\big(\delta\gamma_{xy}^{(0)} + 2z\delta\kappa_{xy}\big) \Big] dz \Big\} dx dy,
\end{aligned} \tag{2.25}$$

and the virtual work δV due to the applied forces is given by

$$\begin{aligned}
\delta V &= -\int_{\Omega_0} \Big[q_b(x,y)\delta w\Big(x,y,\frac{h}{2}\Big) + q_t(x,y)\delta w\Big(x,y,-\frac{h}{2}\Big) \Big] dx dy \\
&\quad - \int_{\Gamma_\sigma} \int_{-\frac{h}{2}}^{\frac{h}{2}} [\hat{\sigma}_{nn}\delta u_n + \hat{\sigma}_{ns}\delta u_s + \hat{\sigma}_{nz}\delta w] dz ds \\
&= -\int_{\Omega_0} \big\{ \big[q_b(x,y) + q_t(x,y) \big] \delta w_0(x,y) \big\} dx dy \\
&\quad - \int_{\Gamma_\sigma} \int_{-\frac{h}{2}}^{\frac{h}{2}} \Big[\hat{\sigma}_{nn}\Big(\delta u_{0n} - z\frac{\partial \delta w_0}{\partial \delta n}\Big) + \hat{\sigma}_{ns}\Big(\delta u_{0s} - z\frac{\partial \delta w_0}{\partial \delta s}\Big) + \hat{\sigma}_{nz}\delta w_0 \Big] dz ds,
\end{aligned} \tag{2.26}$$

in which

- Γ is the closed boundary of the total domain Ω of the plate,
- Ω_0 denotes the undeformed midplane of Ω,

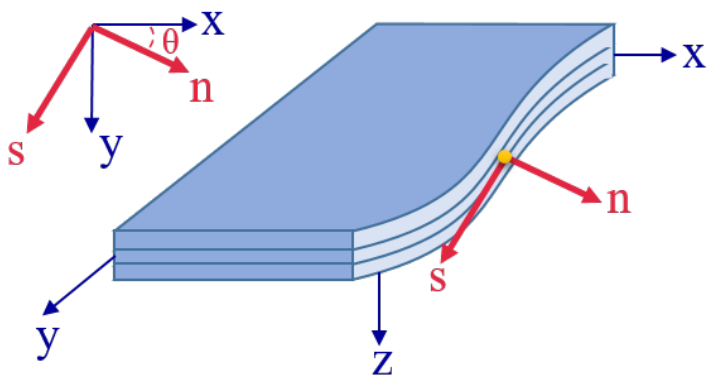

Figure 2.3: Coordinate system on the curved boundary.

- n and s in Figure 2.3 denote the normal and tangential directions from a point on Γ, respectively,
- Γ_σ is the portion of Γ on which applied stress components ($\hat{\sigma}_{nn}$, $\hat{\sigma}_{ns}$, $\hat{\sigma}_{nz}$) are specified while Γ_u is the portion of Γ whose displacements are prescribed,
- q_b and q_t are the distributed forces at the bottom and at the top of the laminate, respectively, and
- δu_{0n} and δu_{0s} are the virtual displacements along the normal and tangential directions on Γ, respectively.

The dynamic version of the principle of virtual work can be defined as

$$0 = \int_0^T (\delta U + \delta V - \delta K) dt, \tag{2.27}$$

in which the virtual kinetic energy δK is given by

$$\begin{aligned} \delta K = \int_{\Omega_0} \int_{-\frac{h}{2}}^{\frac{h}{2}} \rho_0 \Big[\Big(\dot{u}_0 - z\frac{\partial \dot{w}_0}{\partial x} \Big) \Big(\delta \dot{u}_0 - z\frac{\partial \delta \dot{w}_0}{\partial x} \Big) \\ + \Big(\dot{v}_0 - z\frac{\partial \dot{w}_0}{\partial y} \Big) \Big(\delta \dot{v}_0 - z\frac{\partial \delta \dot{w}_0}{\partial y} \Big) + \dot{w}_0 \delta \dot{w}_0 \Big] dz dx dy, \end{aligned} \tag{2.28}$$

in which ρ_0 is the density of the plate material. Substituting δU, δV, and δK into Equation (2.27),

$$\begin{aligned}
0 = \int_0^T \{ \int_{\Omega_0} [& N_{xx}\delta{\epsilon_{xx}}^{(0)} + M_{xx}\delta\kappa_{xx} + N_{yy}\delta{\epsilon_{yy}}^{(0)} + M_{yy}\delta\kappa_{yy} + N_{xy}\delta{\gamma_{xy}}^{(0)} \\
& + M_{xy}\delta 2\kappa_{xy} - q\delta w_0 - I_0(\dot{u}_0\delta\dot{u}_0 + \dot{v}_0\delta\dot{v}_0 + \dot{w}_0\delta\dot{w}_0) \\
& + I_1(\frac{\partial\delta\dot{w}_0}{\partial x}\dot{u}_0 + \frac{\partial\dot{w}_0}{\partial x}\delta\dot{u}_0 + \frac{\partial\delta\dot{w}_0}{\partial y}\dot{v}_0 + \frac{\partial\dot{w}_0}{\partial y}\delta\dot{v}_0) \\
& - I_2(\frac{\partial\dot{w}_0}{\partial x}\frac{\partial\delta\dot{w}_0}{\partial x} + \frac{\partial\dot{w}_0}{\partial y}\frac{\partial\delta\dot{w}_0}{\partial y})]dxdy \\
& - \int_{\Gamma_\sigma} (\hat{N_{nn}}\delta u_{0n} + \hat{N_{ns}}\delta u_{0s} - \hat{M_{nn}}\frac{\partial\delta w_0}{\partial n} - \hat{M_{ns}}\frac{\partial\delta w_0}{\partial s} + \hat{Q_n}\delta w_0)ds\}dt,
\end{aligned} \tag{2.29}$$

in which $q = q_b + q_t$ is the total transverse load, the in-plane force resultants on Γ_σ are given by

$$\begin{Bmatrix} \hat{N}_{nn} \\ \hat{N}_{ns} \end{Bmatrix} = \int_{-h/2}^{h/2} \begin{Bmatrix} \hat{\sigma}_{nn} \\ \hat{\sigma}_{ns} \end{Bmatrix} dz, \tag{2.30}$$

the moment resultants on Γ_σ are given by

$$\begin{Bmatrix} \hat{M}_{nn} \\ \hat{M}_{ns} \end{Bmatrix} = \int_{-h/2}^{h/2} \begin{Bmatrix} \hat{\sigma}_{nn} \\ \hat{\sigma}_{ns} \end{Bmatrix} z \ dz, \tag{2.31}$$

the transverse force resultant Q_n is given by

$$\hat{Q}_n = \int_{-h/2}^{h/2} \hat{\sigma}_{nz} dz, \tag{2.32}$$

and the mass moments of inertia (I_0, I_1, I_2) are given by

$$\begin{Bmatrix} I_0 \\ I_1 \\ I_2 \end{Bmatrix} = \int_{-h/2}^{h/2} \begin{Bmatrix} 1 \\ z \\ z^2 \end{Bmatrix} \rho_0 dz. \tag{2.33}$$

Applying the von Kármán strains in Equations (2.13), (2.14), and (2.15) to Equation (2.29) and then collecting terms with respect to the virtual displacements (δu_0, δv_0, δw_0),

$$\begin{aligned}
0 = \int_0^T \Big\{ \int_{\Omega_0} \Big[& \Big(-N_{xx,x} + N_{xy,y} - I_0\ddot{u}_0 + I_1\frac{\partial \ddot{w}_0}{\partial x} \Big)\delta u_0 \\
& - \Big(N_{xy,x} + N_{yy,y} - I_0\ddot{v}_0 + I_1\frac{\partial \ddot{w}_0}{\partial y} \Big)\delta v_0 \\
& - \Big(M_{xx,xx} + 2M_{xy,xy} + M_{yy,yy} + \frac{\partial}{\partial x}(N_{xx}\frac{\partial w_0}{\partial x} + N_{xy}\frac{\partial w_0}{\partial y}) \\
& + \frac{\partial}{\partial y}(N_{xy}\frac{\partial w_0}{\partial x} + N_{yy}\frac{\partial w_0}{\partial y}) + q - I_0\ddot{w}_0 - I_1\frac{\partial \ddot{u}_0}{\partial x} + I_2\frac{\partial^2 \ddot{w}_0}{\partial x^2} + I_2\frac{\partial^2 \ddot{w}_0}{\partial y^2} \Big)\delta w_0 \Big] dxdy \\
+ \int_{\Gamma_\sigma} \Big[& (N_{xx}n_x + N_{xy}n_y)\delta u_0 + (N_{xy}n_x + N_{yy}n_y)\delta v_0 \\
& + \Big(M_{xx,x}n_x + M_{xy,y}n_x + M_{yy,y}n_y + M_{xy,x}n_y \\
& + (N_{xx}\frac{\partial w_0}{\partial x} + N_{xy}\frac{\partial w_0}{\partial y})n_x + (N_{xy}\frac{\partial w_0}{\partial x} + N_{yy}\frac{\partial w_0}{\partial y})n_y \\
& - I_1\ddot{u}_0 n_x - I_1\ddot{v}_0 n_y + I_2\frac{\partial \ddot{w}_0}{\partial x}n_x + I_2\frac{\partial \ddot{w}_0}{\partial y}n_y \Big)\delta w_0 \\
& - (M_{xx}n_x + M_{xy}n_y)\frac{\partial \delta w_0}{\partial x} - (M_{xy}n_x + M_{yy}n_y)\frac{\partial \delta w_0}{\partial y} \Big] ds \\
- \int_{\Gamma_\sigma} & \Big(\hat{N}_{nn}\delta u_{0n} + \hat{N}_{ns}\delta u_{0s} - \hat{M}_{nn}\frac{\partial \delta w_0}{\partial n} - \hat{M}_{ns}\frac{\partial \delta w_0}{\partial s} + \hat{Q}_n\delta w_0 \Big) ds \Big\} dt.
\end{aligned} \tag{2.34}$$

2.4.1 Equations of motion

Setting the coefficients of δu_0, δv_0, and δw_0 over Ω_0 in Equation (2.34) to zero separately since they are independent, the nonlinear equations of motion are given by

$$\delta u_0 : \quad \frac{\partial N_{xx}}{\partial x} + \frac{\partial N_{xy}}{\partial y} = I_0 \frac{\partial^2 u_0}{\partial t^2} - I_1 \frac{\partial^2}{\partial t^2}(\frac{\partial w_0}{\partial x}), \tag{2.35}$$

$$\delta v_0 : \quad \frac{\partial N_{xy}}{\partial x} + \frac{\partial N_{yy}}{\partial y} = I_0 \frac{\partial^2 v_0}{\partial t^2} - I_1 \frac{\partial^2}{\partial t^2}(\frac{\partial w_0}{\partial y}), \tag{2.36}$$

$$\begin{aligned} \delta w_0 : \quad & \frac{\partial^2 M_{xx}}{\partial x^2} + 2\frac{\partial^2 M_{xy}}{\partial y \partial x} + \frac{\partial^2 M_{yy}}{\partial^2 y} + \frac{\partial}{\partial x}(N_{xx}\frac{\partial w_0}{\partial x} + N_{xy}\frac{\partial w_0}{\partial y}) \\ & + \frac{\partial}{\partial y}(N_{xy}\frac{\partial w_0}{\partial x} + N_{yy}\frac{\partial w_0}{\partial y}) + q = I_0 \frac{\partial^2 w_0}{\partial t^2} - I_2 \frac{\partial^2}{\partial t^2}(\frac{\partial^2 w_0}{\partial x^2} + \frac{\partial^2 w_0}{\partial y^2}) \\ & + I_1 \frac{\partial^2}{\partial t^2}(\frac{\partial u_0}{\partial x} + \frac{\partial v_0}{\partial y}). \end{aligned} \tag{2.37}$$

2.4.2 Boundary conditions

The boundary conditions are obtained by collecting the coefficients of the virtual displacements and their derivatives on the boundary Γ_σ in Equation (2.34).

As shown in Figure 2.3, since the angle between the unit outward normal vector $\hat{\mathbf{n}}$ and the x-axis is θ, its direction cosines are given by $n_x = \cos\theta$ and $n_y = \sin\theta$. The transformation between the coordinate systems (n, s, r) and (x, y, z) are given by Equation (2.38).

$$\begin{aligned} \hat{\mathbf{e}}_x &= cos\theta \hat{\mathbf{e}}_n - sin\theta \hat{\mathbf{e}}_s = n_x \hat{\mathbf{e}}_n - n_y \hat{\mathbf{e}}_s, \\ \hat{\mathbf{e}}_y &= sin\theta \hat{\mathbf{e}}_n + cos\theta \hat{\mathbf{e}}_s = n_y \hat{\mathbf{e}}_n + n_x \hat{\mathbf{e}}_s, \\ \hat{\mathbf{e}}_z &= \hat{\mathbf{e}}_r. \end{aligned} \tag{2.38}$$

Using the transformation, the displacements (u_0, v_0) and the derivatives $(w_{0,x}, w_{0,y})$ can be expressed in terms of (u_{0n}, v_{0s}) and $(w_{0,n}, w_{0,s})$, respectively as shown in Equations (2.39)

and Equations (2.40).

$$\begin{aligned} u_0 &= n_x u_{0n} - n_y u_{0s}, \\ v_0 &= n_y u_{0n} + n_x u_{0s}. \end{aligned} \tag{2.39}$$

$$\begin{aligned} \frac{\partial w_0}{\partial x} &= n_x \frac{\partial w_0}{\partial n} - n_y \frac{\partial w_0}{\partial s}, \\ \frac{\partial w_0}{\partial y} &= n_y \frac{\partial w_0}{\partial n} + n_x \frac{\partial w_0}{\partial s}. \end{aligned} \tag{2.40}$$

Using the stress transformation,

$$\begin{Bmatrix} \sigma_{nn} \\ \sigma_{ns} \end{Bmatrix} = \begin{bmatrix} {n_x}^2 & {n_y}^2 & 2n_x n_y \\ {n_x}^2 & {n_y}^2 & 2n_x n_y \end{bmatrix} \begin{Bmatrix} \sigma_{xx} \\ \sigma_{yy} \\ \sigma_{xy} \end{Bmatrix}. \tag{2.41}$$

Substituting Equation (2.41) into Equations (2.16) and (2.17) yields

$$\begin{Bmatrix} N_{nn} \\ N_{ns} \end{Bmatrix} = \begin{bmatrix} {n_x}^2 & {n_y}^2 & 2n_x n_y \\ {n_x}^2 & {n_y}^2 & 2n_x n_y \end{bmatrix} \begin{Bmatrix} N_{xx} \\ N_{yy} \\ N_{xy} \end{Bmatrix}, \tag{2.42}$$

$$\begin{Bmatrix} M_{nn} \\ M_{ns} \end{Bmatrix} = \begin{bmatrix} {n_x}^2 & {n_y}^2 & 2n_x n_y \\ {n_x}^2 & {n_y}^2 & 2n_x n_y \end{bmatrix} \begin{Bmatrix} M_{xx} \\ M_{yy} \\ M_{xy} \end{Bmatrix}. \tag{2.43}$$

Substituting Equations (2.42) and (2.43) to the boundary integrals in Equation (2.34),

$$
\begin{aligned}
0 = \int_0^T \int_{\Gamma_\sigma} \Big[& (N_{nn} - \hat{N}_{nn})\delta u_{0n} + (N_{ns} - \hat{N}_{ns})\delta u_{0s} \\
& + \Big(M_{xx,x} n_x + M_{xy,y} n_x + M_{yy,y} n_y + M_{xy,x} n_y \\
& + (N_{xx}\frac{\partial w_0}{\partial x} + N_{xy}\frac{\partial w_0}{\partial y}) n_x + (N_{xy}\frac{\partial w_0}{\partial x} + N_{yy}\frac{\partial w_0}{\partial y}) n_y \\
& - I_1 \ddot{u}_0 n_x - I_1 \ddot{v}_0 n_y + I_2 \frac{\partial \ddot{w}_0}{\partial x} n_x + I_2 \frac{\partial \ddot{w}_0}{\partial y} n_y - \hat{Q}_n \Big) \delta w_0 \\
& - (M_{nn} - \hat{M}_{nn}) \frac{\partial \delta w_0}{\partial n} - (M_{ns} - \hat{M}_{ns}) \frac{\partial \delta w_0}{\partial s} \Big] ds dt.
\end{aligned}
\tag{2.44}
$$

Thus, the natural boundary conditions[2] are given by

$$
\begin{aligned}
N_{nn} - \hat{N}_{nn} &= 0, \\
N_{ns} - \hat{N}_{ns} &= 0, \\
Q_n - \hat{Q}_{nn} &= 0, \\
M_{nn} - \hat{M}_{nn} &= 0, \\
M_{ns} - \hat{M}_{ns} &= 0,
\end{aligned}
\tag{2.45}
$$

on Γ_σ, in which

$$
\begin{aligned}
Q_n = & \Big(M_{xx,x} + M_{xy,y} - I_1 \ddot{u}_0 + I_2 \frac{\partial \ddot{w}_0}{\partial x} + N_{xx}\frac{\partial w_0}{\partial x} + N_{xy}\frac{\partial w_0}{\partial y} \Big) n_x \\
& + \Big(M_{yy,y} + M_{xy,x} - I_1 \ddot{v}_0 n_y + I_2 \frac{\partial \ddot{w}_0}{\partial y} + N_{xy}\frac{\partial w_0}{\partial x} + N_{yy}\frac{\partial w_0}{\partial y} \Big) n_y.
\end{aligned}
\tag{2.46}
$$

From Equation (2.44), the primary variables (i.e., generalized displacements) are

$$
u_n,\ u_s,\ w_0,\ \frac{\partial w_0}{\partial n},\ \frac{\partial w_0}{\partial s},
\tag{2.47}
$$

[2]Essential boundary conditions require u and its derivatives (primary variables) to vanish at the boundary while natural boundary conditions require the specification of the coefficients (secondary variables) of u and its derivatives [31].

and secondary variables (i.e., generalized forces) are

$$N_{nn},\ N_{ns},\ Q_n,\ M_{nn},\ M_{ns}. \tag{2.48}$$

The generalized displacements are specified on Γ_u, which constitutes the essential (or geometric) boundary conditions.

The history and thorough derivation of the Kirchhoff shear resultant is explained in detail by Tuttle in [32]. For the completeness, the Kirchhoff shear resultant is given here by

$$V_n = Q_n + \frac{\partial M_{ns}}{\partial s}, \tag{2.49}$$

which should be balanced by the applied force $\hat{Q}_n$. This boundary condition is known as the Kirchhoff free-edge boundary condition given by

$$V_n = \hat{Q}_n. \tag{2.50}$$

Applying the Kirchhoff shear resultant into Equations (2.47) and (2.48), the boundary conditions of CLPT are given by

$$\text{Essential (or geometric) boundary condition:}\quad u_n,\ u_s,\ w_0,\ \frac{\partial w_0}{\partial n}, \tag{2.51}$$

$$\text{Natural (or static) boundary condition:}\quad N_{nn},\ N_{ns},\ V_n,\ M_{nn}. \tag{2.52}$$

2.5 Nonlinear Finite Element Model of CLPT

In this section, the nonlinear finite element model (FEM) based on the nonlinear equations of motion (Equations (2.35), (2.36), and (2.37)) are derived based on Reddy's work in [25, 28, 31, 33, 34].

2.5.1 Integration-by-parts, gradient and divergence theorems

Using integration-by-parts,

$$\int_a^b w\frac{dv}{dx}dx = -\int_a^b v\frac{dw}{dx}dx + \int_a^b \frac{d}{dx}(wv)dx. \tag{2.53}$$

in which u, v, and w are sufficiently differentiable functions.

Let $F(x,y)$ and $G(x,y)$ be scalar functions in the 2-D domain Ω. Using the gradient theorem,

$$\int_\Omega \nabla F dxdy = \oint_\Gamma \hat{\mathbf{n}} F ds, \tag{2.54}$$

$$\int_\Omega \Big(\hat{\mathbf{e}}_x\frac{\partial F}{\partial x} + \hat{\mathbf{e}}_y\frac{\partial F}{\partial y}\Big)dxdy = \oint_\Gamma (n_x\hat{\mathbf{e}}_x + n_y\hat{\mathbf{e}}_y)Fds. \tag{2.55}$$

in which the gradient operator ∇ is $\nabla = \hat{\mathbf{e}}_x\frac{\partial}{\partial x} + \hat{\mathbf{e}}_y\frac{\partial}{\partial y}$, $\hat{\mathbf{e}}_x$ and $\hat{\mathbf{e}}_y$ denote the unit basis vectors along the x and y coordinates, respectively. In addition, $\hat{\mathbf{n}}$ denotes the unit vector normal to the surface Γ of the domain Ω, and then the direction cosines n_x and n_y of the unit vector $\hat{\mathbf{n}}$ are given by

$$n_x = cos(x,\hat{\mathbf{n}}) = \hat{\mathbf{e}}_x\cdot\hat{\mathbf{n}},\ \ n_y = cos(y,\hat{\mathbf{n}}) = \hat{\mathbf{e}}_y\cdot\hat{\mathbf{n}}. \tag{2.56}$$

in which $cos(x,\hat{\mathbf{n}})$ denotes the cosine of the angle between the positive x direction and the unit vector $\hat{\mathbf{n}}$ while $cos(y,\hat{\mathbf{n}})$ denotes the cosine of the angle between the positive y direction and the unit vector $\hat{\mathbf{n}}$.

The fact that the two vectors shown in Equation (2.55) are equal if and only if their components are equal leads to

$$\int_\Omega \frac{\partial F}{\partial x}dxdy = \oint_\Gamma n_x F ds,\ \ \int_\Omega \frac{\partial F}{\partial y}dxdy = \oint_\Gamma n_y F ds. \tag{2.57}$$

Using the divergence theorem,

$$\int_{\Omega} \nabla \cdot \mathbf{G} dxdy = \oint_{\Gamma} \hat{\mathbf{n}} \cdot \mathbf{G} ds, \tag{2.58}$$

$$\int_{\Omega} \Big(\frac{\partial G}{\partial x} + \frac{\partial G}{\partial y} \Big) dxdy = \oint_{\Gamma} (n_x G_x + n_y G_y) ds. \tag{2.59}$$

Using integration-by-parts, gradient and divergence theorems in Equations (2.53), (2.57), and (2.59),

$$\int_{\Omega} (\nabla G) w dxdy = - \int_{\Omega} (\nabla w) G dxdy + \oint_{\Gamma} \hat{\mathbf{n}} w G ds. \tag{2.60}$$

Using Equation (2.57), the component forms of Equation (2.60) are give by

$$\int_{\Omega} w \frac{\partial G}{\partial x} dxdy = - \int_{\Omega} \frac{\partial w}{\partial x} G dxdy + \oint_{\Gamma} n_x w G ds, \tag{2.61}$$

$$\int_{\Omega} w \frac{\partial G}{\partial y} dxdy = - \int_{\Omega} \frac{\partial w}{\partial y} G dxdy + \oint_{\Gamma} n_y w G ds. \tag{2.62}$$

2.5.2 Weak form of nonlinear equations of motion

To derive the nonlinear FEM, taking the weak forms of the nonlinear equations of motion in Equation (2.35), (2.36), and (2.37),

$$0 = \int_{\Omega^e} \delta u_0 \Big[- \frac{\partial N_{xx}}{\partial x} - \frac{\partial N_{xy}}{\partial y} + I_0 \frac{\partial^2 u_0}{\partial t^2} - I_1 \frac{\partial^2}{\partial t^2} \big(\frac{\partial w_0}{\partial x} \big) \Big] dxdy, \tag{2.63}$$

$$0 = \int_{\Omega^e} \delta v_0 \Big[- \frac{\partial N_{xy}}{\partial x} - \frac{\partial N_{yy}}{\partial y} + I_0 \frac{\partial^2 v_0}{\partial t^2} - I_1 \frac{\partial^2}{\partial t^2} \big(\frac{\partial w_0}{\partial y} \big) \Big] dxdy, \tag{2.64}$$

$$
\begin{aligned}
0 = \int_{\Omega^e} \delta w_0 \Big[& -\frac{\partial^2 M_{xx}}{\partial x^2} - 2\frac{\partial^2 M_{xy}}{\partial y \partial x} - \frac{\partial^2 M_{yy}}{\partial^2 y} - \frac{\partial}{\partial x}(N_{xx}\frac{\partial w_0}{\partial x} + N_{xy}\frac{\partial w_0}{\partial y}) \\
& - \frac{\partial}{\partial y}(N_{xy}\frac{\partial w_0}{\partial x} + N_{yy}\frac{\partial w_0}{\partial y}) - q + I_0\frac{\partial^2 w_0}{\partial t^2} - I_2\frac{\partial^2}{\partial t^2}(\frac{\partial^2 w_0}{\partial x^2} + \frac{\partial^2 w_0}{\partial y^2}) \\
& + I_1\frac{\partial^2}{\partial t^2}(\frac{\partial u_0}{\partial x} + \frac{\partial v_0}{\partial y})\Big] dxdy.
\end{aligned} \tag{2.65}
$$

in which the virtual displacements $(\delta u_0, \delta v_0, \delta w_0)$ take the role of weight functions in the development of weak forms.

Using integration-by-parts and the gradient and divergence theorems in Equations (2.61) and (2.62), Equations (2.63), (2.64), and (2.65) are modified as

$$
\begin{aligned}
0 = & \int_{\Omega^e} \Big[\frac{\partial \delta u_0}{\partial x} N_{xx} + \frac{\partial \delta u_0}{\partial y} N_{xy} + I_0 \delta u_0 \frac{\partial^2 u_0}{\partial t^2} - I_1 \delta u_0 \frac{\partial^2}{\partial t^2}(\frac{\partial w_0}{\partial x})\Big] dxdy \\
& - \oint_{\Gamma^e} (N_{xx} n_x + N_{xy} n_y)\delta u_0 ds,
\end{aligned} \tag{2.66}
$$

$$
\begin{aligned}
0 = & \int_{\Omega^e} \Big[\frac{\partial \delta v_0}{\partial x} N_{xy} + \frac{\partial \delta v_0}{\partial y} N_{yy} + I_0 \delta v_0 \frac{\partial^2 v_0}{\partial t^2} - I_1 \delta v_0 \frac{\partial^2}{\partial t^2}(\frac{\partial w_0}{\partial y})\Big] dxdy \\
& - \oint_{\Gamma^e} (N_{xy} n_x + N_{yy} n_y)\delta v_0 ds,
\end{aligned} \tag{2.67}
$$

$$
\begin{aligned}
0 = \int_{\Omega^e} \Big[& -\frac{\partial^2 \delta w_0}{\partial x^2} M_{xx} - 2\frac{\partial^2 \delta w_0}{\partial y \partial x} M_{xy} - \frac{\partial^2 \delta w_0}{\partial^2 y} M_{yy} + \frac{\partial \delta w_0}{\partial x}(N_{xx}\frac{\partial w_0}{\partial x} + N_{xy}\frac{\partial w_0}{\partial y}) \\
& + \frac{\partial \delta w_0}{\partial y}(N_{xy}\frac{\partial w_0}{\partial x} + N_{yy}\frac{\partial w_0}{\partial y}) - \delta w_0 q + I_0 \delta w_0 \frac{\partial^2 w_0}{\partial t^2} \\
& + I_2\Big(\frac{\partial \delta w_0}{\partial x}\frac{\partial^3 w_0}{\partial x \partial t^2} + \frac{\partial w_0}{\partial y}\frac{\partial^3 w_0}{\partial y \partial t^2}\Big) - I_1\Big(\frac{\partial \delta w_0}{\partial x}\frac{\partial^2 u_0}{\partial t^2} + \frac{\partial \delta w_0}{\partial y}\frac{\partial v_0}{\partial t^2})\Big)\Big] dxdy \\
& - \oint_{\Gamma^e} \Big[\Big(\frac{\partial M_{xx}}{\partial x} + \frac{\partial M_{xy}}{\partial y} + N_{xx}\frac{\partial w_0}{\partial x} + N_{xy}\frac{\partial w_0}{\partial y}\Big) n_x \\
& + \Big(\frac{\partial M_{xy}}{\partial x} + \frac{\partial M_{yy}}{\partial y} + N_{xy}\frac{\partial w_0}{\partial x} + N_{yy}\frac{\partial w_0}{\partial y}\Big) n_y \\
& + \Big(I_1\frac{\partial^2 u_0}{\partial t^2} - I_2\frac{\partial^3 w_0}{\partial x \partial t^2}\Big) n_x + \Big(I_1\frac{\partial^2 v_0}{\partial t^2} - I_2\frac{\partial^3 w_0}{\partial y \partial t^2}\Big) n_y\Big] \delta w_0 ds \\
& + \oint_{\Gamma^e} \Big[\frac{\partial \delta w_0}{\partial x}(M_{xx} + n_x) + M_{xy} n_y) + \frac{\partial \delta w_0}{\partial y}(M_{xy} n_x + M_{yy} n_y)\Big] ds.
\end{aligned} \tag{2.68}
$$

2.5.3 Finite element model of CLPT

The approximate solutions to Equations (2.66), (2.67), and (2.68) can be expressed in terms of the nodal displacements u_j^e, v_j^e, and Δ_j^e, and can be given by

$$u_0(x,y) = \sum_{j=1}^{m} u_j^e \psi_j^e(x,y), \quad v_0(x,y) = \sum_{j=1}^{m} v_j^e \psi_j^e(x,y), \quad w_0(x,y) = \sum_{j=1}^{m} \Delta_j^e \varphi_j^e(x,y). \tag{2.69}$$

in which ψ_j^e are the Lagrange interpolation functions for the nodal degrees of freedom of u_j^e and v_j^e, and φ_j^e are the Hermite interpolation functions satisfying C^1 continuity of Δ_j^e.

Applying the laminate constitutive relation in Equation (2.23) and the approximation solutions in Equation (2.69) to Equations (2.66), (2.67) and (2.68), and rearranging the equations in a coupled matrix form, the nonlinear FEM of CLPT is given by

$$[M^e]\{\ddot{u}^e\} + [K^e]\{u^e\} = \{F^e\}, \tag{2.70}$$

or in an expanded form,

$$\begin{bmatrix} [M^{11}] & [0] & [M^{13}] \\ [0] & [M^{22}] & [M^{23}] \\ [M^{13}]^T & [M^{23}]^T & [M^{33}] \end{bmatrix} \begin{Bmatrix} \{\ddot{u}\} \\ \{\ddot{v}\} \\ \{\ddot{\Delta}\} \end{Bmatrix} + \begin{bmatrix} [K^{11}] & [K^{12}] & [K^{13}] \\ [K^{21}] & [K^{22}] & [K^{23}] \\ [K^{31}] & [K^{32}] & [K^{33}] \end{bmatrix} \begin{Bmatrix} \{u\} \\ \{v\} \\ \{\Delta\} \end{Bmatrix} = \begin{Bmatrix} \{F^1\} \\ \{F^2\} \\ \{F^3\} \end{Bmatrix}, \tag{2.71}$$

in which the nonzero elements of the stiffness matrix $[K^e]$, mass matrix $[M^e]$, and force vectors $\{F\}$ are defined as follows:

$$K_{ij}^{11} = \int_{\Omega^e} \left[A_{11} \frac{\partial \psi_i^e}{\partial x} \frac{\partial \psi_j^e}{\partial x} + A_{66} \frac{\partial \psi_i^e}{\partial y} \frac{\partial \psi_j^e}{\partial y} + A_{16} \left(\frac{\partial \psi_i^e}{\partial x} \frac{\partial \psi_j^e}{\partial y} + \frac{\partial \psi_i^e}{\partial y} \frac{\partial \psi_j^e}{\partial x} \right) \right] dxdy, \tag{2.72}$$

$$K_{ij}^{12} = \int_{\Omega^e} \left[A_{12} \frac{\partial \psi_i^e}{\partial x} \frac{\partial \psi_j^e}{\partial y} + A_{66} \frac{\partial \psi_i^e}{\partial y} \frac{\partial \psi_j^e}{\partial x} + A_{26} \frac{\partial \psi_i^e}{\partial y} \frac{\partial \psi_j^e}{\partial y} + A_{16} \frac{\partial \psi_i^e}{\partial x} \frac{\partial \psi_j^e}{\partial x} \right] dxdy = K_{ji}^{21}, \tag{2.73}$$

$$
\begin{aligned}
K_{ij}^{13} = &- \int_{\Omega^e} \Big[\frac{\partial \psi_i^e}{\partial x} \Big(B_{11} \frac{\partial^2 \varphi_j^e}{\partial x^2} + B_{12} \frac{\partial^2 \varphi_j^e}{\partial y^2} + 2B_{16} \frac{\partial^2 \varphi_j^e}{\partial x \partial y} \Big) \\
&+ \frac{\partial \psi_i^e}{\partial y} \Big(B_{16} \frac{\partial^2 \varphi_j^e}{\partial x^2} + B_{26} \frac{\partial^2 \varphi_j^e}{\partial y^2} + 2B_{66} \frac{\partial^2 \varphi_j^e}{\partial x \partial y} \Big) \Big] dxdy \\
&+ \frac{1}{2} \int_{\Omega^e} \Big\{ \frac{\partial \psi_i^e}{\partial x} \Big[A_{11} \frac{\partial w_0}{\partial x} \frac{\partial \varphi_j^e}{\partial x} + A_{12} \frac{\partial w_0}{\partial y} \frac{\partial \varphi_j^e}{\partial y} \\
&+ A_{16} \Big(\frac{\partial w_0}{\partial x} \frac{\partial \varphi_j^e}{\partial y} + \frac{\partial w_0}{\partial y} \frac{\partial \varphi_j^e}{\partial x} \Big) \Big] \\
&+ \frac{\partial \psi_i^e}{\partial y} \Big[A_{16} \frac{\partial w_0}{\partial x} \frac{\partial \varphi_j^e}{\partial x} + A_{26} \frac{\partial w_0}{\partial y} \frac{\partial \varphi_j^e}{\partial y} + A_{66} \Big(\frac{\partial w_0}{\partial x} \frac{\partial \varphi_j^e}{\partial y} + \frac{\partial w_0}{\partial y} \frac{\partial \varphi_j^e}{\partial x} \Big) \Big] \Big\} dxdy,
\end{aligned} \tag{2.74}
$$

$$
K_{ij}^{22} = \int_{\Omega^e} \Big[A_{22} \frac{\partial \psi_i^e}{\partial y} \frac{\partial \psi_j^e}{\partial y} + A_{66} \frac{\partial \psi_i^e}{\partial x} \frac{\partial \psi_j^e}{\partial x} + A_{26} \Big(\frac{\partial \psi_i^e}{\partial x} \frac{\partial \psi_j^e}{\partial y} + \frac{\partial \psi_i^e}{\partial y} \frac{\partial \psi_j^e}{\partial x} \Big) \Big] dxdy, \tag{2.75}
$$

$$
\begin{aligned}
K_{ij}^{23} = &- \int_{\Omega^e} \Big[\frac{\partial \psi_i^e}{\partial y} \Big(B_{12} \frac{\partial^2 \varphi_j^e}{\partial x^2} + B_{22} \frac{\partial^2 \varphi_j^e}{\partial y^2} + 2B_{26} \frac{\partial^2 \varphi_j^e}{\partial x \partial y} \Big) \\
&+ \frac{\partial \psi_i^e}{\partial x} \Big(B_{16} \frac{\partial^2 \varphi_j^e}{\partial x^2} + B_{26} \frac{\partial^2 \varphi_j^e}{\partial y^2} + 2B_{66} \frac{\partial^2 \varphi_j^e}{\partial x \partial y} \Big) \Big] dxdy \\
&+ \frac{1}{2} \int_{\Omega^e} \Big\{ \frac{\partial \psi_i^e}{\partial y} \Big[A_{12} \frac{\partial w_0}{\partial x} \frac{\partial \varphi_j^e}{\partial x} + A_{22} \frac{\partial w_0}{\partial y} \frac{\partial \varphi_j^e}{\partial y} \\
&+ A_{216} \Big(\frac{\partial w_0}{\partial x} \frac{\partial \varphi_j^e}{\partial y} + \frac{\partial w_0}{\partial y} \frac{\partial \varphi_j^e}{\partial x} \Big) \Big] \\
&+ \frac{\partial \psi_i^e}{\partial y} \Big[A_{16} \frac{\partial w_0}{\partial x} \frac{\partial \varphi_j^e}{\partial x} + A_{26} \frac{\partial w_0}{\partial y} \frac{\partial \varphi_j^e}{\partial y} + A_{66} \Big(\frac{\partial w_0}{\partial x} \frac{\partial \varphi_j^e}{\partial y} + \frac{\partial w_0}{\partial y} \frac{\partial \varphi_j^e}{\partial x} \Big) \Big] \Big\} dxdy,
\end{aligned} \tag{2.76}
$$

$$
\begin{aligned}
K_{ij}^{31} = &- \int_{\Omega^e} \Big[\frac{\partial \psi_j^e}{\partial x} \Big(B_{11} \frac{\partial^2 \varphi_i^e}{\partial x^2} + B_{12} \frac{\partial^2 \varphi_i^e}{\partial y^2} + 2B_{16} \frac{\partial^2 \varphi_i^e}{\partial x \partial y} \Big) \\
&+ \frac{\partial \psi_j^e}{\partial y} \Big(B_{16} \frac{\partial^2 \varphi_i^e}{\partial x^2} + B_{26} \frac{\partial^2 \varphi_i^e}{\partial y^2} + 2B_{66} \frac{\partial^2 \varphi_i^e}{\partial x \partial y} \Big) \Big] dxdy \\
&+ \int_{\Omega^e} \Big\{ \frac{\partial \psi_j^e}{\partial x} \Big[A_{11} \frac{\partial w_0}{\partial x} \frac{\partial \varphi_i^e}{\partial x} + A_{12} \frac{\partial w_0}{\partial y} \frac{\partial \varphi_i^e}{\partial y} \\
&+ A_{16} \Big(\frac{\partial w_0}{\partial x} \frac{\partial \varphi_i^e}{\partial y} + \frac{\partial w_0}{\partial y} \frac{\partial \varphi_i^e}{\partial x} \Big) \Big] \\
&+ \frac{\partial \psi_j^e}{\partial y} \Big[A_{16} \frac{\partial w_0}{\partial x} \frac{\partial \varphi_i^e}{\partial x} + A_{26} \frac{\partial w_0}{\partial y} \frac{\partial \varphi_i^e}{\partial y} + A_{66} \Big(\frac{\partial w_0}{\partial x} \frac{\partial \varphi_i^e}{\partial y} + \frac{\partial w_0}{\partial y} \frac{\partial \varphi_i^e}{\partial x} \Big) \Big] \Big\} dxdy,
\end{aligned} \tag{2.77}
$$

$$
\begin{aligned}
K_{ij}^{32} = &- \int_{\Omega^e} \Big[\frac{\partial \psi_j^e}{\partial y} \Big(B_{12} \frac{\partial^2 \varphi_i^e}{\partial x^2} + B_{22} \frac{\partial^2 \varphi_i^e}{\partial y^2} + 2B_{26} \frac{\partial^2 \varphi_i^e}{\partial x \partial y} \Big) \\
&+ \frac{\partial \psi_j^e}{\partial x} \Big(B_{16} \frac{\partial^2 \varphi_i^e}{\partial x^2} + B_{26} \frac{\partial^2 \varphi_i^e}{\partial y^2} + 2B_{66} \frac{\partial^2 \varphi_i^e}{\partial x \partial y} \Big) \Big] dxdy \\
&+ \int_{\Omega^e} \Big\{ \frac{\partial \psi_j^e}{\partial y} \Big[A_{12} \frac{\partial w_0}{\partial x} \frac{\partial \varphi_i^e}{\partial x} + A_{22} \frac{\partial w_0}{\partial y} \frac{\partial \varphi_i^e}{\partial y} \\
&+ A_{26} \Big(\frac{\partial w_0}{\partial x} \frac{\partial \varphi_i^e}{\partial y} + \frac{\partial w_0}{\partial y} \frac{\partial \varphi_i^e}{\partial x} \Big) \Big] \\
&+ \frac{\partial \psi_j^e}{\partial x} \Big[A_{16} \frac{\partial w_0}{\partial x} \frac{\partial \varphi_i^e}{\partial x} + A_{26} \frac{\partial w_0}{\partial y} \frac{\partial \varphi_i^e}{\partial y} + A_{66} \Big(\frac{\partial w_0}{\partial x} \frac{\partial \varphi_i^e}{\partial y} + \frac{\partial w_0}{\partial y} \frac{\partial \varphi_i^e}{\partial x} \Big) \Big] \Big\} dxdy,
\end{aligned} \tag{2.78}
$$

$$
\begin{aligned}
K_{ij}^{33} = &- \int_{\Omega^e} \Big[\frac{\partial^2 \varphi_i^e}{\partial x^2} \Big(D_{11} \frac{\partial^2 \varphi_j^e}{\partial x^2} + D_{12} \frac{\partial^2 \varphi_j^e}{\partial y^2} + 2D_{16} \frac{\partial^2 \varphi_j^e}{\partial x \partial y} \Big) \\
&+ \frac{\partial^2 \psi_i^e}{\partial y^2} \Big(D_{12} \frac{\partial^2 \varphi_j^e}{\partial x^2} + D_{22} \frac{\partial^2 \varphi_j^e}{\partial y^2} + 2D_{66} \frac{\partial^2 \varphi_j^e}{\partial x \partial y} \Big) \\
&+ 2 \frac{\partial^2 \psi_i^e}{\partial x \partial y} \Big(D_{16} \frac{\partial^2 \varphi_j^e}{\partial x^2} + D_{26} \frac{\partial^2 \varphi_j^e}{\partial y^2} + 2D_{66} \frac{\partial^2 \varphi_j^e}{\partial x \partial y} \Big) \Big] dxdy \\
&+ \frac{1}{2} \int_{\Omega^e} \Big\{ \Big[A_{11} \Big(\frac{\partial w_0}{\partial x} \Big)^2 + A_{12} \Big(\frac{\partial w_0}{\partial y} \Big)^2 + 2A_{16} \frac{\partial w_0}{\partial x} \frac{\partial w_0}{\partial y} \Big] \frac{\partial \varphi_i^e}{\partial x} \frac{\partial \varphi_j^e}{\partial x} \\
&+ \Big[A_{16} \Big(\frac{\partial w_0}{\partial x} \Big)^2 + A_{26} \Big(\frac{\partial w_0}{\partial y} \Big)^2 + 2A_{66} \frac{\partial w_0}{\partial x} \frac{\partial w_0}{\partial y} \Big] \Big(\frac{\partial \varphi_i^e}{\partial x} \frac{\partial \varphi_j^e}{\partial y} + \frac{\partial \varphi_j^e}{\partial x} \frac{\partial \varphi_i^e}{\partial y} \Big) \\
&+ \Big[A_{12} \Big(\frac{\partial w_0}{\partial x} \Big)^2 + A_{22} \Big(\frac{\partial w_0}{\partial y} \Big)^2 + 2A_{26} \frac{\partial w_0}{\partial x} \frac{\partial w_0}{\partial y} \Big] \frac{\partial \varphi_i^e}{\partial y} \frac{\partial \varphi_j^e}{\partial y} \Big\} dxdy \\
&- \int_{\Omega^e} \Big\{ \frac{\partial \varphi_i^e}{\partial x} \Big[\frac{\partial w_0}{\partial x} \Big(B_{11} \frac{\partial^2 \varphi_j^e}{\partial x^2} + B_{12} \frac{\partial^2 \varphi_j^e}{\partial y^2} + 2B_{16} \frac{\partial^2 \varphi_j^e}{\partial x \partial y} \Big) \\
&+ \frac{\partial w_0}{\partial y} \Big(B_{16} \frac{\partial^2 \varphi_j^e}{\partial x^2} + B_{26} \frac{\partial^2 \varphi_j^e}{\partial y^2} + 2B_{66} \frac{\partial^2 \varphi_j^e}{\partial x \partial y} \Big) \Big] \\
&+ \frac{\partial \varphi_i^e}{\partial y} \Big[\frac{\partial w_0}{\partial y} \Big(B_{12} \frac{\partial^2 \varphi_j^e}{\partial x^2} + B_{22} \frac{\partial^2 \varphi_j^e}{\partial y^2} + 2B_{26} \frac{\partial^2 \varphi_j^e}{\partial x \partial y} \Big) \\
&+ \frac{\partial w_0}{\partial x} \Big(B_{16} \frac{\partial^2 \varphi_j^e}{\partial x^2} + B_{26} \frac{\partial^2 \varphi_j^e}{\partial y^2} + 2B_{66} \frac{\partial^2 \varphi_j^e}{\partial x \partial y} \Big) \Big] \Big\} dxdy \\
&- \frac{1}{2} \int_{\Omega^e} \Big\{ \frac{\partial^2 \psi_i^e}{\partial x^2} \Big[B_{11} \frac{\partial w_0}{\partial x} \frac{\partial \varphi_j^e}{\partial x} + B_{12} \frac{\partial w_0}{\partial y} \frac{\partial \varphi_j^e}{\partial y} + B_{16} \Big(\frac{\partial w_0}{\partial y} \frac{\partial \varphi_j^e}{\partial x} + \frac{\partial w_0}{\partial x} \frac{\partial \varphi_j^e}{\partial y} \Big) \Big] \\
&+ \frac{\partial^2 \psi_i^e}{\partial y^2} \Big[B_{12} \frac{\partial w_0}{\partial x} \frac{\partial \varphi_j^e}{\partial x} + B_{22} \frac{\partial w_0}{\partial y} \frac{\partial \varphi_j^e}{\partial y} + B_{26} \Big(\frac{\partial w_0}{\partial y} \frac{\partial \varphi_j^e}{\partial x} + \frac{\partial w_0}{\partial x} \frac{\partial \varphi_j^e}{\partial y} \Big) \Big] \\
&+ 2 \frac{\partial^2 \psi_i^e}{\partial x \partial y} \Big[B_{16} \frac{\partial w_0}{\partial x} \frac{\partial \varphi_j^e}{\partial x} + B_{26} \frac{\partial w_0}{\partial y} \frac{\partial \varphi_j^e}{\partial y} + B_{66} \Big(\frac{\partial w_0}{\partial y} \frac{\partial \varphi_j^e}{\partial x} + \frac{\partial w_0}{\partial x} \frac{\partial \varphi_j^e}{\partial y} \Big) \Big] \Big\} dxdy,
\end{aligned} \tag{2.79}
$$

$$M_{ij}^{11} = \int_{\Omega^e} I_0 \psi_i^e \psi_j^e dxdy, \tag{2.80}$$

$$M_{ij}^{13} = -\int_{\Omega^e} I_1 \psi_i^e \frac{\partial \varphi_j^e}{\partial x} dxdy, \tag{2.81}$$

$$M_{ij}^{22} = \int_{\Omega^e} I_0 \psi_i^e \psi_j^e dxdy, \tag{2.82}$$

$$M_{ij}^{23} = -\int_{\Omega^e} I_1 \psi_i^e \frac{\partial \varphi_j^e}{\partial y} dxdy, \tag{2.83}$$

$$M_{ij}^{33} = \int_{\Omega^e} \Big[I_0 \varphi_i^e \varphi_j^e + I_2 \Big(\frac{\partial \varphi_i^e}{\partial x} \frac{\partial \varphi_j^e}{\partial x} + \frac{\partial \varphi_i^e}{\partial y} \frac{\partial \varphi_j^e}{\partial y} \Big) \Big] dxdy, \tag{2.84}$$

$$F_i^1 = \oint_{\Gamma^e} N_n \psi_i^e ds, \tag{2.85}$$

$$F_i^2 = \oint_{\Gamma^e} N_s \psi_i^e ds, \tag{2.86}$$

$$F_i^3 = \oint_{\Omega^e} q \varphi_i^e dxdy + \oint_{\Gamma^e} \Big(V_n \varphi_i^e - M_n \frac{\partial \varphi_i^e}{\partial n} \Big) ds, \tag{2.87}$$

in which

$$N_n = N_{xx} n_x + N_{xy} n_y, \tag{2.88}$$

$$N_s = N_{xy} n_x + N_{yy} n_y, \tag{2.89}$$

$$V_n = Q_n + \frac{\partial M_{ns}}{\partial s} + \Big(N_{xx} \frac{\partial w_0}{\partial x} + N_{xy} \frac{\partial w_0}{\partial y} \Big) n_x + \Big(N_{xy} \frac{\partial w_0}{\partial x} + N_{yy} \frac{\partial w_0}{\partial y} \Big) n_y, \tag{2.90}$$

$$M_n = M_{xx} n_x + M_{xy} n_y, \tag{2.91}$$

$$M_s = M_{xy} n_x + M_{yy} n_y. \tag{2.92}$$

The FEM in Equation (2.70) is nonlinear since $[K^e]$ depends on displacements.

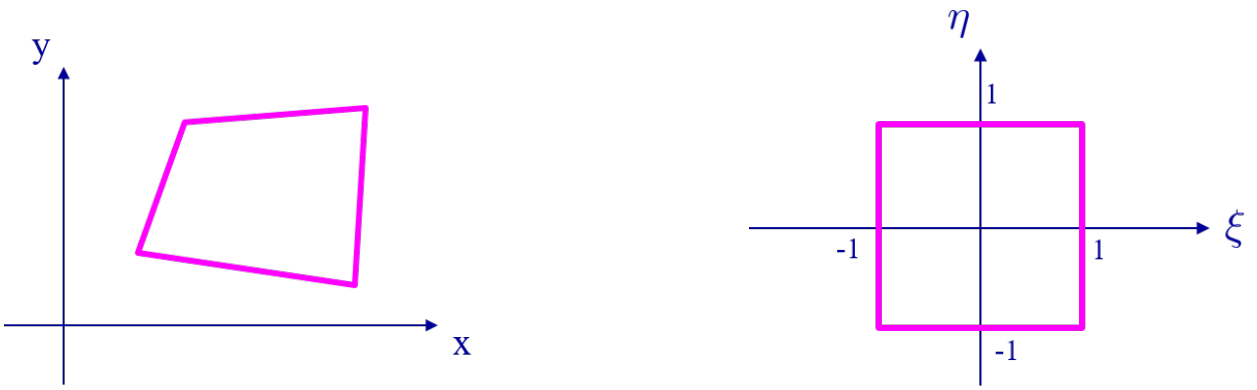

(a) Real element. (b) Reference element.

Figure 2.4: Real and reference elements for isoparametric mapping.

2.5.4 Transformation of derivatives

In this work, the FEM in Equations (2.70) to (2.92) were formulated using the isoparametric form [35, 36]. The first derivatives can be transformed between real elements (in terms of x and y) and reference elements (in terms of ξ and η) using the well-known Jacobian matrix $[J]$:

$$\begin{Bmatrix} \frac{\partial}{\partial \xi} \\ \frac{\partial}{\partial \eta} \end{Bmatrix} = \begin{bmatrix} \frac{\partial x}{\partial \xi} & \frac{\partial y}{\partial \xi} \\ \frac{\partial x}{\partial \eta} & \frac{\partial y}{\partial \eta} \end{bmatrix} \begin{Bmatrix} \frac{\partial}{\partial x} \\ \frac{\partial}{\partial y} \end{Bmatrix} = \begin{bmatrix} J_{11} & J_{12} \\ J_{21} & J_{22} \end{bmatrix} \begin{Bmatrix} \frac{\partial}{\partial x} \\ \frac{\partial}{\partial y} \end{Bmatrix} = [J] \begin{Bmatrix} \frac{\partial}{\partial x} \\ \frac{\partial}{\partial y} \end{Bmatrix}, \tag{2.93}$$

$$\begin{Bmatrix} \frac{\partial}{\partial x} \\ \frac{\partial}{\partial y} \end{Bmatrix} = \begin{bmatrix} j_{11} & j_{12} \\ j_{21} & j_{22} \end{bmatrix} \begin{Bmatrix} \frac{\partial}{\partial \xi} \\ \frac{\partial}{\partial \eta} \end{Bmatrix} = [j] \begin{Bmatrix} \frac{\partial}{\partial \xi} \\ \frac{\partial}{\partial \eta} \end{Bmatrix}, \tag{2.94}$$

$$[j] = [J]^{-1}. \tag{2.95}$$

The transformation of the second derivatives is explained in [34] and [36]. Following the method of Dhatt in [36],

$$\begin{Bmatrix} \frac{\partial^2}{\partial x^2} \\ \frac{\partial^2}{\partial y^2} \\ \frac{\partial^2}{\partial x \partial y} \end{Bmatrix} = [T_1] \begin{Bmatrix} \frac{\partial}{\partial \xi} \\ \frac{\partial}{\partial \eta} \end{Bmatrix} + [T_2] \begin{Bmatrix} \frac{\partial^2}{\partial \xi^2} \\ \frac{\partial^2}{\partial \eta^2} \\ \frac{\partial^2}{\partial \xi \partial \eta} \end{Bmatrix}, \tag{2.96}$$

in which $[T_1]$ and $[T_2]$ are

$$[T_1] = -[T_2][C_1][j], \tag{2.97}$$

$$[T_2] = \begin{bmatrix} j_{11}^2 & j_{12}^2 & 2j_{11}j_{12} \\ j_{21}^2 & j_{22}^2 & 2j_{21}j_{22} \\ j_{11}j_{21} & j_{12}j_{22} & j_{11}j_{22} + j_{12}j_{21} \end{bmatrix}, \tag{2.98}$$

$$[C_1] = \begin{bmatrix} \frac{\partial}{\partial \xi} < J_{11} \ J_{12} > \\ \frac{\partial}{\partial \eta} < J_{21} \ J_{22} > \\ \frac{1}{2}\left(\frac{\partial}{\partial \eta} < J_{11} \ J_{12} > + \frac{\partial}{\partial \xi} < J_{21} \ J_{22} > \right) \end{bmatrix}. \tag{2.99}$$

2.6 Summary

This chapter derived the necessary governing equations (Equations (2.35) to (2.37)) and its boundary conditions (Equations (2.51) and (2.52)). Then, the nonlinear FEM (Equations (2.70) to (2.92)) was developed based on the governing equations. Applying high-precision cubic Hermite elements to this model and then solving the model for static and dynamic analyses are discussed in Chapter 4.

Chapter 3

EXPERIMENT OF SNAP-THROUGH OF POST-BUCKLED THIN LAMINATED COMPOSITE PLATES

3.1 Introduction

Unlike isotropic materials such as steel and aluminum which have well-defined material properties, the material properties of composite structures are notoriously variable. Thus, in experiments using composite specimens, controlling the quality of the specimens (e.g., designed angles of layers, uniform thickness of laminates, removal of undesired substances between layers, etc.), and finding and verifying the material properties of the specimens are important steps.

In this work, laminated composite plate specimens were fabricated in the Composites Lab at the University of Washington (UW). The in-house fabrication led to quality assurance and enabled the specimens to have complicated shapes including spacers. In addition, the material properties of the specimens were verified through: (i) tensile load tests; (ii) static cantilever tests, and (iii) free vibration tests.

The experiments of post-buckled thin laminated composite plate specimens were conducted in the UW Structural Vibrations Lab (named *the UW Lab*) and at the Air Force Research Laboratory (named *AFRL*). The test data from the UW Lab were obtained using a single-point displacement-sensing laser, Micro-epsilon optoNCDT 1700-500. The test was exploratory to acquire a qualitative understanding and to describe experimental methods since the full-field measurement of the buckled shape used in the test could not be char-

acterized and thus the test data could not be compared quantitatively with the modeling results. The snap-through boundaries were established using the data and then their characteristics were investigated. The experimental data from AFRL were collected using a double-point laser vibrometer (velocity-sensing), Polytec OFV 512, and two digital image correlation (DIC) cameras, Photron FASTCAM SA5. The equipment used in the two labs is listed in Table 3.1. The DIC technique was applied to obtain the full-field measurement of the buckled shape and dynamic response of the post-buckled specimen. The technique inherently generates a large data set and thus leads to high computational costs of transferring and analyzing the data. As a result, to find snap-through boundaries of the post-buckled specimen, frequency-sweep tests were performed using the vibrometer instead of using the DIC cameras. Some of the vibrometer measurements were compared to the corresponding DIC data for verification purposes.

Table 3.1: A list of the lab equipment

Equipment	Model Name	Named	Test Location
One single-point displacement-sensing laser	Micro-epsilon optoNCDT 1700-500	*Single-point laser*	UW Lab
One double-point laser vibrometer (velocity-sensing)	Polytec OFV 512	*Vibrometer*	AFRL
Two DIC cameras	Photron FASTCAM SA5	*DIC cameras*	AFRL

3.2 Fabrication of Laminated Composite Plate Specimens

All the specimens tested in this work were fabricated in-house to achieve controlled quality assurance and to create complicated specimen shapes. The specimens had the shape of a 'castle' in chess, as shown in Figures 3.2a and 3.2c, since the shape includes spacers (or shims)

(a) Fabric cutter.

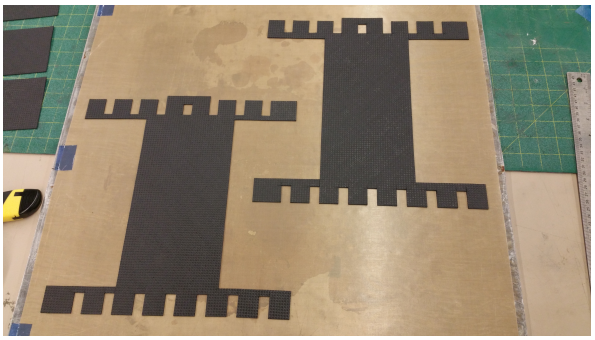

(b) Laid-up prepreg.

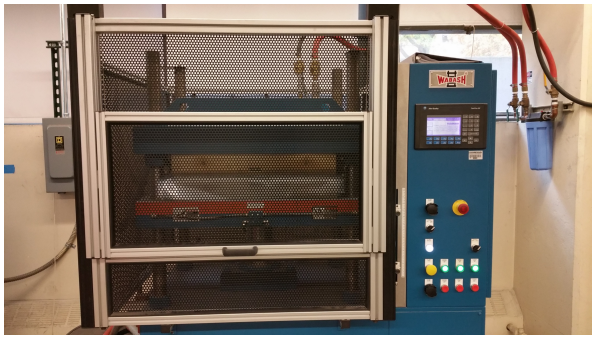

(c) Hot press.

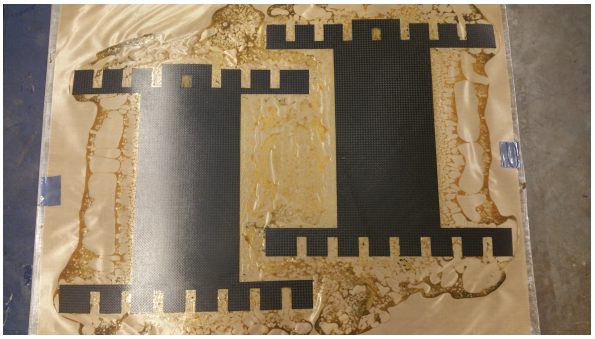

(d) Cured prepreg.

Figure 3.1: In-house fabrication of laminated composite plates in the Composites Lab at the University of Washington.

to prevent slippage along clamped boundaries as shown in Figure 3.2b. In the fabrication process, prepregs were cut using the fabric cutter (Figure 3.1a) to make precise dimensions and straight edges. After laying the cut layers according to designed angles (Figure 3.1b), the laid-up prepregs were put in the hot press and cured following the temperature cycles specified by the manufacturer (Figure 3.1c).

Since the clamps used in the UW Lab and at AFRL had different dimensions, two types of plate specimens were fabricated as shown in Table 3.2 and Figure 3.2. The one used in the UW Lab was named *the UW plate* while the other used at AFRL was labeled *the AFRL plate*.

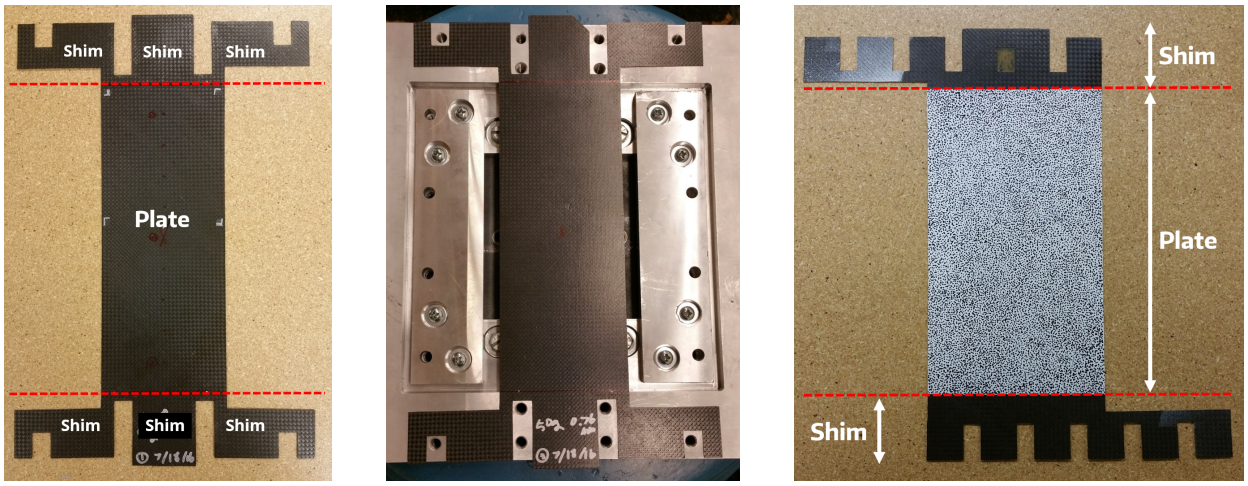

(a) UW plate specimen.

(b) UW plate on the bottom clamp.

(c) AFRL plate specimen.

Figure 3.2: *UW plate* and *AFRL plate* specimens.

Table 3.2: Geometrical properties of the specimens

	UW Plate	AFRL Plate
Material	T800H-6K/3900-2	T800H-6K/3900-2
Layup	$[45]_4$	$[45]_4$
Length, a	254 mm	228.6 mm
Width, b	101.6 mm	127 mm
Thickness, h	0.72 mm	0.72 mm

3.3 Evaluation and verification of material properties

3.3.1 Predicted material properties

All the laminated composite plate specimens tested in this work were fabricated using the woven prepreg, TORAYCA T800H-6K/3900-2 (BMS 8-276) (named *the weave*), which has

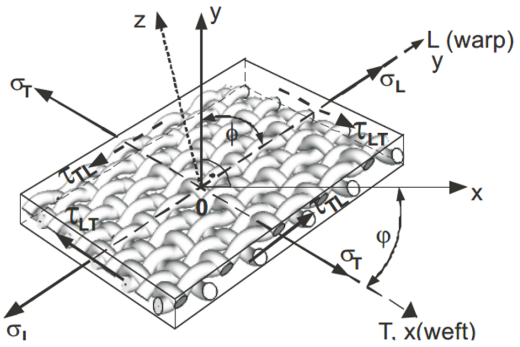

(a) Plain weave pattern. Photo courtesy of Penava. [37]

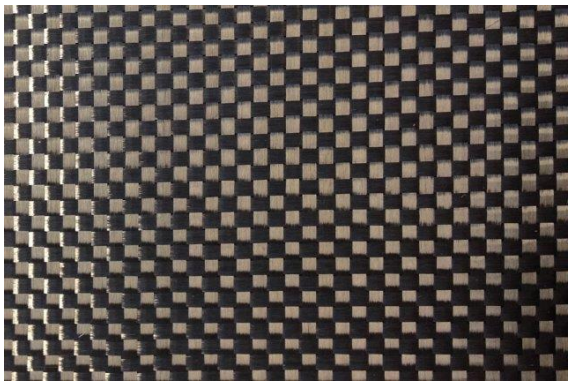

(b) Plain weave prepreg TORAYCA T800H-6K/3900-2 (BMS 8-276).

Figure 3.3: Plain weave prepreg TORAYCA T800H-6K/3900-2 (BMS 8-276).

a plain weave pattern as shown in Figure 3.3. The fabric pattern is the simplest available and is the most commonly used [32]. The material properties of the unidirectional prepreg (named *the uni*) consisting of the same fibers and epoxy used in the weave were reported in several papers [38, 39, 40]; however, the properties of this weave have not been found in the literature. In this work, to address this issue, it was assumed that the material properties of the weave (thickness t) can be estimated by calculating material properties of a symmetric laminate $[0/90]_{\frac{n}{4}S}$[1] having n uni layers (thickness t/n) as illustrated in Figure 3.4. The material properties predicted based on this assumption were verified by three types of tests described in the following sections.

The material properties of the uni tabulated in Table 3.3 were obtained from the work of Kobayashi et al. in [38]. Using the properties, the effective properties of the weave were calculated by following Tuttle's work in [32]. He explained that considering a laminate subjected to uni-axial loading N_{xx} and using Equation (2.22), the effective extensional Young's

[1] 0 and 90 indicate the fiber angle of the corresponding layers. $\frac{n}{4}$ represents the number of repetition of the [0/90] sequence. The subscript S means a symmetric stack sequence. For example, $[0/90]_{2S}$ can be expanded as [0/90/0/90/90/0/90/0].

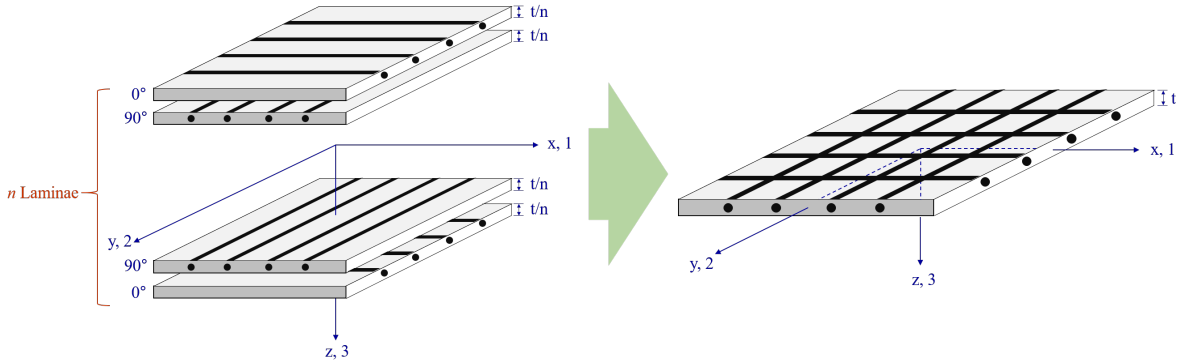

Figure 3.4: A symmetric laminate consisting of n unidirectional laminae and its corresponding weave lamina.

Table 3.3: Material properties of the uni presented in [38]

Material property	Value
Longitudinal Young's Modulus, E_{11}	143 GPa
Transverse Young's Modulus, E_{22}	7.99 GPa
In-plane Shear Modulus, G_{12}	3.96 GPa
In-plane Poisson's Ratio, ν_{12}	0.345
Out-of-plane Poisson's Ratio, ν_{12}	0.490

modulus in the x-axis direction, $\bar{E}^{ex}_{xx}$, is given by

$$\bar{E}^{ex}_{xx} = \frac{\bar{\sigma}_{xx}}{\varepsilon^0_{xx}} = \frac{N_{xx}/t}{a_{11}N_{xx}} = \frac{1}{ta_{11}}. \tag{3.1}$$

In addition, assuming an isotropic plate under a pure bending, i.e., $E_{11} = E_{22} = E$, $\nu_{12} = \nu_{21}$, and G_{12}, the effective flexural Young's modulus in the x-direction, $\bar{E}^{fl}_{xx}$, is given

by

$$D_{11} = \frac{\bar{E}^{fl}_{xx} t^3}{12(1-\nu^2)}, \qquad d_{11} = \frac{1}{D_{11}(1-\nu^2)} = \frac{12}{\bar{E}^{fl}_{xx} t^3},$$
$$\bar{E}^{fl}_{xx} = \frac{12}{d_{11} t^3}. \tag{3.2}$$

For the completeness, the effective extensional properties of a composite laminate Tuttle defined in [32] are given by

$$\bar{E}^{ex}_{xx} = \frac{\bar{\sigma}_{xx}}{\varepsilon^0_{xx}} = \frac{1}{t a_{11}}, \qquad \bar{E}^{ex}_{yy} = \frac{\bar{\sigma}_{yy}}{\varepsilon^0_{yy}} = \frac{1}{t a_{22}},$$
$$\bar{\nu}^{ex}_{xy} = \frac{-\varepsilon^0_{yy}}{\varepsilon^0_{xx}} = \frac{-a_{12}}{a_{11}}, \qquad \bar{\nu}^{ex}_{yx} = \frac{-\varepsilon^0_{xx}}{\varepsilon^0_{yy}} = \frac{-a_{12}}{a_{22}}, \tag{3.3}$$
$$\bar{G}_{xy} = \frac{\bar{\tau}_{xy}}{\gamma^0_{xy}} = \frac{1}{t a_{66}},$$

and the effective flexural properties are given by

$$\bar{E}^{fl}_{xx} = \frac{12}{d_{11} t^3}, \qquad \bar{E}^{fl}_{yy} = \frac{12}{d_{22} t^3},$$
$$\bar{\nu}^{fl}_{xy} = \frac{-d_{12}}{d_{11}}, \qquad \bar{\nu}^{fl}_{yx} = \frac{-d_{12}}{d_{22}}. \tag{3.4}$$

Applying the properties presented in Table 3.3 into Equations (3.3) and (3.4), the effective extensional properties and the effective flexural properties were calculated. Both properties converged to the same value as the number of plies n went to the infinity. Based on the initial assumption, the material properties of the weave were assumed to agree with these effective properties which are tabulated in Table 3.4. The superscripts *ex* and *fl* were removed from the table since they are identical.

3.3.2 Tensile load test

To verify the computed properties in Table 3.4, tensile tests were conducted using an Instron 5585H and an extensometer as shown in Figure 3.5. Four specimens having the dimensions

Table 3.4: Computed material properties of the weave

Material property	Value
Longitudinal Young's Modulus, $\bar{E}_{xx}$	75.9 GPa
Transverse Young's Modulus, $\bar{E}_{yy}$	75.9 GPa
In-plane Shear Modulus, $\bar{G}_{xy}$	3.96 GPa
In-plane Poisson's Ratio, $\bar{\nu}_{xy}$	0.037
Out-of-plane Poisson's Ratio, $\bar{\nu}_{yx}$	0.037

of 254 mm x 25.4 mm x 0.9 mm were tested. Two of them were $[0]_5$ with the others being $[45]_5$. The strains obtained from the tensile load tests and the strains predicted using the material properties shown in Table 3.4 are compared in Table 3.5. The specimens 1, 3, and 4 which were pulled up to $\varepsilon_e \simeq 0.0055$ and which did not fail showed errors within 2.8% while the specimen 2 which failed at $\varepsilon_e = 0.01071$ as shown in Figure 3.5c demonstrated a relatively larger error, 6.79%.

Table 3.5: Tensile load test results of the specimens (254 mm x 25.4 mm x 0.9 mm)

	Layup	Load (kN)	Experimental Strain (ε_e)	Modeling Strain (ε_m)	Error (%)
Specimen 1	$[0]_5$	10.0	0.00545	0.005587	-2.51
Specimen 2	$[0]_5$	20.9	0.01071 (failed)	0.011437	-6.79
Specimen 3	$[45]_5$	1.8	0.00553	0.005377	2.77
Specimen 4	$[45]_5$	1.9	0.00564	0.005733	-1.65

3.3.3 Static cantilever test

Using the material properties shown in Table 3.4 and Equations (2.19), (2.20), and (2.21), the laminate stiffnesses of a cantilever specimen (Figure 3.6a) were evaluated and are tabulated in Table 3.6.

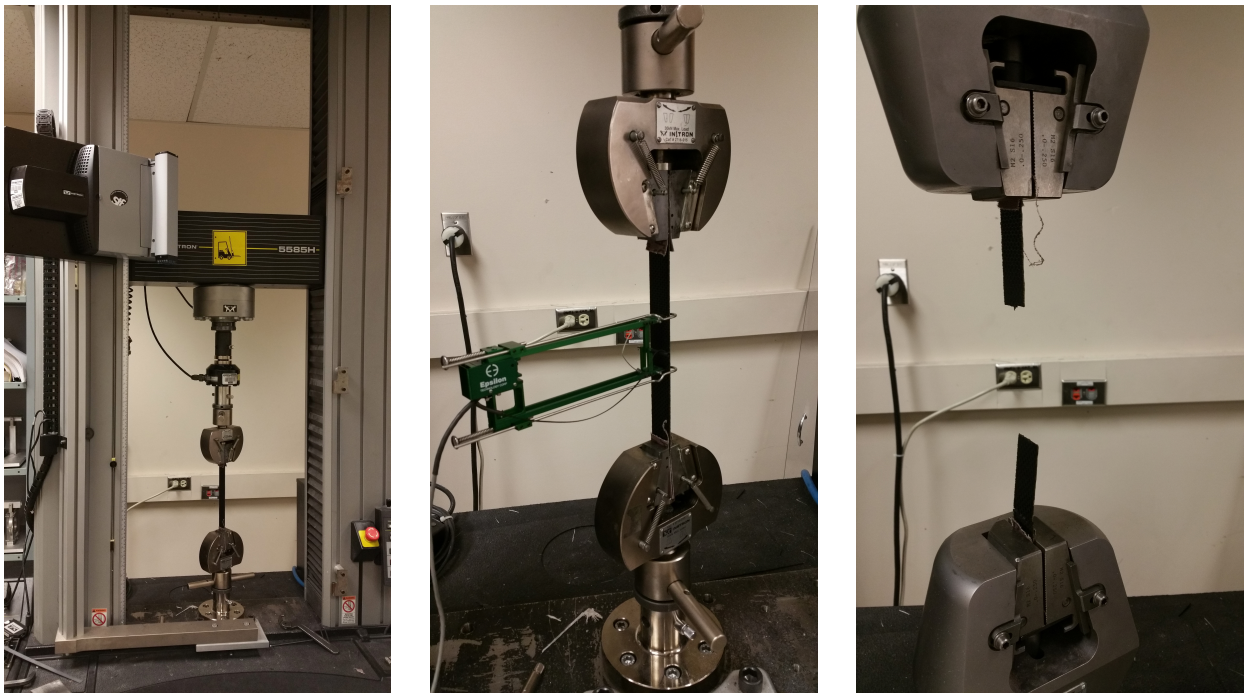

(a) Instron 5585H. (b) Extensometer. (c) Final fracture of the specimen.

Figure 3.5: Tensile load test using an Instron 5585H and an extensometer.

Table 3.6: Laminate stiffnesses of the cantilever specimen (170 mm x 89.5 x 0.72 mm)

	Extensional stiffnesses (Pa-m)		Coupling stiffnesses (Pa-m^2)		Bending stiffnesses (Pa-m^3)
A_{11}	0.31225×10^8	B_{11}	0	D_{11}	0.13489×10^1
A_{12}	0.25523×10^8	B_{12}	0	D_{12}	0.11026×10^1
A_{16}	0	B_{16}	0	D_{16}	0
A_{22}	0.31225×10^8	B_{22}	0	D_{22}	0.13489×10^1
A_{26}	0	B_{26}	0	D_{26}	0
A_{66}	0.26349×10^8	B_{66}	0	D_{66}	0.11383×10^1

In the experiment, the displacements of the cantilever under static loading applied to the middle of the tip were measured using the single-point laser. A nonlinear FEM created using Equations (2.70) to (2.92) was evaluated using MATLAB [41]. In the model, the cantilever

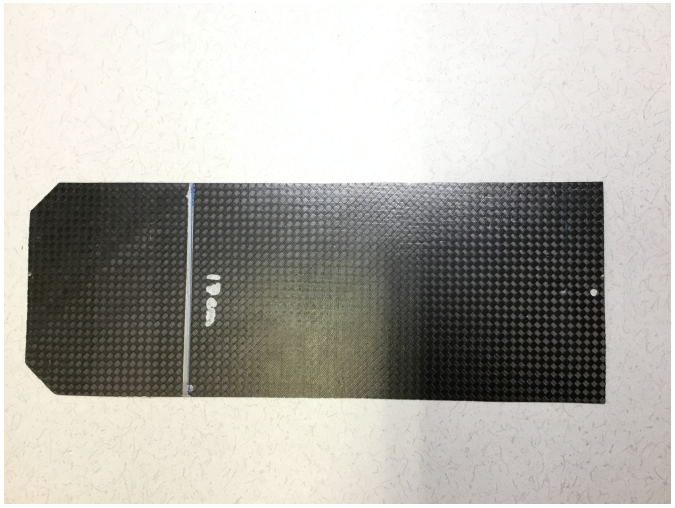

(a) Specimen of cantilever test.

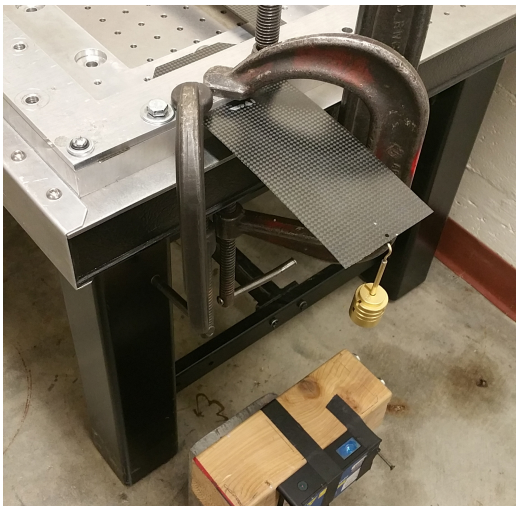

(b) Experimental setup.

Figure 3.6: Experimental setup of the static cantilever test.

specimen was modeled using 3,900 elements (65 in x-axis $\times$ 60 in y-axis) as shown in Figure 3.7c. Self-weight loading was first applied as illustrated in Figure 3.7a to capture the initial displacement due to gravity and then additional point loading was applied to the middle of the tip of the cantilever as illustrated in 3.7b.

The experimental and modeling results of the cantilever test are tabulated in Table 3.7 and are illustrated in Figure 3.8. The modeling results showed typically less than 6 % variance from the test results. At the end of the loading range, the load-displacement curve of the model showed a trend of deviating from the experimental curve since the model predicted more stiffness hardening (i.e., more nonlinearity) in that loading range than the experimental data showed.

3.3.4 Free vibration test

As the final step of the verification of the material properties presented in Table 3.4, free vibration tests of the cantilever specimen were conducted using the same experimental setup

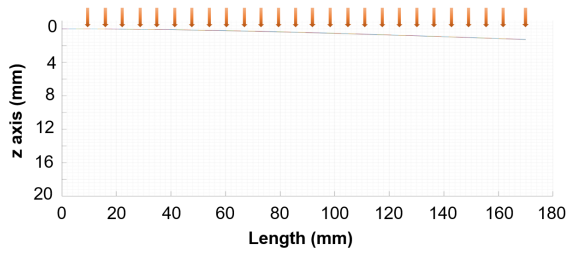

(a) Self-weight loading application.

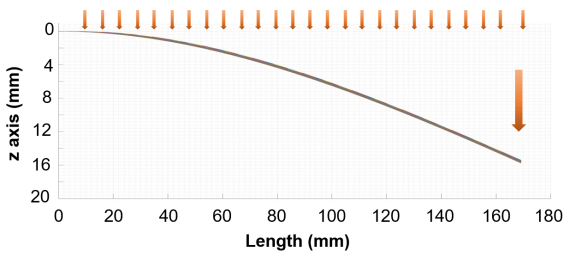

(b) Additional point load application to the middle of the tip.

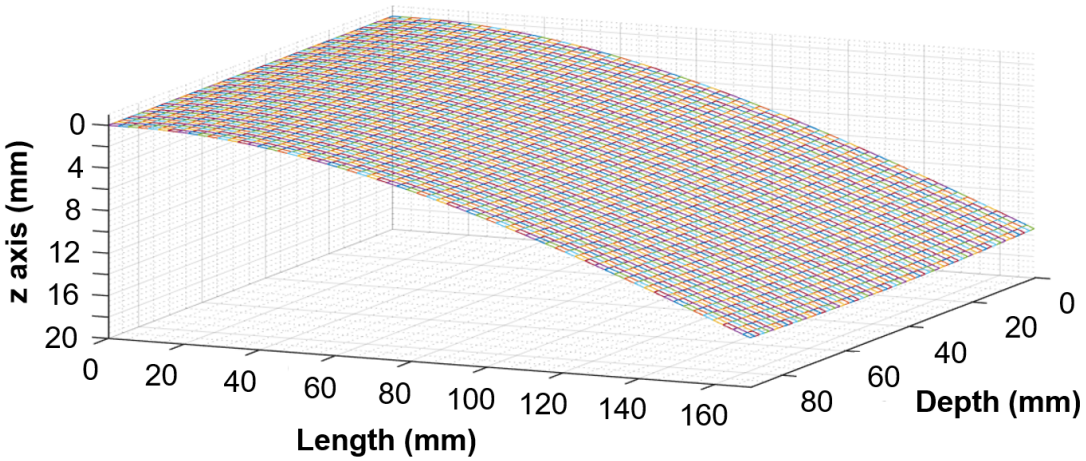

(c) Deformed shape of the cantilever specimen (65 × 60 elements).

Figure 3.7: Modeling results of the static cantilever test.

shown in Figure 3.6b. In the experiment, the specimens were subjected to impact loading at the middle of the tip and the dynamic response of the cantilever specimen was measured using the single-point laser. The fast Fourier transform (FFT) of the response was taken to obtain the natural frequency of the specimen. Although the free vibration decay response is not steady-state, the FFT provides a good approximation. The nonlinear FEM illustrated in Figure 3.7c was used to evaluate the natural frequency of the specimen. The experimental and modeling results are illustrated in Figure 3.9 and are tabulated in Table 3.8.

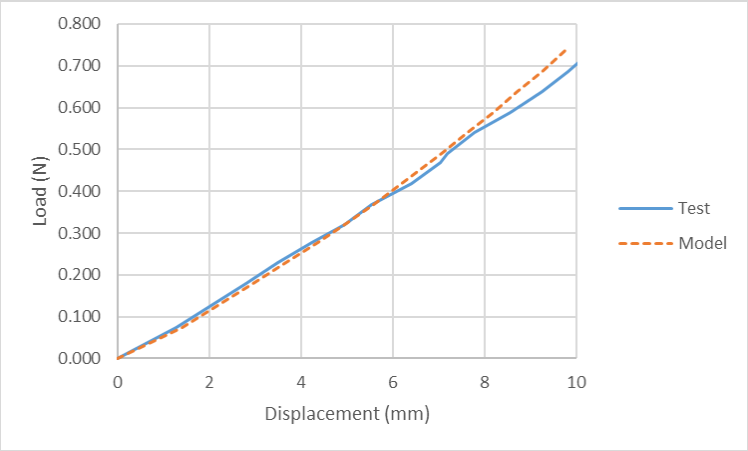

Figure 3.8: Load vs. transverse displacement curves from the experimental data and modeling results.

Table 3.7: Transverse displacements of the cantilever specimen measured from the experiment and model

Load (N)	Experiment (mm)	Modeling (mm)	Variance (mm)	Error (%)
0	0	0	0	0
0.075	1.2775	1.3963	-0.1188	-9.30
0.180	2.8043	2.9521	-0.1478	-5.27
0.229	3.4897	3.6757	-0.1860	-5.33
0.278	4.2375	4.3668	-0.1293	-3.05
0.320	4.9542	4.9442	0.0100	0.20
0.369	5.5462	5.5835	-0.0373	-0.67
0.418	6.4186	6.1995	0.2191	3.41
0.467	7.0418	6.7945	0.2473	3.51
0.491	7.1976	7.0677	0.1299	1.80
0.540	7.7896	7.6359	0.1537	1.97
0.589	8.5686	8.1879	0.3807	4.44
0.638	9.2541	8.7250	0.5291	5.72
0.687	9.8149	9.2485	0.5664	5.77
0.736	10.3446	9.7595	0.5851	5.66

Table 3.8: First natural frequency of the specimen from the experiment and model

Boundary Condition	Experiment	Model	Error
CFFF	18.349 Hz	17.569 Hz	4.44%

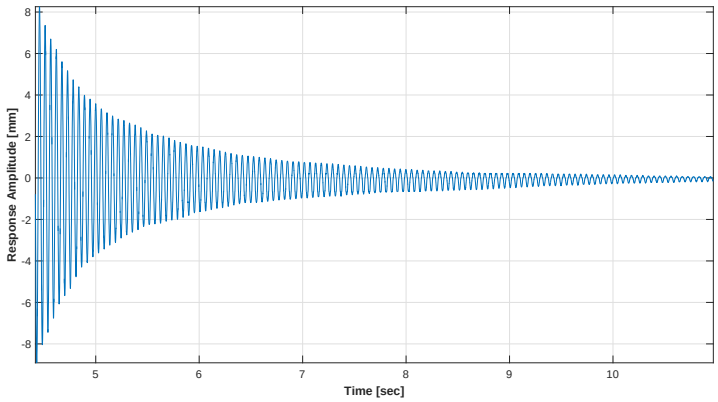

(a) Time-response plot of the free vibration test.

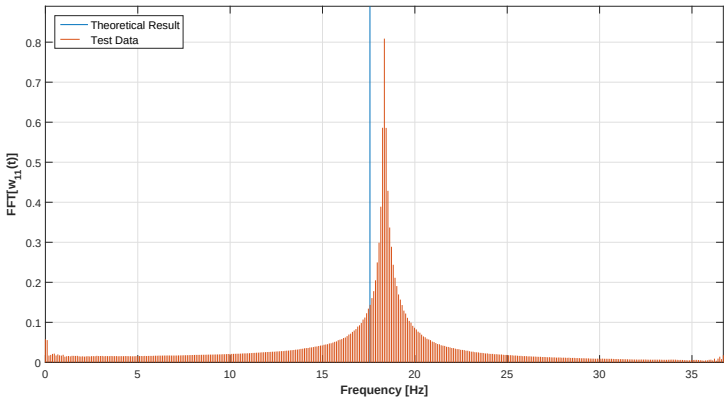

(b) Fourier transform plot of the free vibration test.

Figure 3.9: Free vibration test results.

3.3.5 Results of the verification of material properties

As presented in the previous sections, the experimental results obtained from the tensile load tests, static cantilever tests, and free vibration tests showed a good agreement with the modeling results computed using the material properties shown in Table 3.4. In case of metal, which possesses well-known material properties and whose uniform quality is assured, this argument would be readily challenged. However, considering that the material properties of anisotropic composite laminates are notoriously nonuniform and variable, the errors between the experimental data and modeling results presented in this section can be deemed reasonable and acceptable. Thus, these material properties were used in Chapter 4 to model snap-through of post-buckled composite plates.

3.4 Exploratory investigation of snap-through boundaries

The experiments of snap-through of post-buckled plate specimens conducted at the UW Lab used the single-point laser. Since the full-field measurement of the initially buckled shape and deformed shapes of the specimen could not be obtained, this experiment was exploratory and thus the experimental data were not compared with the modeling results. However, the snap-through boundaries established using the data provide a good sense of the important characteristics of the behavior of post-buckled plates.

3.4.1 Experimental Setup

In this experiment, the UW plate (Figure 3.2a and Table 3.2) was used as the specimen. The specimen was clamped along $x = 0$ and $x = a$ and was free along $y = 0$ and $y = b$ as shown in Figure 3.11, in which a and b are specified in Table 3.2. Thus, the boundary conditions are CCFF, in which C and F stand for clamped and free, respectively.

As shown in Figure 3.10, the clamp was mounted on the electrodynamic shaker, MB C10 which applied a harmonic loading to the clamp. Consequently, the loading was inertially

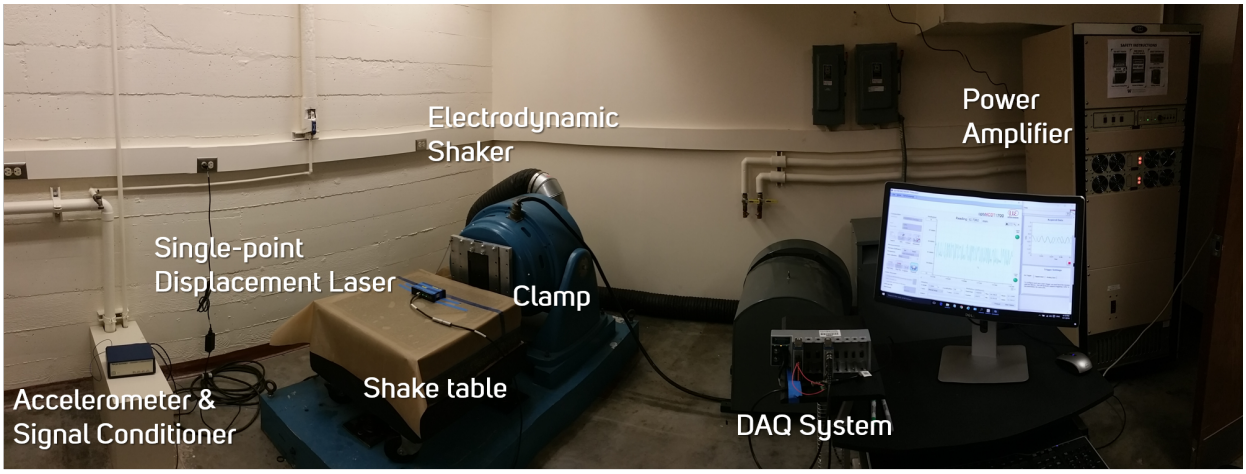

Figure 3.10: Experimental setup in the UW Lab.

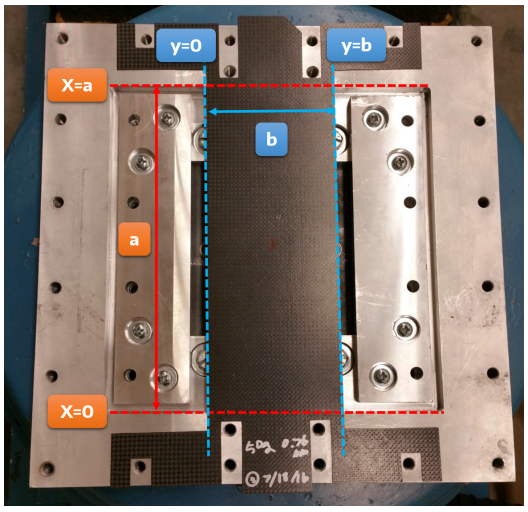

(a) UW plate on clamp.

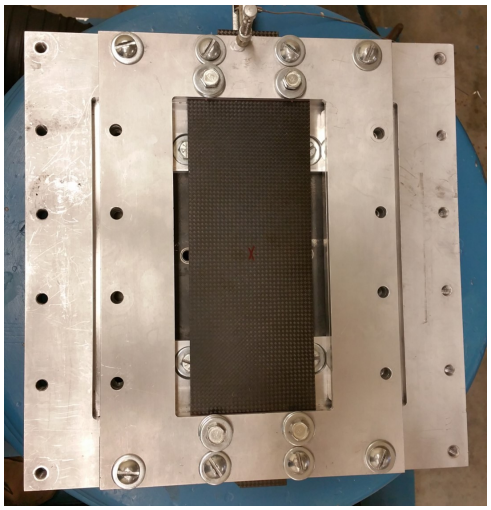

(b) Boundary conditions: CCFF.

Figure 3.11: Boundary conditions of the specimen, the UW plate.

applied to the specimen in the clamp. The corresponding dynamic response of the specimen was captured by the single-point laser.

The plate specimen was buckled by pushing the small tab protruding from the top of the clamp downward with an axial load as shown in Figure 3.12. While applying axial loading,

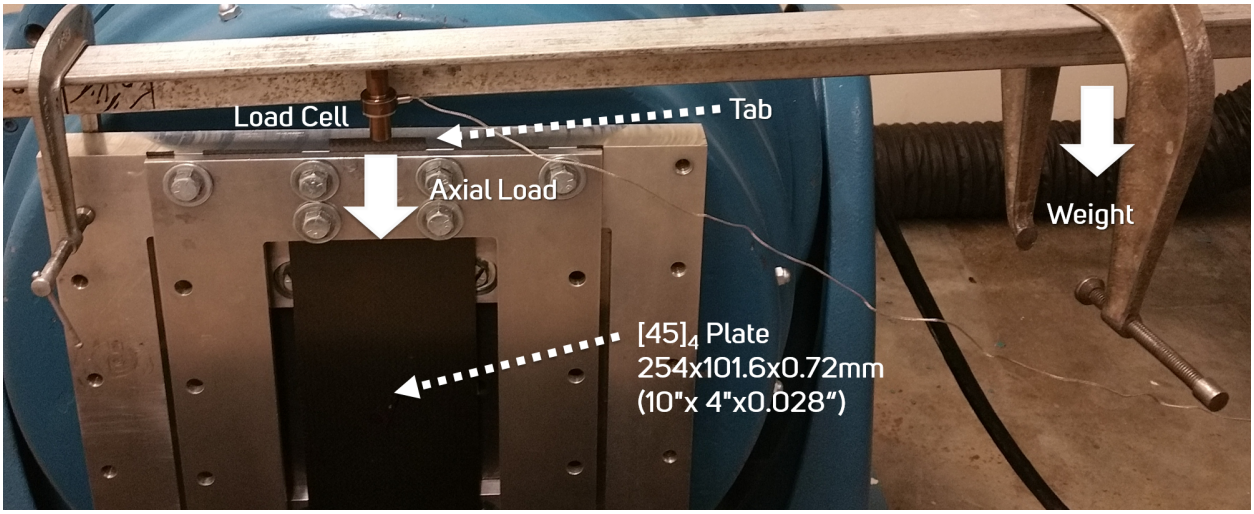

Figure 3.12: Buckling process and measurement of axial loads with a load cell.

the axial load and buckled depth of the midpoint of the specimen were monitored by the load cell and laser. The final peak-to-peak displacement of the midpoint was 1.90 mm and the corresponding axial load was 54.6 N.

3.4.2 Experimental data

In this section, the methodology of the snap-through boundary analysis is explained by taking an example of the forcing amplitude-ramp experiment with the 105 Hz forcing frequency. Figure 3.13 illustrates the dynamic response of the midpoint of the plate specimen under 105 Hz harmonic loading. At a small loading amplitude, the plate showed a single-well response. As the loading amplitude was continuously increased, the response amplitude also increased. When the loading amplitude reached 13.6 g, the plate began to demonstrate chaotic behaviors with chaotic snap-through. When the loading amplitude was further increased to 25.4 g, the plate started to show periodic snap-through. Considering the thickness of the plate is 0.72 mm, the peak-to-peak response amplitude of the periodic snap-through, 6.76 mm, is significant. After reaching this threshold (named *the threshold 1*) where a transition from

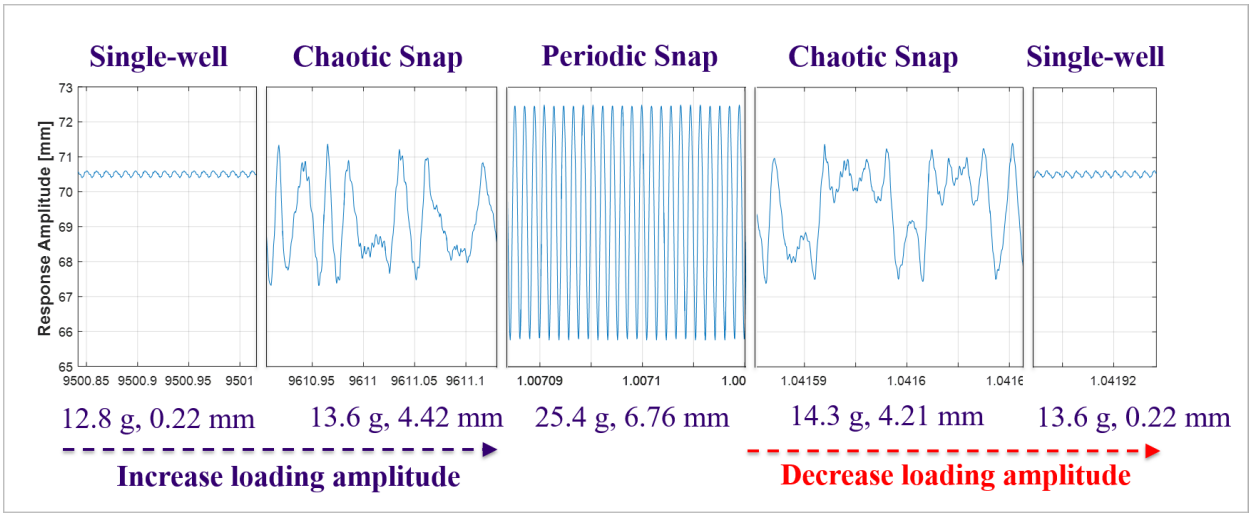

Figure 3.13: Dynamic response under 105 Hz harmonic loading.

chaotic snap-through to periodic snap-through occurs, the loading amplitude was set to continuously decrease. At 14.3 g, the plate stopped showing the periodic snap-through and began to demonstrate chaotic snap-through again. This is another threshold (named *the threshold 2*) where a transition from periodic snap-through to chaotic snap-through occurs. Thus, the transition at the threshold 2 happens in the reverse direction compared to the transition at the threshold 1. Once these thresholds are found at the other frequencies in the frequency domain and are marked in the harmonic forcing parameter space (loading amplitude vs. loading frequency), the thresholds 1 and 2 create boundaries on the space and are named periodic snap-through boundaries as shown in Figure 3.15. The data points on the space were connected to visualize the boundary clear. The boundary connecting the thresholds 1 (named *Periodic snap starts*) where periodic snap-through starts generally appear higher than the boundary connecting the thresholds 2 (named *Periodic snap stops*) where periodic snap-through stops under decreasing load. As the loading amplitude was further decreased, the chaotic snap-through stopped and the midpoint of the plate settled into a single-well response at 13.6 g. Based on these data, the snap-through boundaries at the 105 Hz loading frequency are illustrated in Figure 3.14.

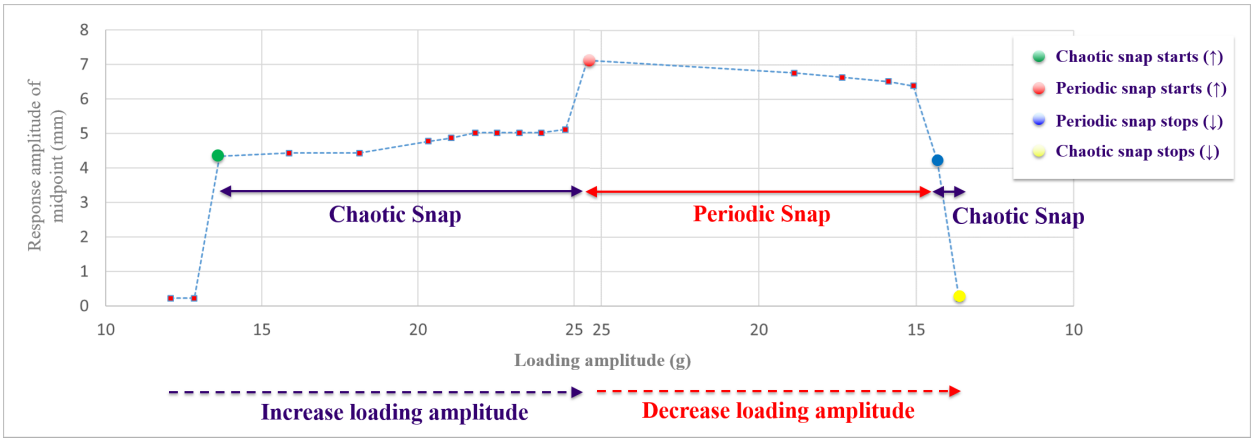

Figure 3.14: Snap-through boundaries under 105 Hz harmonic loading: (↑) indicates the boundaries found while increasing the loading amplitude while (↓) indicates the ones observed while decreasing the amplitude.

The aforementioned process was repeated at frequencies from 30 to 110 Hz to find snap-through boundaries in the harmonic forcing parameter space as shown in Figure 3.15. As discussed previously, the boundaries encountered while increasing the loading amplitude are located higher than are the boundaries found while decreasing the loading amplitude. Consequently, coexisting responses [3, 5, 6, 7, 42] exist between these boundaries. This phenomenon is not unanticipated since the dynamic response of the post-buckled specimen is nonlinear. As seen in Figure 3.15, the chaotic and periodic snap-through responses exist together between the red and green boundaries (Periodic snap starts (↑) and Chaotic snap starts (↑), respectively). In addition, the periodic snap-through and single-well responses exist together between the green and blue boundaries (Chaotic snap starts (↑) and Periodic snap stops (↓), respectively).

Although the data collected by the single-point laser could not provide enough information to compare the experimental data with the modeling results, this exploratory investigation of the snap-through boundaries shown in Figure 3.15 provided a useful experimental analysis on the characterization of snap-through boundaries and relevant nonlinear behaviors.

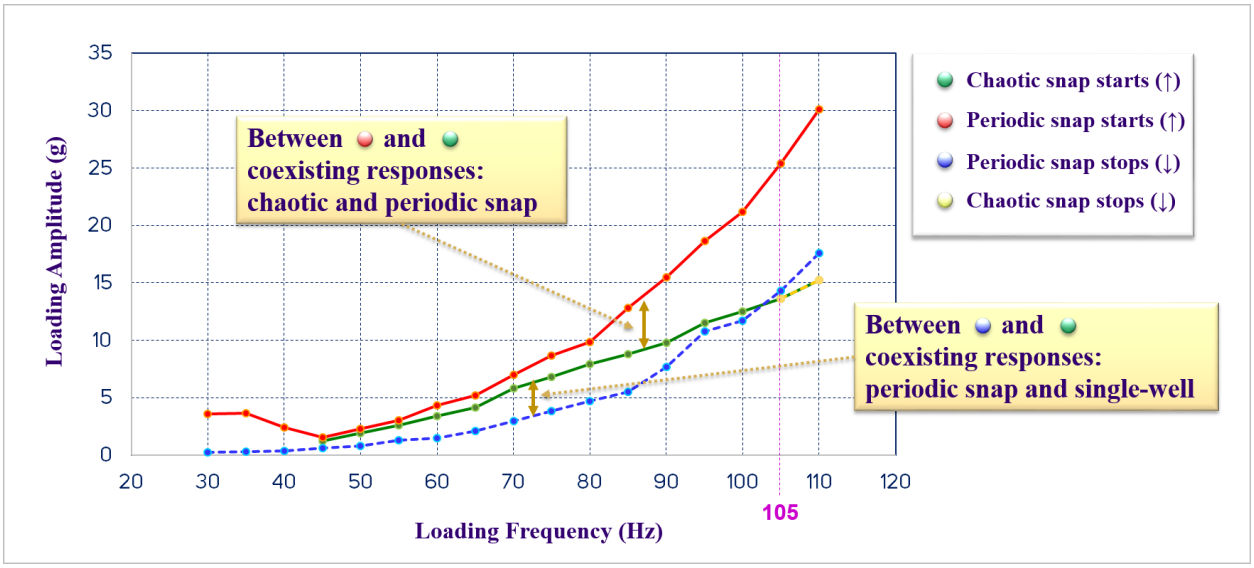

Figure 3.15: Snap-through boundaries in the harmonic forcing parameter space (loading amplitude vs. loading frequency): (↑) indicates the boundaries found while increasing the loading amplitude while (↓) indicates the ones observed while decreasing the amplitude.

3.5 Full-field measurement of the nonlinear dynamic response of a post-buckled plate

To further develop the exploratory investigation of the snap-through boundaries, full-field measurement of the nonlinear dynamic response of a post-buckled plate specimen was conducted at AFRL. The experimental data were collected using the vibrometer and the two DIC cameras. The vibrometer data obtained from frequency-sweep tests were used to find snap-through boundaries of the specimen. The DIC technique was used to find the buckled shape of the specimen and to collect the full-field measurement data of the dynamic response of the specimen. Since the technique is data-intensive as previously discussed, to find the snap-through boundaries of the post-buckled specimen, frequency-sweep tests were performed using the vibrometer instead of using the DIC cameras. Some of the vibrometer measurements were compared to the corresponding DIC data to verify the validity of the vibrometer data. These experiments are outlined in Table 3.9.

Table 3.9: An outline of the experiments at AFRL

Experiment	Equipment	Purpose	Range
Static	DIC cameras	Buckled shape	N/A
Force-dwell	DIC cameras and vibrometer	Comparison between the two data sets	5 g-85 Hz, 7 g-75 Hz, 4 g-180 Hz
Frequency-sweep	Vibrometer	Investigation of snap-through boundary	Frequency: 50 to 180 Hz Amplitude: 2 to 7 g

3.5.1 Experimental setup

The AFRL plate (Figure 3.2b and Table 3.2) was used as a specimen in this experiment. The specimen was clamped along $x = 0$ and $x = a$ and was free along $y = 0$ and $y = b$ as shown in Figure 3.16b, in which a and b are specified in Table 3.2. Thus, the boundary conditions were CCFF. As shown in Figure 3.16a, the clamp was mounted onto the shake table of the electrodynamic shaker. The shaker applied a harmonic loading to the clamp and the loading was inertially applied to the specimen in the clamp. The corresponding dynamic response of the specimen was captured by the two DIC cameras (Figure 3.17a) and by the vibrometer (Figure 3.17b).

3.5.2 Digital image correlation (DIC) technique

In this experiment, the DIC technique, particularly the binocular stereovision technique, was used to obtain the full-field measurement of the dynamic response of the plate specimen. Binocular stereovision is a technique for reconstructing a 3-D structure from two (or more) different viewpoints of a binocular stereovision sensor which is made up of two cameras positioned in such a way that their field of view intersects [43]. As shown in Figure 3.16a, the two DIC cameras traced the random speckle pattern on the surface of the plate with a

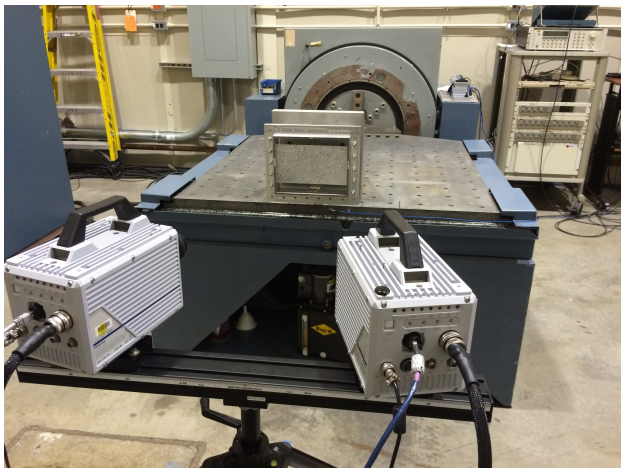

(a) DIC experimental setup.

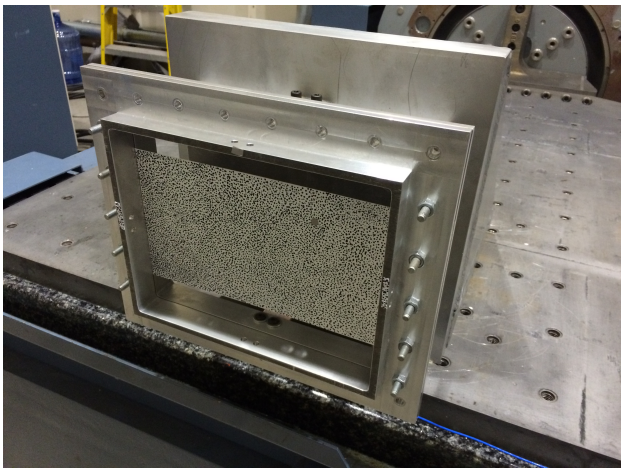

(b) Boundary conditions of the specimen: CCFF.

Figure 3.16: Experimental setup for the full-field measurement.

(a) DIC camera: Photron FASTCAM SA5.

(b) Double-point vibrometer laser: Polytec OFV 512.

Figure 3.17: Equipment employed for the full-field measurement.

2,000 Hz sampling frequency. Figure 3.18 shows the digital images taken by the two cameras. The two left and right pairs demonstrate the fields of views of the left and right cameras, respectively. The bottom two screens show the 99 sampling points on the specimen during the forced vibration of the specimen. The 95 points were placed on the plate while the other

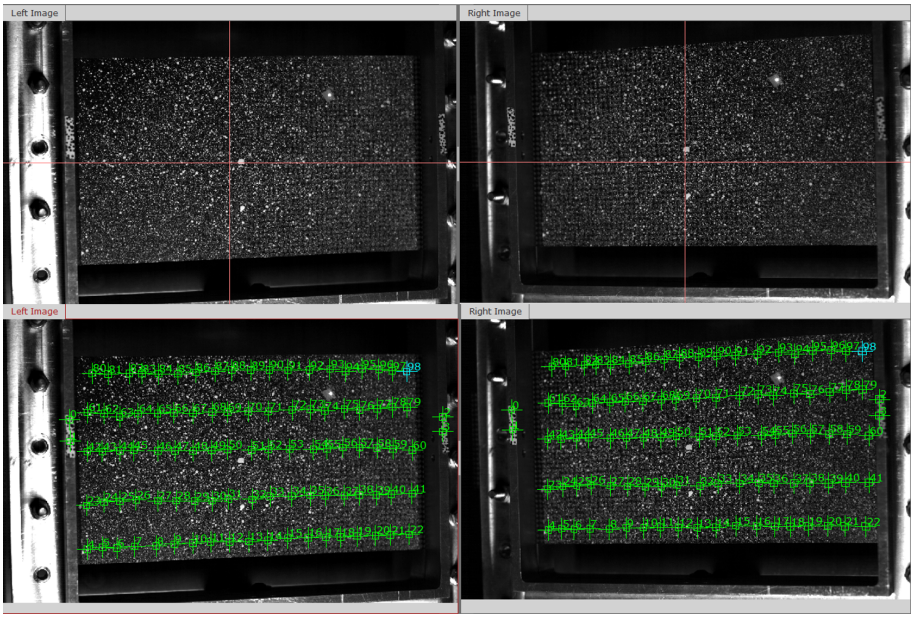

Figure 3.18: DIC controller screens: digital images of the specimen taken by the two cameras (top pictures) and sampling points on the images (bottom pictures).

4 points traced the movement of the clamp to measure the displacement of the specimen relative to the base (i.e. the clamp) motion.

3.5.3 Experimental data: the DIC technique

The DIC technique was used to measure the buckled shape and to collect data from the dynamic experiments with three types of loading: dwelling at (a) 5 g-85 Hz, (b) 7 g-75 Hz, and (c) 4 g-180 Hz.

Static measurement of the buckled shape

The initially-flat plate was buckled and was clamped as shown in Figure 3.16b. The plate could not be buckled as shown in Figure 3.12 at AFRL. Alternatively, one edge of the plate was clamped first and then the plate was pressed down by a hand. While maintaining the pressure on the plate, the other edge was clamped to the frame. Figure 3.19 shows the

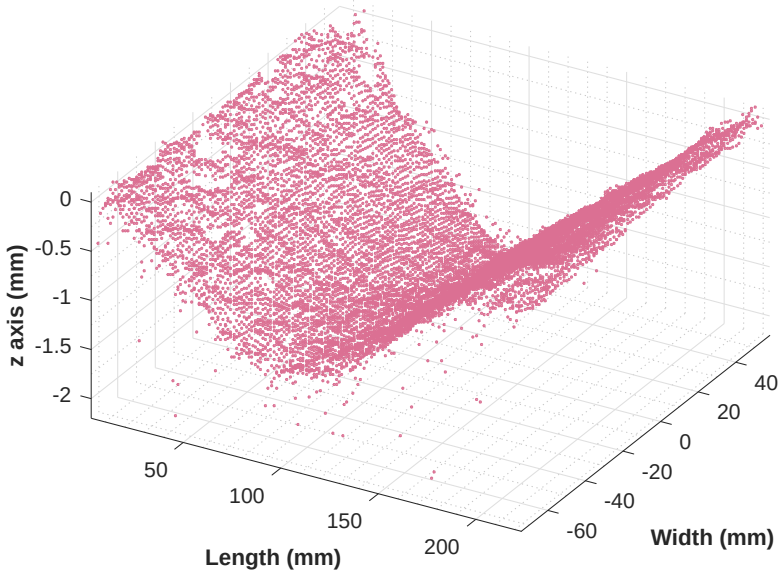

(a) Buckled shape of the specimen reconstructed by the static full-field measurement with 13,475 sampling points.

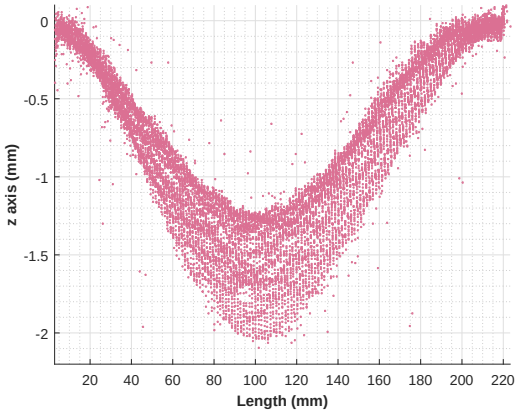

(b) Buckled shape of the specimen along the length.

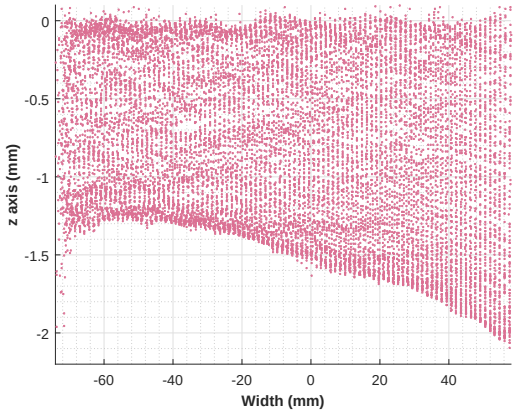

(c) Buckled shape of the specimen along the width.

Figure 3.19: Static full-field measurement of the buckled shape of the specimen.

buckled shape of the specimen reconstructed by the static full-field measurement with 13,475 sampling points before the specimen was subjected to harmonic load (at $t = 0$). It can be

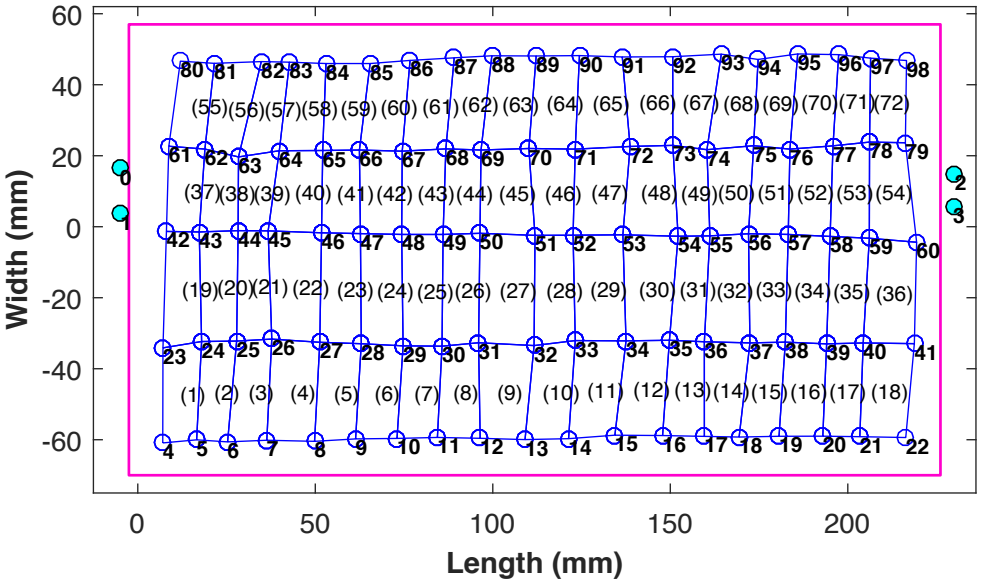

Figure 3.20: Superposition of the specimen plate (pink line), 95 sampling points on the plate (blue empty circles), and 4 sampling points on the clamp (cyan-filled circles) for the dynamic full-field measurement.

observed from Figure 3.19b that the buckled shape was not symmetric along the length and was slightly biased to one side. In addition, Figure 3.19c shows that the buckled depth (i.e., transverse displacement) was not symmetric along the width. The buckled depth at the midspan varied from 1.3 to 2.1 mm. It is suspected that these phenomena occurred due to uneven pressure during clamping. This sloped buckled shape showed interesting behaviors including twisting deformation, which is further discussed in the following sections. Although this complexity made modeling more challenging, considering buckling is hardly expected to occur uniformly in reality, analyzing the experimental data and modeling results of this buckled specimen can be expected to provide more insights into the dynamic response of post-buckled plates.

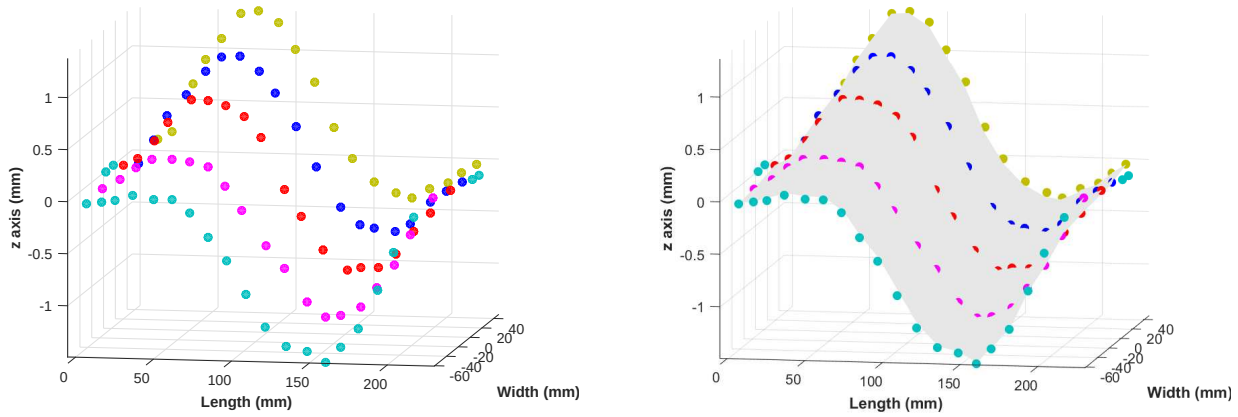

(a) Snapshot of full-field measurement using the 95 sampling points.

(b) Snapshot of deflected shape interpolated from Figure 3.21a.

Figure 3.21: Full-field measurement of the dynamic response of the specimen subjected to harmonic loading.

Full-field measurement of the dynamic response

Since the DIC technique generates a large size of data as discussed earlier, the number of the sampling points used in the static measurement could not be maintained for the dynamic test. Instead, just 99 points were used to capture the dynamic response as shown in Figure 3.18; however, those points were enough to trace the dynamic deformation of the reconstructed initial shape. The sampling points are superimposed on the plate in Figure 3.20.

Figure 3.21 illustrates the full-field measurement at a snapshot of the dynamic response of the specimen subjected to 5 g-85 Hz harmonic loading. The displacement of the 95 sampling points was added to the corresponding points in the buckled shape and then the deformed shape was reconstructed as shown in Figure 3.21a. The entire deformed shape was reconstructed by interpolating the shape from the positions of the sampling points using MATLAB as shown in Figure 3.21b.

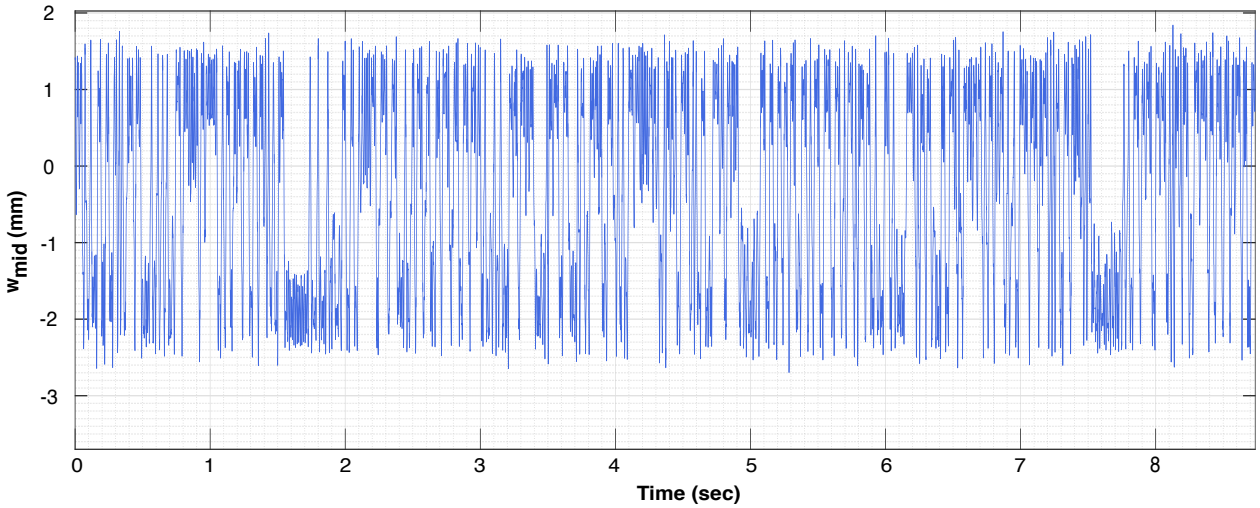

Figure 3.22: Transverse displacement of the midpoint (sampling point number 51 in Figure 3.20) w_{mid} subjected to 5 g-85 Hz harmonic loading.

DIC force-dwell 1: 5 g-85 Hz harmonic loading

The sampling point number 51 in Figure 3.20 whose buckled depth was 1.39 mm was chosen as the (nominal) midpoint of the plate. Figure 3.22 shows the transverse displacement of the midpoint (w_{mid}) over a period of 8.74 seconds when the plate specimen was subjected to 5 g-85 Hz harmonic loading. In the figure, it is observed that the post-buckled plate demonstrated chaotic snap-through under the given loading amplitude and frequency. The midpoint recurrently oscillated around one of its stable equilibria and then snapped into the other stable equilibrium point in a chaotic manner. When it oscillated around a stable equilibrium point (i.e., a single-well response), the peak-to-peak response was approximately 0.8 mm; however, the peak-to-peak displacement of the frequent snap-through events was around 4.1 mm, a significant increase compared to the single-well response.

Figure 3.23 shows the state-space of the midpoint. The sampling frequency, 2,000 Hz, was too low to capture smooth curves in the state-space. Considering the state-space and

the transverse displacement in Figure 3.22, the separatrix[2] of w_{mid} appears to be located (nominally) at between w_{mid} = -1.0 and -0.5 mm. Since the separatrix is higher-dimensional, the discussion on the separatrix in this section relates to w_{mid}. As an approximation, it was also observed that the upper equilibrium point ($w_{\text{mid}} \simeq$ 1.0 mm) was closer to the neutral point (w_{mid} = 0 mm) than was the lower equilibrium point ($w_{\text{mid}} \simeq$ -2.0 mm). The neutral point was located on the flat plane (w = 0 mm) connecting the two fixed boundaries.

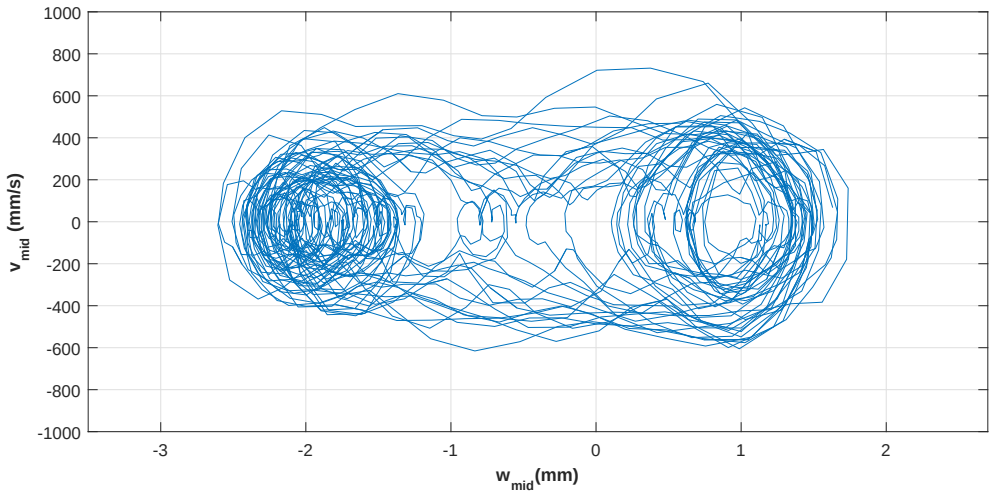

Figure 3.23: State-space of the midpoint subjected to 5 g-85 Hz harmonic loading.

Figure 3.24 demonstrates a part of the chaotic transverse response in Figure 3.22 over a period of 0.45 seconds and the snapshots of the corresponding interpolated deflected shapes of the plate specimen. At the peak (1), the plate in Figure 3.24b oscillated around the upper equilibrium point and the first mode dominated the response. When the plate approached the assumed separatrix ($w_{\text{mid}} \simeq$ -0.5 to -1.0 mm) at (2), the dominance of the second mode was observed (Figure 3.24c). The plate could not snap into the lower equilibrium point at (2) and continued to oscillate around the upper equilibrium point. At (3) (Figure 3.24d), the

[2]Following the description of Strogatz in [20], the basin boundary (a stable manifold) which separates the two basins of attraction shown in Figure 1.3b is traditionally called a separatrix. Thompson defined in [44] that in an n-dimensional state space, an invariant manifold of dimension *n-1* that separates regions of the state space is named a separatrix.

plate showed a larger displacement at the peak than the displacement at (1) and snapped into the lower equilibrium point to arrive at the other peak at (5) (Figure 3.24f). When the plate passed the assumed separatrix of w_{mid} at (4) (Figure 3.24e), it was observed that the response amplitude was significantly smaller than the amplitude at (2) and that the plate looked almost flat. This is an interesting phenomenon since plates experience large amplitude compressive loads when they pass their neutral points ($w_{\text{mid}} = 0$) and thus the plates typically demonstrate the dominance of higher modes as shown at (2) and at (7) (Figure 3.24h) since these modes have lower potential energy. Thus, the deflected shape observed at (4) is abnormal and is not expected to frequently happen; however, when it occurs, the plate experiences a larger compressive load than the load at (2) and (7). At (6) (Figure 3.24g), the plate had a response amplitude slightly smaller than the response amplitude at (3). Although the plate moved into the immediate vicinity of the assumed separatrix at (7), it could not snap into the other equilibrium point and continued to oscillate the upper equilibrium point.

DIC force-dwell 2: 7 g-75 Hz harmonic loading

Figure 3.25 shows w_{mid} over a period of 8.72 seconds when the plate specimen was subjected to 7 g-75 Hz harmonic loading. In the figure, it is observed that the post-buckled plate demonstrated nearly periodic snap-through. The midpoint continuously snapped between the two stable equilibria in a periodic manner. When the midpoint demonstrated a chaotic snap-through in Figure 3.22, the peak-to-peak displacement was approximately 4.1 mm; however, the peak-to-peak displacement during the periodic snap-through was around 5.2 mm. In addition to the increased peak-to-peak displacement, the nearly periodic snap-through case showed a significantly higher number of snap-through events than did the chaotic snap-through case in the same time window for a slightly lower frequency.

Figure 3.26 shows the state-space of the midpoint subjected to 7 g-75 Hz harmonic loading. Considering the plots of the state-space and of the transverse response in Figure

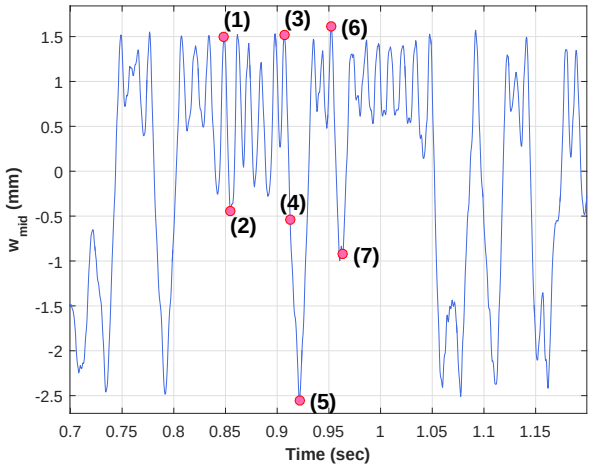

(a) Part of the chaotic response in Figure 3.22.

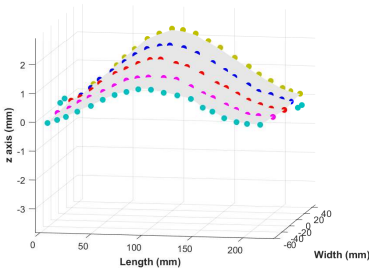

(b) Deflected shape at (1).

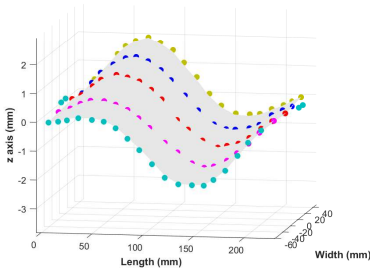

(c) Deflected shape at (2).

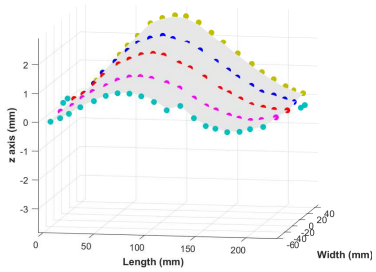

(d) Deflected shape at (3).

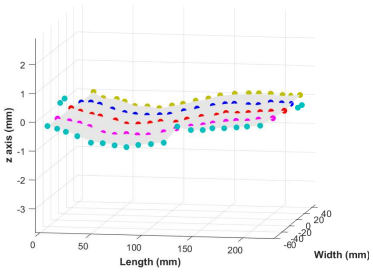

(e) Deflected shape at (4).

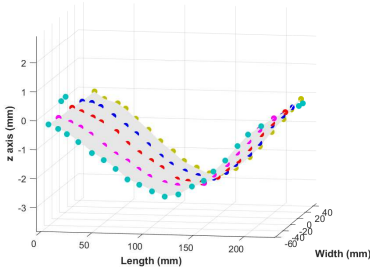

(f) Deflected shape at (5).

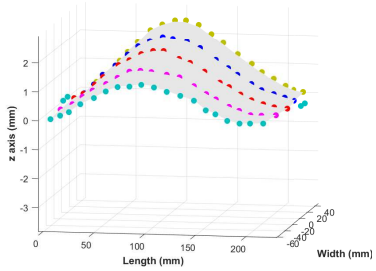

(g) Deflected shape at (6).

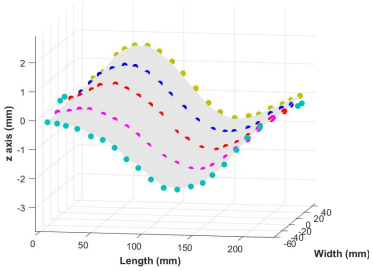

(h) Deflected shape at (7).

Figure 3.24: Chaotic dynamic response of the plate subjected to 5 g-85 Hz harmonic loading and snapshots of corresponding interpolated deflected shapes.

3.25, the separatrix of w_{mid} appears to be located at the same point found from Figure 3.23, which is positioned at between w_{mid} = -0.5 and -1.0 mm. Since the midpoint traveled in a

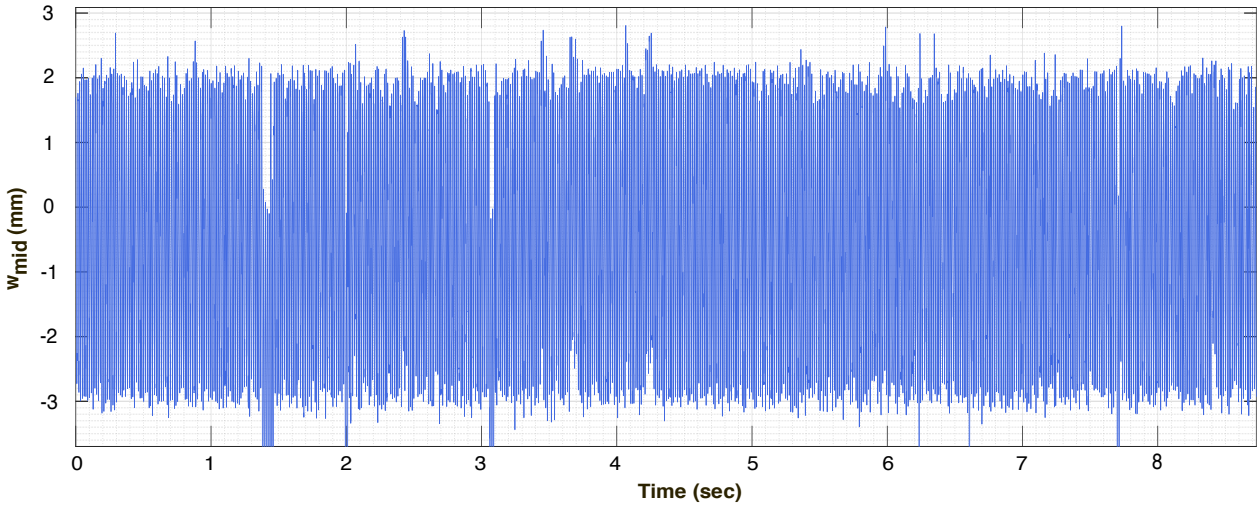

Figure 3.25: w_{mid} subjected to 7 g-75 Hz harmonic loading.

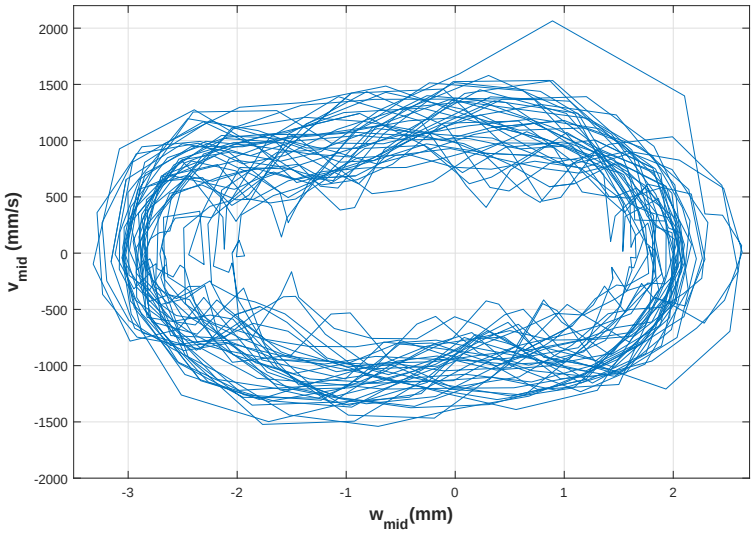

Figure 3.26: State-space of the midpoint subjected to 7 g-75 Hz harmonic loading.

periodic manner above the two basins of attraction of the two stable equilibria, the midpoint draws a hollow elliptical shape in the state-space as shown in Figure 3.26.

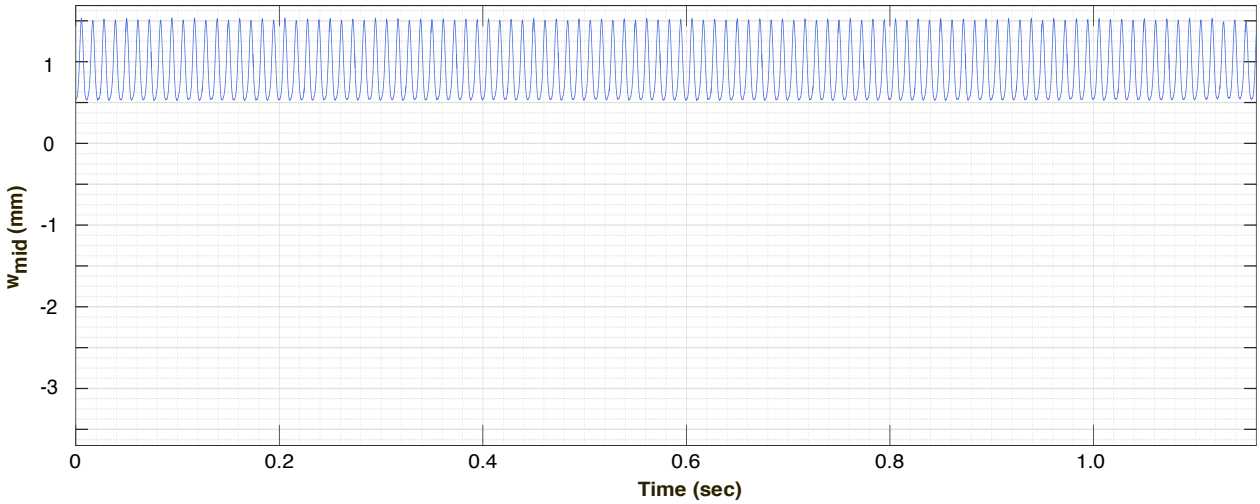

Figure 3.27: w_{mid} subjected to 4 g-180 Hz harmonic loading.

DIC force-dwell 3: 4 g-180 Hz harmonic loading

Figure 3.27 shows w_{mid} over a period of 1.16 seconds when the plate specimen was subjected to 4 g-180 Hz harmonic loading. In the figure, it is observed that the post-buckled plate demonstrated a single-well response under that loading. The midpoint settled down in the upper stable equilibrium and oscillated around the equilibrium point in a periodic manner. The peak-to-peak response was approximately 1.0 mm, which is considerably smaller than the chaotic and periodic snap-through cases.

Figure 3.28 shows the state-space of the midpoint. Considering the state-space and the transverse displacement in Figure 3.27, the upper stable equilibrium point of the midpoint appears to be located at around $w_{\text{mid}} = 1.0$ mm. Since the midpoint showed periodic single-well response and traveled inside one of the two basins of attraction, the midpoint draws a hollow ellipse in the state-space and does not cross the separatrix to move to the other basin as shown in Figure 3.26. It also exhibited asymmetric response, which is a characteristic of single-well response in bi-stable systems.

It was observed from the video taken during the force-dwell experiment and from the re-constructed full-field response of the plate under the aforementioned three types of harmonic

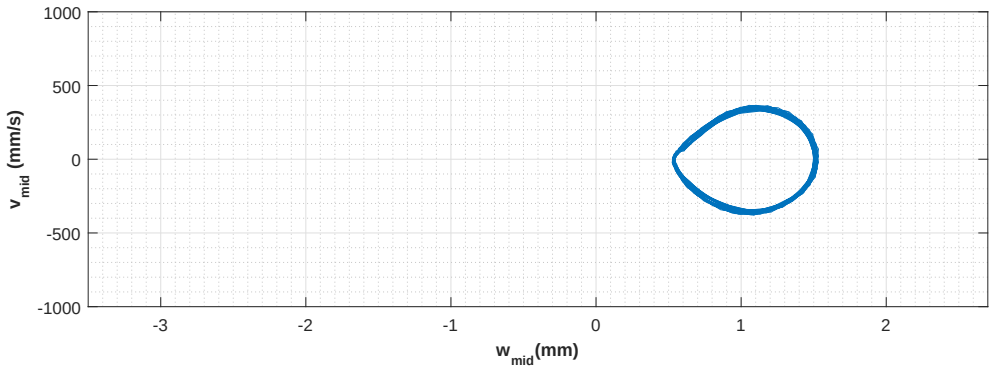

Figure 3.28: State-space of the midpoint subjected to 4 g-180 Hz harmonic loading.

loading that twisting deformation concurred with the flexural vibration due to the sloped buckled shape along the depth.

3.5.4 Experimental data: the vibrometer

As shown in Figure 3.29a, one of the two vibrometer lasers traced the vibration of the plate while the other laser detected the movement of the bottom of the clamp (i.e., the base) to measure the displacement of the plate relative to the clamp. The vibrometer laser sampling point was aimed between DIC sampling points number 74 and 94 and is indicated as a red circle on Figure 3.29b. Since the vibrometer inherently does not provide full-field measurement, the force-dwell experimental data which were collected by using both the DIC cameras and the vibrometer at the same time were compared to verify the validity of the vibrometer measurement.

Methodology of vibrometer data analysis

In this section, the methodology of the vibrometer data analysis is explained by taking an example of the frequency-sweep experiment with 5 g forcing amplitude. The forcing frequencies against time were extracted from Figure 3.30 as shown in Figure 3.31a. Based

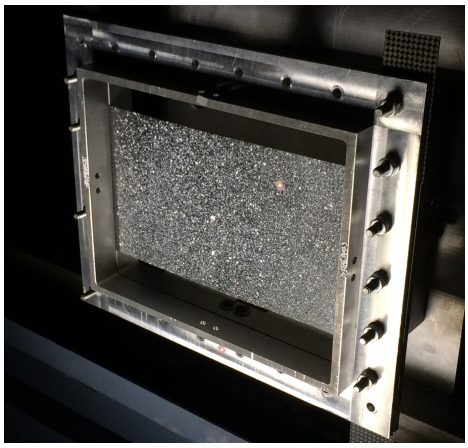

(a) One vibrometer sampling point (a red dot) on the AFRL plate. Another point (a red dot) on the bottom of the clamp.

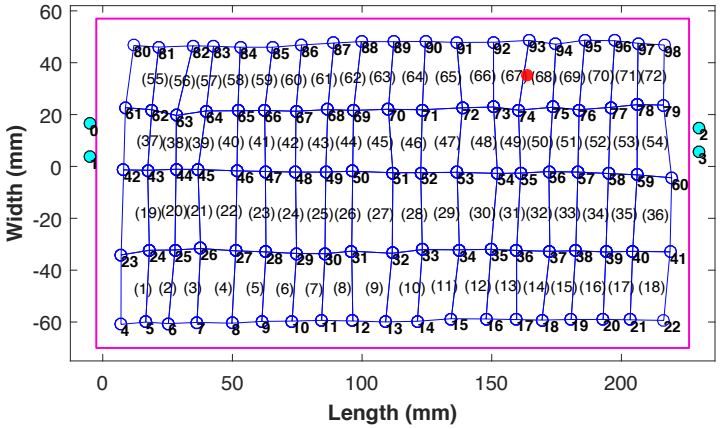

(b) vibrometer sampling point (red circle) between the DIC sampling points number 74 and 93.

Figure 3.29: Vibrometer sampling point on the specimen surface.

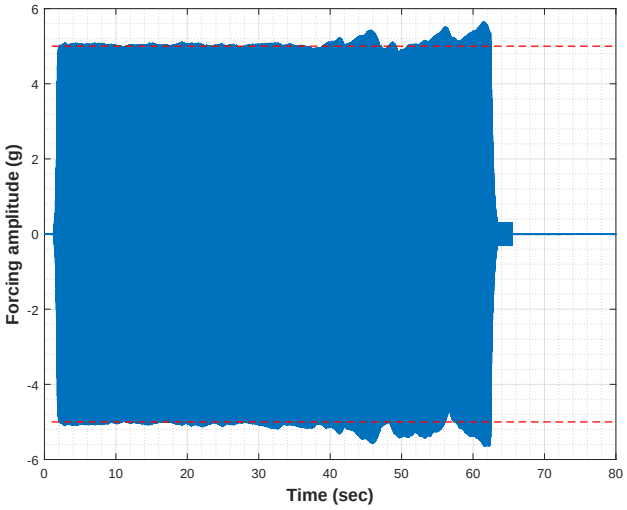

Figure 3.30: Harmonic forcing amplitude 5 g vs. time.

on the stepped plots (red lines), the upper and lower bounds (blue lines) were evaluated. Using these bounds, the plots were filtered as shown in Figure 3.31b.

Figure 3.32b illustrates the displacement obtained through cumulative trapezoidal numerical integration of the measured velocity seen in Figure 3.32a. In the displacement plot,

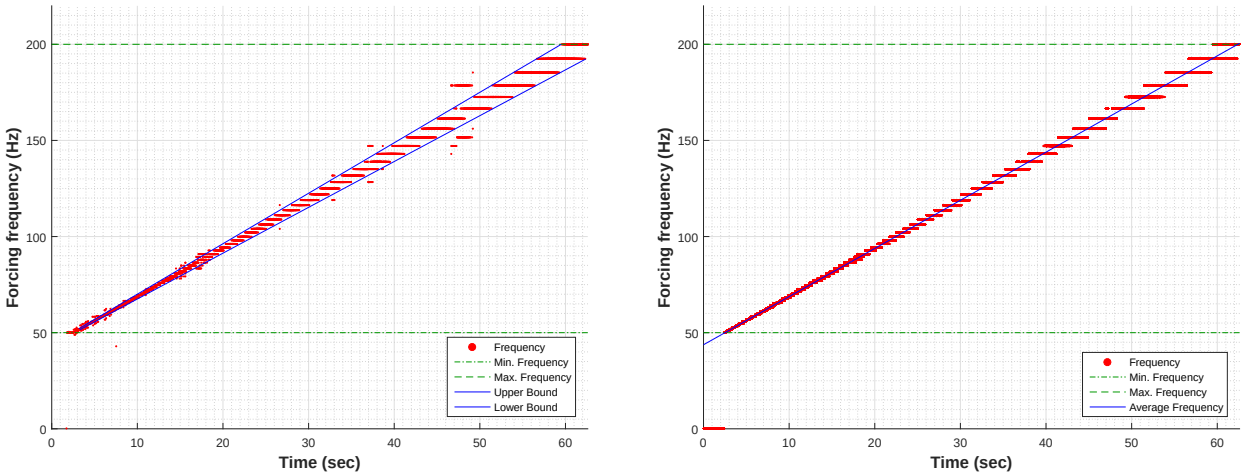

(a) Extracted forcing frequency vs. time.

(b) Filtered forcing frequency vs. time.

Figure 3.31: Stepped forcing frequencies of the frequency-sweep experiment (5 g).

it was observed that the datum was continuously shifted due a DC bias[3] in the vibrometer during the measurement and thus the true datum could not be specified. Therefore, the displacement values indicated in Figure 3.32b are less dependable; however, the peak-to-peak displacement can be used as an important indication of occurrence of snap-through [3].

For a convenient visualization, the drift due to the DC bias was removed as shown in Figure 3.33 by continuously subtracting a windowed average of peak-to-peak displacements from the displacements within the window. According to the reconstructed buckled shape (Figure 3.19), the buckled depth of the vibrometer sampling point was 0.793 mm. In Figure 3.33, the buckled depth is demarcated as red dotted lines and the data points exceeding the buckled depth are colored as purple, which means that snap-through likely occurred at those points. Furthermore, the time data in the x-axis of Figure 3.32b was replaced by the frequency data obtained from the average frequency values marked on a blue solid line in Figure 3.31b for the intuitive analysis of the plot. However, when the snap-through

[3]The presence of a DC current or voltage component in an AC system is called DC bias (or DC offset), which may cause a steady-state deviation from a sine wave (i.e., waveform distortion) [45]. Thus, DC bias means a non-zero mean value of waveform [46].

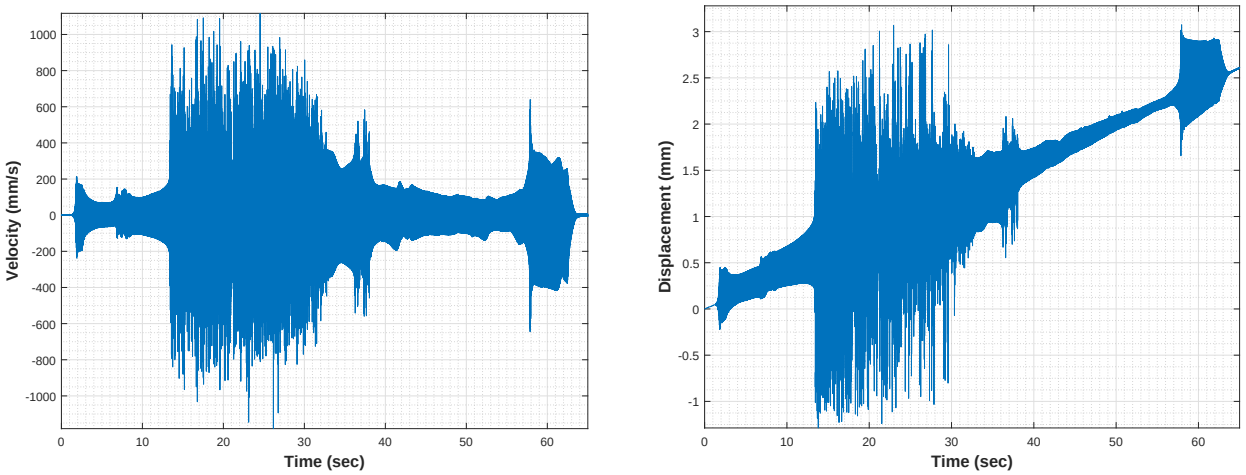

(a) Measured velocity.

(b) Numerically integrated displacement.

Figure 3.32: Measured velocity and integrated displacement of the frequency-sweep experiment (5 g).

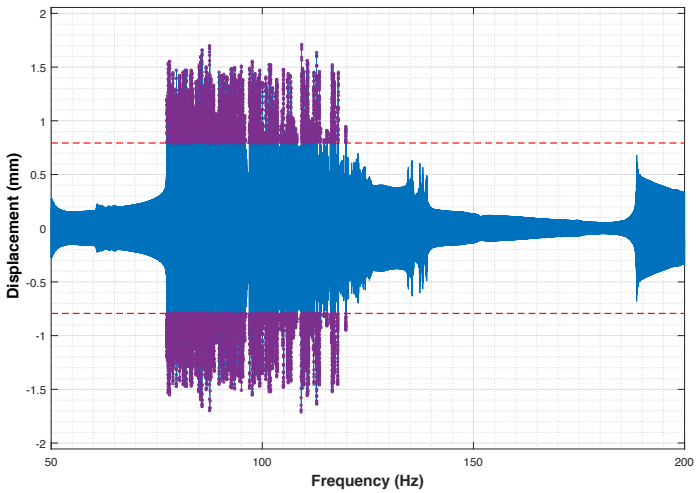

Figure 3.33: Numerically integrated displacement shifted by removing the drift from Figure 3.32b. The buckled depth is demarcated as red dotted lines and the data points exceeding the buckled depth are colored as purple.

boundaries were marked on the harmonic forcing parameter space as shown in Figure 3.34, the actual stepped frequency values were used in lieu of the continuously increasing average frequencies. The other frequency-sweep experimental data collected by the vibrometer are

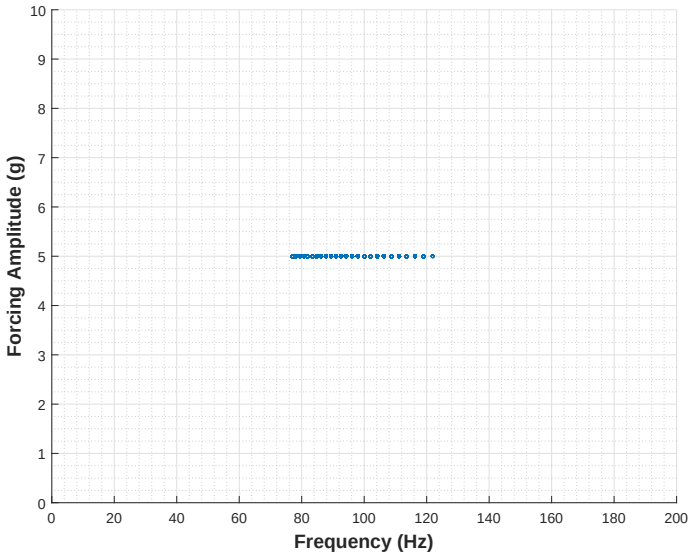

Figure 3.34: Snap-through boundary of 5 g forcing amplitude in the harmonic forcing parameter space.

presented and are compared with the modeling results in Chapter 5.

3.5.5 Experimental data: comparison of the force-dwell data between the DIC technique and the vibrometer

Figure 3.35 illustrates the numerically integrated displacement of the vibrometer sampling point (named *the vib-point*) measured by the vibrometer (w_{vibro}) when the plate was subjected to 5 g-85 Hz harmonic forcing over a period of 60 seconds. The displacement continued out of the plot range at time = 25.5 seconds, which indicates that there were occasions where the displacement of the plate exceeded the measuring range of the vibrometer.

While measuring the dynamic response shown in Figure 3.35 with the vibrometer, the DIC cameras were triggered at time = 0.728 seconds and measured the same response over a period of 8.74 seconds. In case one of the DIC sampling points coincides with the vib-point, the DIC cameras would fail to track the point since interpretation of the speckle pattern around the point would be interrupted by the vibrometer laser aimed at the point. Thus,

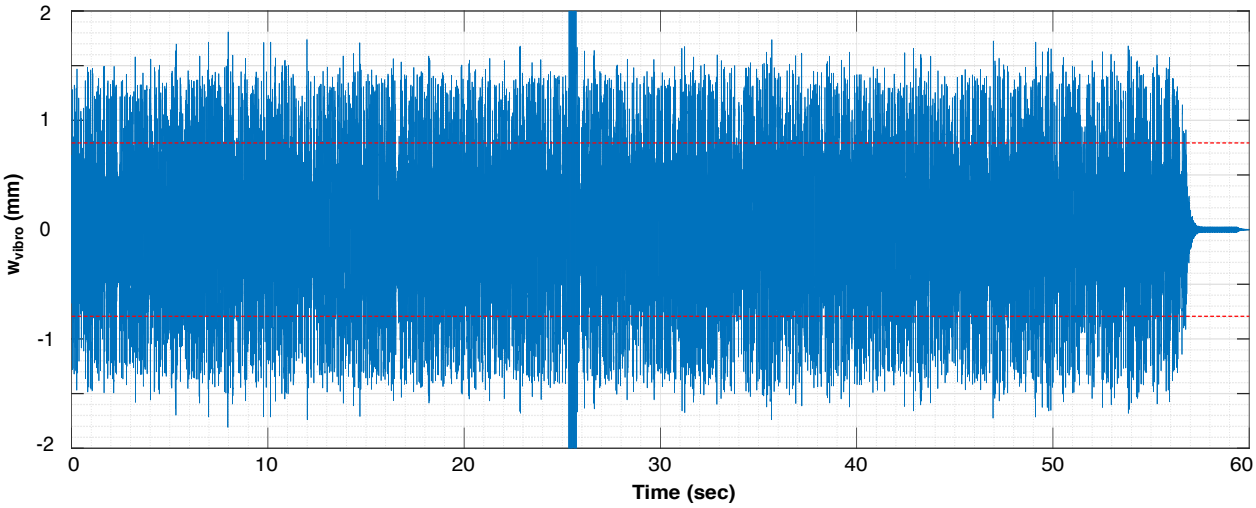

Figure 3.35: Displacement of the vib-point measured by the vibrometer (w_{vibro}) when the plate was subjected to 5 g-85 Hz harmonic forcing. The red dotted lines indicate the buckled depth of the vib-point.

the vib-point was located between the DIC sampling points number 74 and 93 and then the DIC measurement of the vib-point (w_{DIC}) was interpolated using the displacements of those DIC sampling points. The responses observed by both the vibrometer and the DIC cameras at the same time are compared in Figure 3.36. For comparison purposes, time = 0.728 seconds of the vibrometer measurement shown in Figure 3.35 was set as time = 0 second of Figure 3.36.

It is clearly noticeable that the two plots in Figure 3.36 demonstrate the same trend. To be specific, when w_{vibro} exceeded the red dotted line (i.e., the buckled depth of the vib-point) in the top figure, w_{DIC} showed snap-through in the bottom plot. In addition, as shown on the three sections marked by red dotted arrows, the single-well responses also match well. Furthermore, the peak-to-peak displacement of the two plots are almost identical (3.0 mm).

The other two cases shown in Figures 3.37 and 3.38 also exhibit the coincident trends (nearly periodic and single-well, respectively) and identical peak-to-peak displacements (4.0 and 1.0 mm, respectively). Therefore, both data sets were deemed to be precisely synchronized and the numerically integrated displacement of the vibrometer data shifted by

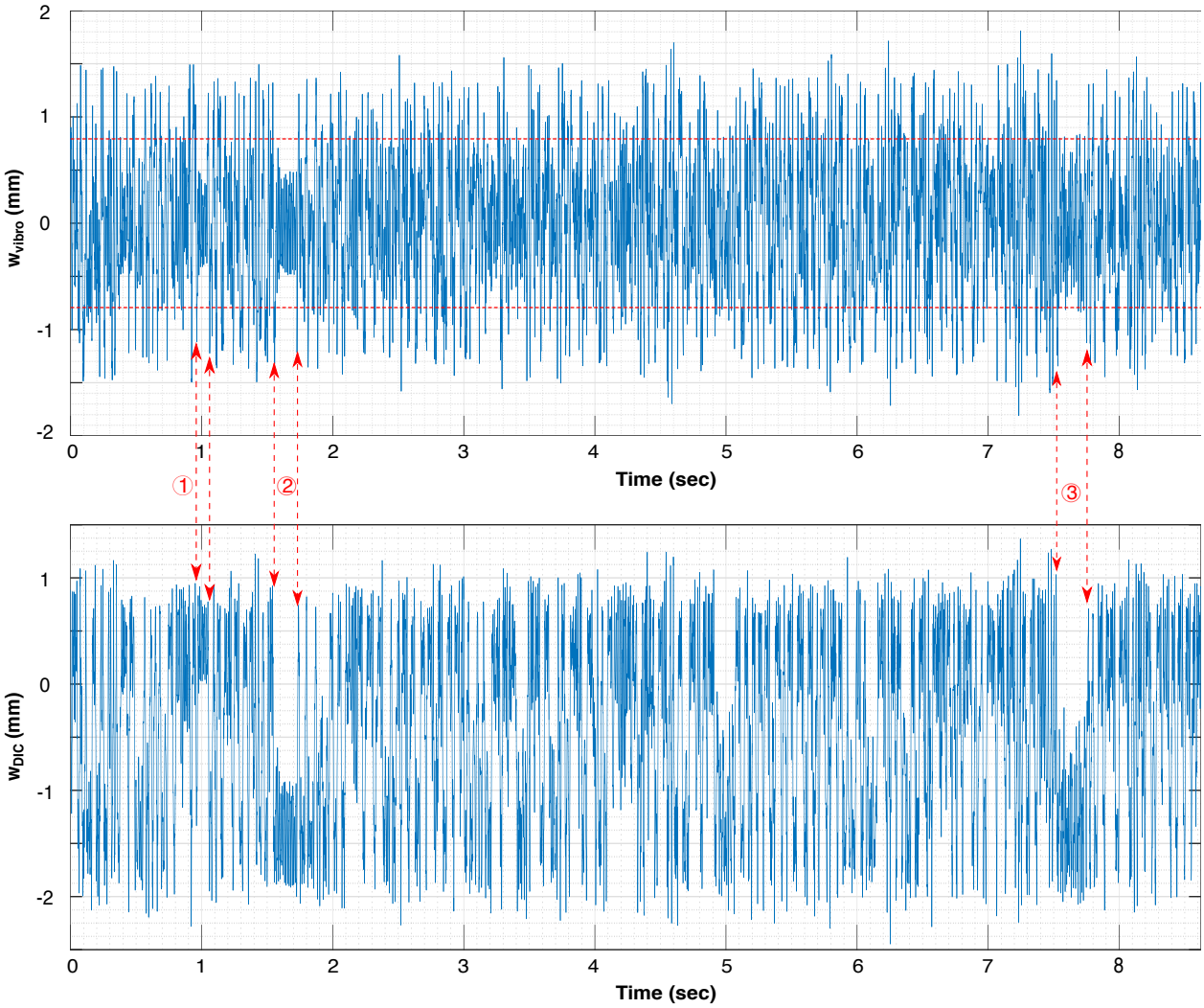

Figure 3.36: Comparison between the data of 5 g-85 Hz harmonic forcing collected by the vibrometer (w_{vibro}) and by the DIC cameras (w_{DIC}) simultaneously. The red dotted lines in the top figure indicate the buckled depth of the vib-point.

removing the drift was validated.

3.6 Summary

In this chapter, the material properties of the specimen were predicted and verified through the tests. In addition, the full-field measurement of the buckled shape of the AFRL plate

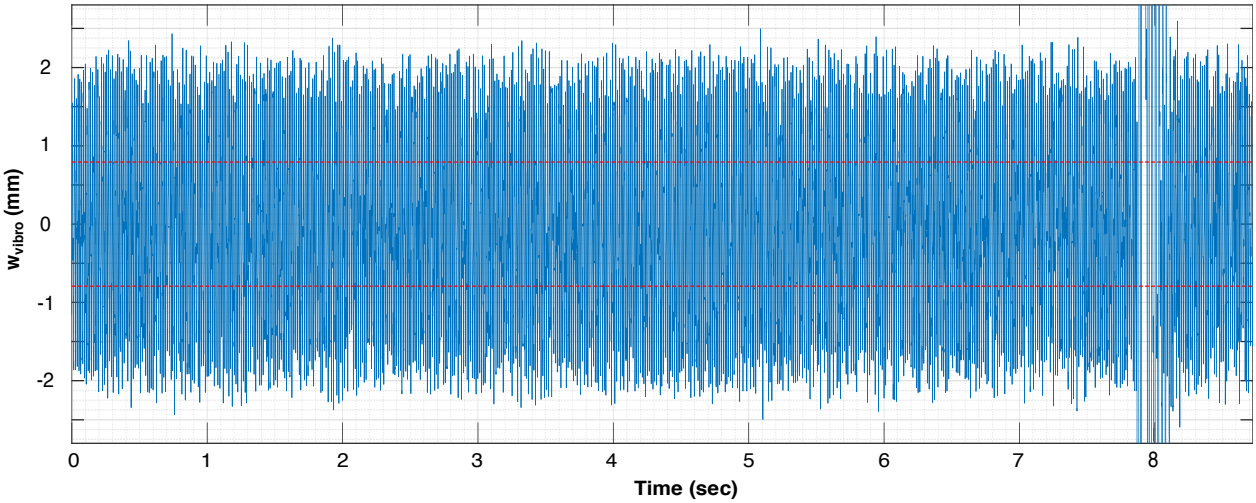

(a) Measurement of the vibrometer, w_{vibro}. The red dotted lines indicate the buckled depth of the vib-point.

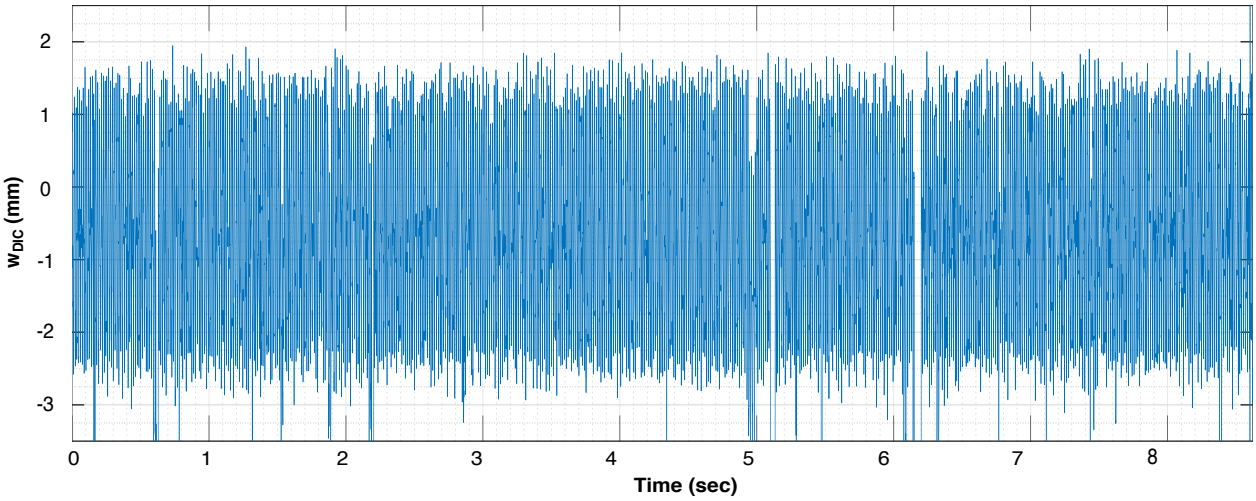

(b) Measurement of the DIC cameras, w_{DIC}.

Figure 3.37: Comparison between the data of 7 g-75 Hz harmonic forcing collected by the vibrometer and by the DIC cameras simultaneously.

was collected by the DIC cameras. This information was used for modeling described in Chapter 4.

The vibrometer data were compared with the corresponding full-field DIC data for verification purposes. The exploratory investigation of the snap-through boundaries of the post-buckled UW plate illustrated the important characteristics of the snap-through bound-

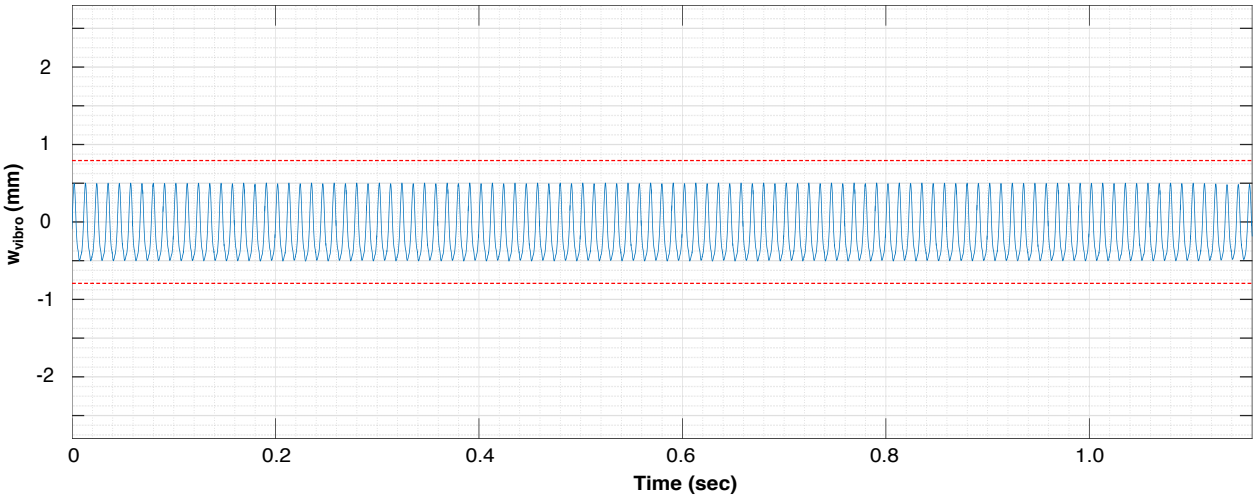

(a) Measurement of the vibrometer, w_{vibro}. The red dotted lines indicate the buckled depth of the vib-point.

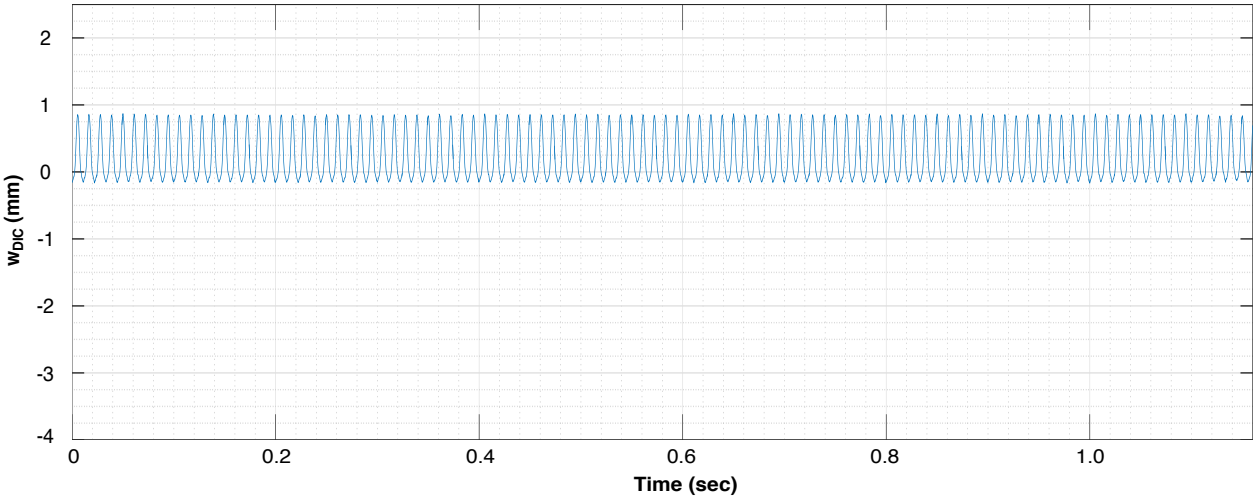

(b) Measurement of the DIC cameras, w_{DIC}.

Figure 3.38: Comparison between the data of 4 g-180 Hz harmonic forcing collected by the vibrometer and by the DIC cameras simultaneously.

aries. To identify the snap-through boundaries of the AFRL plate, the vibrometer data of frequency-sweep tests are presented in Chapter 5.

Chapter 4

MODELING OF SNAP-THROUGH OF POST-BUCKLED THIN LAMINATED COMPOSITE PLATES

4.1 Introduction

In this chapter, the nonlinear FEM developed in Equations (2.70) to (2.92) is solved for the static and dynamic analyses of the post-buckled specimens used for the experiments introduced in the previous chapter. Since CLPT is based on Kirchhoff plate theory, the C^1 continuity of the transverse degrees of freedom Δ_j^e in Equation (2.69) needs to be satisfied. Thus, high-precision cubic Hermite elements were used to develop the FEM.

For the static analysis, an arc-length method and a branch-switching technique were applied to the FEM to find the equilibrium paths of post-buckled plates. In addition, for the dynamic analysis, the Newmark-beta method was applied to the FEM in conjunction with the Newton-Raphson method to find solutions within each time step.

Both conforming and nonconforming elements (i.e., rectangular and quadrilateral elements, respectively) were investigated in this work. The characteristics of those elements are described in the following sections. The static and dynamic analyses using conforming elements were an exploratory investigation since these elements inherently cannot capture the irregularly-buckled shape of the AFRL plate and the material properties used for those analyses are not identical with the material properties evaluated in Chapter 2. The dynamic analysis based on nonconforming elements used the same material properties as described in Chapter 2 and was compared to the dynamic response of the post-buckled AFRL plate. The

analysis types and associated models described in this chapter are outlined in Table 4.1.

4.2 High-precision cubic Hermite elements

There are two kinds of plate bending elements to satisfy the C^1 continuity of the transverse degrees of freedom $\{\Delta_j^e\}$ in Equation (2.69): (a) conforming elements, and (b) nonconforming elements [25]. In this section, the high-precision cubic Hermite elements for both conforming and nonconforming elements are introduced using the description of Dhatt in [36].

4.2.1 Conforming elements: rectangular four-node element with C^1 continuity

The conforming rectangular element with four nodes was developed by Bogner, et al. [47] and is illustrated in Figure 4.1. The nodal degrees of freedom of this type of an element are u_i^e, v_i^e, and $\{\Delta_i^e\}$ for $i = 1, 2, 3, 4$. The in-plane degrees of freedom (u_i^e, v_i^e) are not affected by transformation between real and reference elements while the transverse degrees of freedom of a real element $(\{\Delta_i^e\})$ are transformed into the transverse degrees of freedom of a reference element $(\{\Delta_i^e\}_\xi)$ and vice versa. The nodal variables $\{\Delta_i^e\}$ and $\{\Delta_i^e\}_\xi$ are defined in Figure 4.1.

Table 4.1: An outline of the modeling

Analysis type	Element	Purpose	Method
Static	Conforming	Exploratory investigation	Arc-length, branch-switching, Newton-Raphson
Dynamic	Conforming	Exploratory Investigation	Newmark-beta, Newton-Raphson
Dynamic	Nonconforming	Comparison with the AFRL experimental data	Newmark-beta, Newton-Raphson

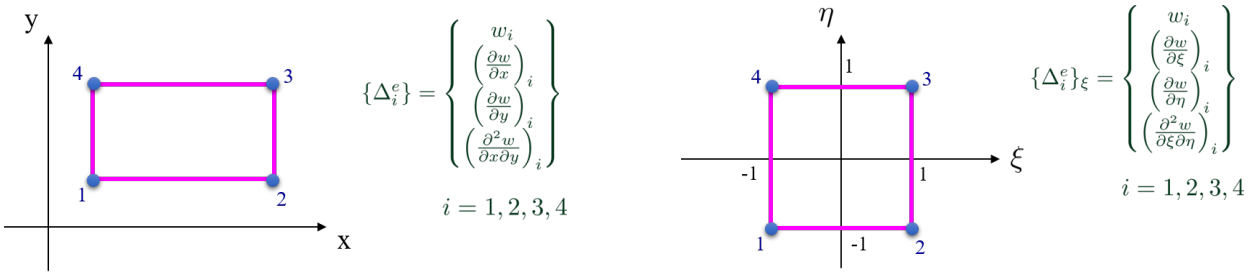

(a) Real element and transverse nodal variables $\{\Delta_i^e\}$.

(b) Reference element and transverse nodal variables $\{\Delta_i^e\}_\xi$.

Figure 4.1: Conforming elements and transverse nodal variables.

Conforming elements satisfy the interelement continuity of these nodal variables [25]. For u_0, v_0, and w_0 in Equation (2.69), linear Largrange interpolation functions were used for ψ_j^e in u_0 and v_0 while cubic Hermite interpolation functions were used for φ_j^e in w_0. Hermite interpolation functions for conforming elements are described in Table 4.2 and Equation (4.1). Equation (4.1) also applies to $N_i(\eta)$ by substituting ξ with η. Hermite interpolation functions w_1 and $(\partial w/\partial \xi)_1$ are visualized in Figure 4.2.

$$
\begin{aligned}
N_1(\xi) &= \frac{1}{4}(1-\xi)^2(2+\xi), \\
N_2(\xi) &= \frac{1}{4}(1-\xi^2)(1-\xi), \\
N_3(\xi) &= \frac{1}{4}(1+\xi)^2(2-\xi), \\
N_4(\xi) &= \frac{1}{4}(-1+\xi^2)(1+\xi).
\end{aligned}
\tag{4.1}
$$

The transformation between $\{\Delta_i^e\}$ and $\{\Delta_i^e\}_\xi$ is described in Equation (4.2).

$$
\{\Delta_i^e\}_\xi = \left[T_i\right] \{\Delta_i^e\}, \tag{4.2}
$$

in which

$$\left[T_i\right] = \begin{bmatrix} 1 & 0 & 0 & 0 \\ 0 & \frac{a}{2} & 0 & 0 \\ 0 & 0 & \frac{b}{2} & 0 \\ 0 & 0 & 0 & \frac{ab}{4} \end{bmatrix}. \tag{4.3}$$

In case an FEM is solved in the isoparametric space, the nodal variables $\{\Delta_i^e\}$ in Figure 4.1 should be the final variables obtained from the model [36]. The transformation of transverse nodal variables should be considered as a separate process from the transformation between

Table 4.2: Hermite interpolation functions for conforming elements

	w_i	$(\partial w/\partial\xi)_i$	$(\partial w/\partial\eta)_i$	$(\partial^2 w/\partial\xi\partial\eta)_i$
Node 1	$N_1(\xi)\cdot N_1(\eta)$	$N_2(\xi)\cdot N_1(\eta)$	$N_1(\xi)\cdot N_2(\eta)$	$N_2(\xi)\cdot N_2(\eta)$
Node 2	$N_3(\xi)\cdot N_1(\eta)$	$N_4(\xi)\cdot N_1(\eta)$	$N_3(\xi)\cdot N_2(\eta)$	$N_4(\xi)\cdot N_2(\eta)$
Node 3	$N_3(\xi)\cdot N_3(\eta)$	$N_4(\xi)\cdot N_3(\eta)$	$N_3(\xi)\cdot N_4(\eta)$	$N_4(\xi)\cdot N_4(\eta)$
Node 4	$N_1(\xi)\cdot N_3(\eta)$	$N_2(\xi)\cdot N_3(\eta)$	$N_1(\xi)\cdot N_4(\eta)$	$N_2(\xi)\cdot N_4(\eta)$

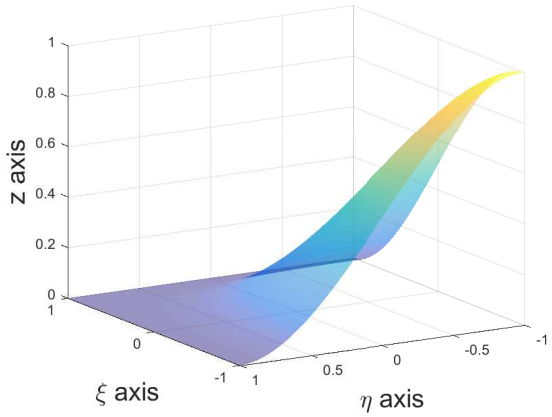

(a) Hermite interpolation function for w_1.

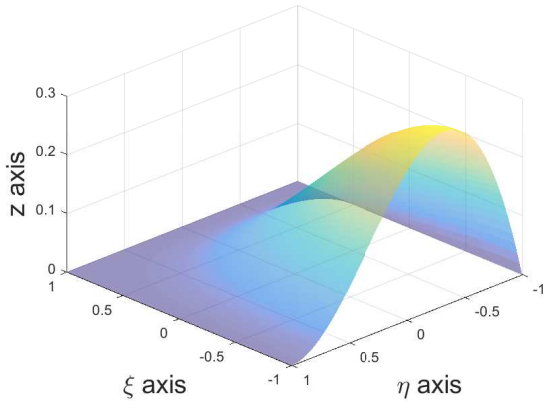

(b) Hermite interpolation function for $(\partial w/\partial\xi)_1$.

Figure 4.2: Visualization of Hermite interpolation functions at node 1 ($(\xi,\eta) = (-1,-1)$).

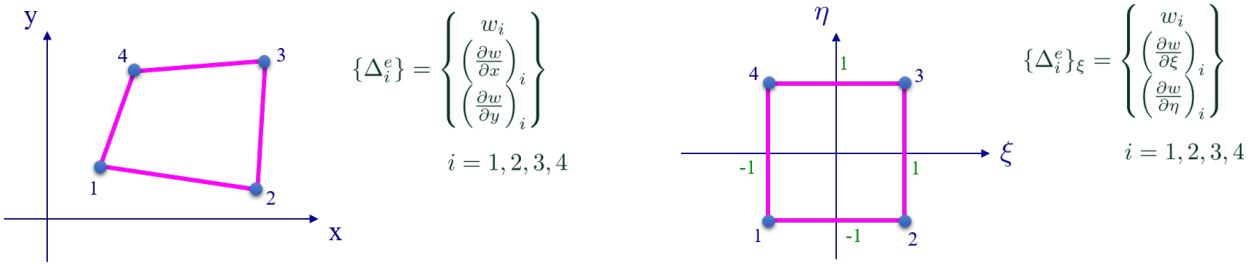

(a) Real element and transverse nodal variables $\{\Delta_i^e\}$.

(b) Reference element and transverse nodal variables $\{\Delta_i^e\}_\xi$.

Figure 4.3: Nonconforming elements and transverse nodal variables.

$w_0(x, y)$ and $w_0(\xi, \eta)$ and between corresponding spatial derivatives. In case of using the Newton-Raphson method to solve a nonlinear FEM within each time step, nodal variables obtained from the previous step affect the stiffness matrix of the current step. Therefore, if the transformation process is omitted, the stiffness matrix can be incorrect.

4.2.2 Nonconforming element: quadrilateral four-node element with semi-C^1 continuity

The nonconforming quadrilateral element with four nodes was developed by Melosh in [48], and Zienkiewicz and Cheung in [49] and is illustrated in Figure 4.3. Same as the characteristics of conforming elements, the transverse degrees of freedom of a real nonconforming element ($\{\Delta_i^e\}$) are transformed into the transverse degrees of freedom of a reference element ($\{\Delta_i^e\}_\xi$) and vice versa; however, $\left(\frac{\partial^2 w}{\partial x \partial y}\right)_i$ and $\left(\frac{\partial^2 w}{\partial \xi \partial \eta}\right)_i$ of nonconforming elements are omitted from $\{\Delta_i^e\}$ and $\{\Delta_i^e\}_\xi$ respectively as defined in Figure 4.3.

Since $\frac{\partial w}{\partial \xi}_i$ and $\frac{\partial w}{\partial \eta}_i$ are continuous at each node, nonconforming elements satisfy the interelement continuity of w_i and $\frac{\partial w_i}{\partial n}$; however, the continuity of $\frac{\partial w_i}{\partial s}$ is not satisfied. The directions n and s are defined in Figure 2.3. The Hermite interpolation functions for a nonconforming element are described in Table 4.3 and Equation 4.4.

Table 4.3: Hermite interpolation functions for nonconforming elements

	w_i	$\partial w_i/\partial x$	$\partial w_i/\partial y$
Node 1	$\frac{1}{8}(\alpha-\xi-\eta)$	$\frac{1}{8}a(1-\xi^2)$	$\frac{1}{8}a(1-\eta^2)$
Node 2	$\frac{1}{8}b(\alpha+\xi-\eta)$	$-\frac{1}{8}b(1-\xi^2)$	$\frac{1}{8}b(1-\eta^2)$
Node 3	$\frac{1}{8}c(\alpha+\xi+\eta)$	$-\frac{1}{8}c(1-\xi^2)$	$-\frac{1}{8}c(1-\eta^2)$
Node 4	$\frac{1}{8}d(\alpha-\xi+\eta)$	$\frac{1}{8}d(1-\xi^2)$	$-\frac{1}{8}d(1-\eta^2)$

$$
\begin{aligned}
a &= (1-\xi)(1-\eta),\\
b &= (1+\xi)(1-\eta),\\
c &= (1+\xi)(1+\eta),\\
d &= (1-\xi)(1+\eta),\\
\alpha &= 2-\xi^2-\eta^2.
\end{aligned}
\tag{4.4}
$$

The transformation between $\{\Delta_i^e\}$ and $\{\Delta_i^e\}_\xi$ for nonconforming elements is described in Equation (4.5).

$$
\{\Delta_i^e\}_\xi = \Big[T_i\Big]\,\{\Delta_i^e\}, \tag{4.5}
$$

in which

$$
\Big[T_i\Big] = \begin{bmatrix} 1 & 0 & 0 \\ 0 & & \\ 0 & \Big[J(\xi_i)\Big] & \end{bmatrix}, \tag{4.6}
$$

in which $[J(\xi_i)]$ is defined in Equation (2.93).

The advantage of using nonconforming elements is that these elements can be applied to

any quadrilateral real elements while the application of conforming elements is confined to only rectangular real elements because obtaining a transformation matrix shown in Equation (4.3) is complicated for non-rectangular shapes.

4.3 Solution methods for the nonlinear static analysis of post-buckled plates

4.3.1 Method 1: Arc-length method

To investigate the equilibrium paths of post-buckled plates, an arc-length method was used. Various arc-length methods [50, 51, 52, 53, 54, 55] were tried to compare their performance. In this work, the linearized arc-length method of Schweizerhof and Wriggers in [56] was selected since the method is simple but yields a good performance. In this section, the linearized arc-length method is presented by following the Crisfield's description in [57].

An equilibrium equation can be expressed as

$$\mathbf{g}(\mathbf{p}, \lambda) = \mathbf{q}_i(\mathbf{p}) - \lambda \mathbf{q}_{ef} = 0, \tag{4.7}$$

in which $\mathbf{q}_i$ are internal forces, $\mathbf{p}$ represents displacements, $\mathbf{q}_{ef}$ is a fixed external loading vector, and the scalar λ is a load-level parameter.

An arc-length is defined by

$$s = \int ds, \tag{4.8}$$

$$ds = \sqrt{d\mathbf{p}^T d\mathbf{p} + d\lambda^2 \psi^2 \mathbf{q}_{ef}^T \mathbf{q}_{ef}}, \tag{4.9}$$

in which ψ is the scaling parameter. The differential form in Equation (4.9) can be replaced with the incremental form in Equation (4.10).

$$a = (\Delta\mathbf{p}^T \Delta\mathbf{p} + \Delta\lambda^2 \psi^2 \mathbf{q}_{ef}^T \mathbf{q}_{ef}) - \Delta l^2 = 0, \tag{4.10}$$

in which the radius Δl is an approximation to the incremental arc length.

The Newton-Raphson method can be described as a truncated Taylor series using Equations (4.7) and (4.10):

$$\mathbf{g}_n = \mathbf{g}_0 + \frac{\partial \mathbf{g}}{\partial \mathbf{p}}\delta\mathbf{p} + \frac{\partial \mathbf{g}}{\partial \lambda}\delta\lambda = \mathbf{g}_0 + \mathbf{K}_t\delta\mathbf{p} - \mathbf{q}_{ef}\delta\lambda = 0, \tag{4.11}$$

$$a_n = a_0 + 2\Delta\mathbf{p}^T\delta\mathbf{p} + 2\Delta\lambda\delta\lambda\psi^2\mathbf{q}_{ef}^T\mathbf{q}_{ef} = 0, \tag{4.12}$$

in which the subscripts n and o denote new and old, respectively. Using Equation (4.12),

$$-a_0/2 = \Delta\mathbf{p}^T\delta\mathbf{p} + \delta\lambda(\Delta\lambda\psi^2\mathbf{q}_{ef}^T\mathbf{q}_{ef}), \tag{4.13}$$

in which a_0 is the old value of the arc-length mismatch. Using Equation (4.11),

$$\delta\mathbf{p} = -\mathbf{K}_t^{-1}\mathbf{g}_0 + \delta\lambda\mathbf{K}_t^{-1}\mathbf{q}_{ef} = \delta\bar{\mathbf{p}} + \delta\lambda\delta\mathbf{p}_t, \tag{4.14}$$

in which $\mathbf{K}_t$ is a tangent stiffness matrix. Substituting $\delta\mathbf{p}$ in Equation (4.14) with $\delta\mathbf{p}$ in Equation (4.12), the corrector of the linearized arc-length method was obtained as shown in Equation (4.15).

$$\delta\lambda(\Delta\mathbf{p}_0, \Delta\lambda_0) = \frac{-a_0/2 - \Delta\mathbf{p}^T\delta\bar{\mathbf{p}}}{\Delta\mathbf{p}_0^T\delta\mathbf{p}_t + \Delta\lambda_0\psi^2\mathbf{q}_{ef}^T\mathbf{q}_{ef}}. \tag{4.15}$$

This corrector was used with a forward-Euler tangential predictor shown in Equation (4.16).

$$\Delta\mathbf{p}_p = \Delta\lambda_p\mathbf{K}_{t0}^{-1}\mathbf{q}_{ef} = \Delta\lambda_p\delta\mathbf{p}_t, \tag{4.16}$$

in which $\mathbf{K}_{t0}$ is the tangent stiffness matrix at the beginning of the increment. Substituting

Equation (4.16) into Equation (4.10) with $\psi = 0$,

$$\delta\lambda_p = \pm\frac{\Delta l}{\sqrt{\delta\mathbf{p}_t^T\delta\mathbf{p}_t}}. \tag{4.17}$$

4.3.2 Method 2: Singular points and branch switching

Identifying singular points and switching branches at these singular points are required to follow the equilibrium paths of post-buckled plates. The semi-direct approach for computation of singular points which Shi and Crisfield introduced in [58] was employed in this work.

In this method, the signs of current stiffness parameters and test functions are used to identify singular points, which is called the bracketing process. The current stiffness parameter C_s is defined as

$$\begin{aligned} k &= \frac{\Delta\mathbf{q}^T\Delta\mathbf{p}}{\Delta\mathbf{p}^T\Delta\mathbf{p}} = \frac{\mathbf{q}_{ef}^T\delta\mathbf{P}_t}{\delta\mathbf{p}_t^T\delta\mathbf{p}_t}, \\ C_s &= \frac{k}{k_0}, \end{aligned} \tag{4.18}$$

in which k is estimated at the current step while k_0 is the initial value. The test function τ can be chosen from one of the following:

- $\tau = \det(\mathbf{K}_t)$,
- $\tau =$ min. pivot from $\mathbf{K}_t$,
- $\tau =$ product of min. pivot and max. pivot from $\mathbf{K}_t$,
- $\tau =$ min. eigenvalue of $\mathbf{K}_t$.

In this work, the minimum eigenvalue of $\mathbf{K}_t$ was chosen as the test function. When both signs of C_s and τ change, it is likely that a limit point has been passed. In case only τ switches its

sign with no change in the sign of C_s, it is likely that a bifurcation point has been passed. The successful bracketing process largely depends on how accurately the first point for the process was found. Thus, in case a relatively large radius of arc-length is applied, there is a high possibility of encountering the first point away from the real singular point.

After identifying the singular points, the simple branch-switching technique that Crisfield described in [59] was employed at bifurcation points. Using this method, the predictor ($\Delta \mathbf{p}_p$) at these points is defined in Equation (4.19).

$$\Delta \mathbf{p}_p = \Delta l \mathbf{z}, \quad \Delta \lambda_p = 0 \tag{4.19}$$

in which z is the lowest eigenmode corresponding to the lowest eigenvalue of $\mathbf{K}_t$ evaluated at bifurcation points.

4.4 Nonlinear static analysis of post-buckled plates: conforming elements

In this section, the nonlinear FEM (Equations (2.70) to (2.92)) was solved using conforming elements to characterize the equilibrium paths of post-buckled plates. As discussed earlier, this analysis is exploratory because

- conforming elements employed in this analysis cannot model the nonuniform buckled depth observed from the reconstructed buckled shape of the AFRL plate, and

- the geometrical and material properties of the specimen used in this analysis are not identical to the ones of the AFRL plate (Table 3.4).

The specimen used in this exploratory analysis was named *the modeling plate*. The geometrical and material properties of the modeling plate and of the AFRL plate are compared in Table 4.4.

Table 4.4: Comparison between the modeling plate and the AFRL plate

	Property	Modeling plate	AFRL plate
Geometry	a (mm)	228.6	228.6
	b (mm)	127	127
	h (mm)	0.63	0.72
Material	$\bar{E}_{xx}$ (GPa)	72.8	75.9
	$\bar{E}_{yy}$ (GPa)	72.8	75.9
	$\bar{G}_{xy}$ (GPa)	5.2	3.96
	$\bar{\nu}_{xy}$	0.3	0.037

4.4.1 Static analysis 1: axial buckling equilibrium path of the initially-flat modeling plate

For the nonlinear static analysis of post-buckled plates, the nonlinear FEM developed in Chapter 2 was simulated using MATLAB with the Hermite interpolation functions for conforming elements described in Table 4.2 and in Equation (4.1). Since conforming elements were employed, the modeling plate was meshed using rectangular elements. The mesh consisted of 231 nodes and 200 elements as shown in Figure 4.4.

The static equilibrium path of the initially-flat modeling plate was analyzed by applying axial loading distributed along the edge of the plate, which corresponds to the nodes number 221 to 231 shown in Figure 4.4. To maintain a straight fixed boundary condition along the edge while the loading was applied, a constraint that the displacements of the nodes along the edge in the length direction (i.e., x-axis direction) were identical was set. The equilibrium path is illustrated in Figure 4.5. In the equilibrium path, the loading parameter $\lambda = 1$ corresponds to the axial load for the first buckling mode, 695.5 N/m. It was observed that the plate buckled slightly above $\lambda = 1$ due to the constraint.

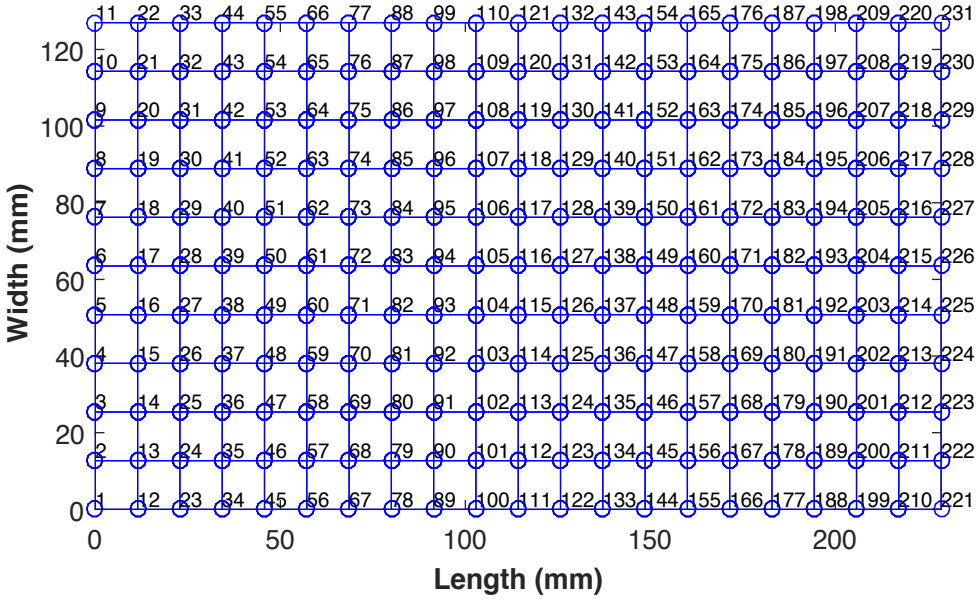

Figure 4.4: FEM mesh for the modeling plate with 231 nodes and 200 rectangular elements.

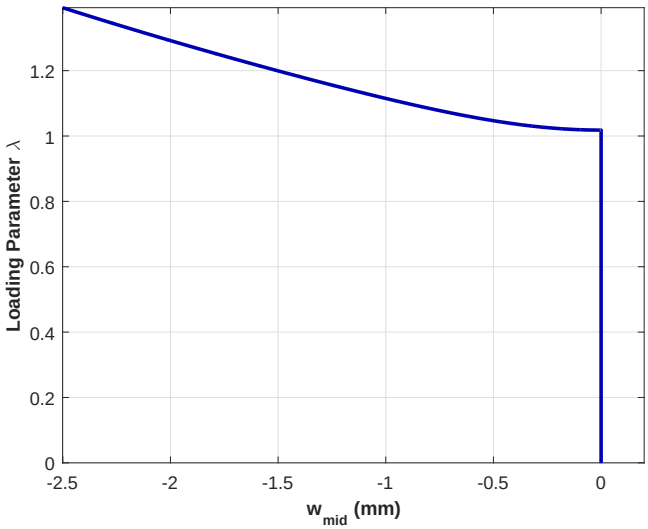

Figure 4.5: Equilibrium path of the initially-flat modeling plate under distributed axial loading. $\lambda = 1$ corresponds to the axial load for the first buckling mode, 695.5 N/m.

4.4.2 Static analysis 2: snap-through equilibrium path of the post-buckled modeling plate

As observed in Figure 3.19, the buckled depth of the AFRL plate along the middle of the length varied from 1.3 to 2.1 mm. Considering the variance of the buckled depth, two different cases were analyzed: two plates with 1 mm- and 2 mm-buckled at the midpoint, respectively. The post-buckled plates were generated using the data obtained from the plot illustrated in Figure 4.5. To find equilibrium paths of the two plates, a point load was applied to the midpoint in the direction of the positive z-axis. The equilibrium paths were analyzed using the linearized arc-length method, the semi-direct approach for the computation of singular points, and the simple branch-switching technique. The static analysis results of the two cases are illustrated in Figures 4.6 and 4.7, and are summarized in Table 4.5. In those plots, w_{mid} is the transverse displacement of the midpoint of the plate, which corresponds to the node number 116 illustrated in Figure 4.1, and P is a concentrated load applied to the midpoint. The 3-D equilibrium paths shown in Figures 4.6d and 4.7d were created by adding an additional axis $w_{1/4} - w_{3/4}$ to the 2-D equilibrium paths shown in Figures 4.6a and 4.7a. The additional axis shows the difference between the transverse displacements of the one-quarter point ($w_{1/4}$) along the length (the node number 61) and the three-quarter point ($w_{3/4}$) along the length (the node number 171), and indicates the level of asymmetry of deflected shapes.

Figure 4.6 demonstrates the equilibrium path and snapshots of corresponding deflected shapes of the 1 mm-buckled plate case. As shown in Figure 4.6b, the buckled shape at (1) had w_{mid} = -1.0024 mm. As P increased, w_{mid} followed its stable primary equilibrium path with increase in both w_{mid} and P. When w_{mid} passed the point (2), both C_s and τ changed their signs and thus it was observed that w_{mid} passed its first limit point at (2). Passing through the limit point, w_{mid} shifted to its unstable primary equilibrium path and P dropped following that path while w_{mid} increased. When w_{mid} passed the point (3), τ changed its sign while C_s maintained its sign. Thus, it was assumed that w_{mid} passed its first bifurcation point at (3) and the bracketing and branch-switching processes were initiated and consequently,

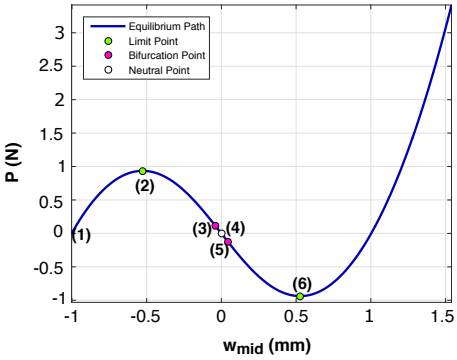

(a) 2-D equilibrium path (w_{mid} vs. P).

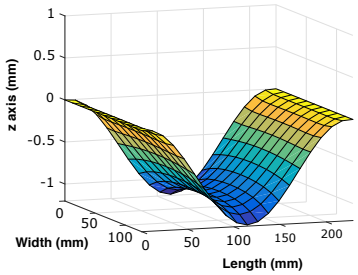

(b) Buckled shape at (1).

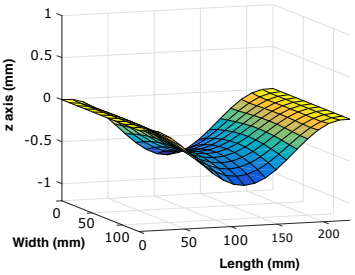

(c) Deflected shape at the first limit point (2).

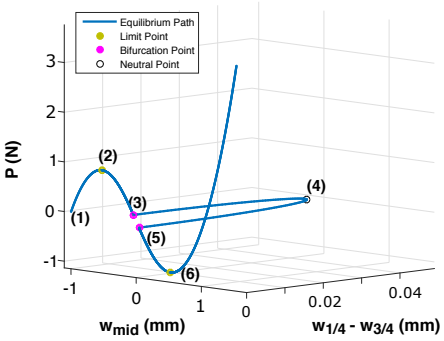

(d) 3-D equilibrium path (w_{mid} vs. $w_{1/4} - w_{3/4}$ vs. P).

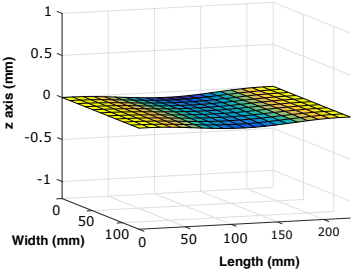

(e) Deflected shape at the first bifurcation point (3).

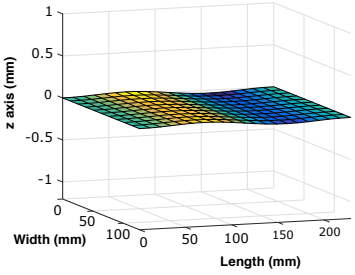

(f) Deflected shape at the neutral point (4).

Figure 4.6: Equilibrium path and snapshots of corresponding deflected shapes of the post-buckled modeling plate (1 mm).

w_{mid} was switched to its unstable secondary path. As observed from the increase in the asymmetry level between the points (3) and (4) shown in Figure 4.6d, the influence of the second mode increased as w_{mid} moved toward the neutral point (4) (i.e., w_{mid}=0), where the asymmetry level reached its maximum value and the second mode dominated the response as shown in Figure 4.6f. After passing the neutral point, the asymmetry level decreased until the level reached zero at the second bifurcation point (5), where w_{mid} returned to its unstable primary path. Passing through its second limit point (6), w_{mid} reverted to its stable primary path and continued following the path. In this case, it was observed that the first bifurcation occurred after w_{mid} passed its first limit point. This phenomenon typically happens for arches

Table 4.5: Limit and bifurcation points of 1 mm- and 2 mm-buckled plates

Point	Values	1 mm-buckled	2 mm-buckled
Initial	w_{mid} (mm)	-1.0024	-2.0023
	P (N)	0	0
First limit	w_{mid} (mm)	-0.5269	N/A
	P (N)	0.9355	N/A
First bifurcation	w_{mid} (mm)	-0.04234	-1.4654
	P (N)	0.1195	4.5183
Neutral	w_{mid} (mm)	0.0005	0.0160
	$w_{1/4} - w_{3/4}(mm)$	0.0445	1.4944
	P (N)	-0.0025	-0.0421
Second bifurcation	w_{mid} (mm)	0.04235	1.4654
	P (N)	-0.1215	-4.5203
Second limit	w_{mid} (mm)	0.5269	N/A
	P (N)	-0.9375	N/A

where w_{mid} is the transverse displacement of the midpoint of the plate (the node number 116) and P is a concentrated load applied to the midpoint.

of intermediate rise.

Figure 4.7 illustrates the equilibrium path and snapshots of corresponding deflected shapes of the 2 mm-buckled plate case. As shown in Figure 4.7b, the buckled shape at (1) had w_{mid} = -2.0023 mm. Same as the previous case, as P increased, w_{mid} followed its stable primary equilibrium path with increase in both w_{mid} and P. When w_{mid} passed the point (2), τ changed its sign while C_s maintained its sign. Thus, it was observed that w_{mid} passed its first bifurcation point at (2) and the bracketing and branch-switching processes were initiated and consequently, w_{mid} was switched to its unstable secondary path. In contrast to the 1 mm-buckled plate case (i.e., an arch of intermediate rise), the 2 mm-buckled plate (i.e., a deep arch) bifurcated before w_{mid} passed its first limit point. Passing through the bifurcation point, w_{mid} shifted to its unstable secondary path and while P decreased

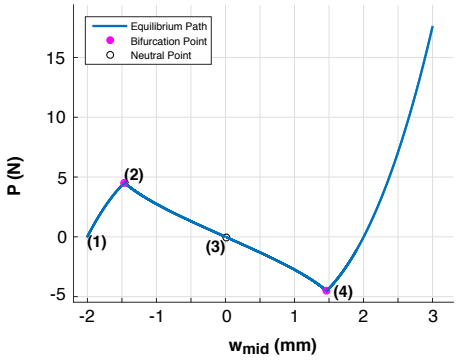

(a) 2-D equilibrium path (w_{mid} vs. P).

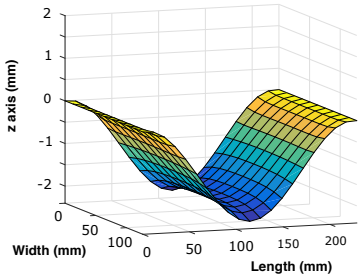

(b) Buckled shape at (1).

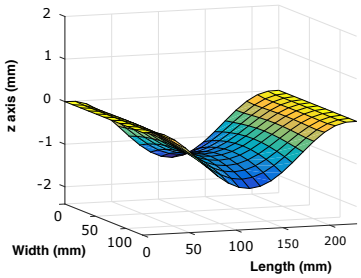

(c) Deflected shape at the first bifurcation point (2).

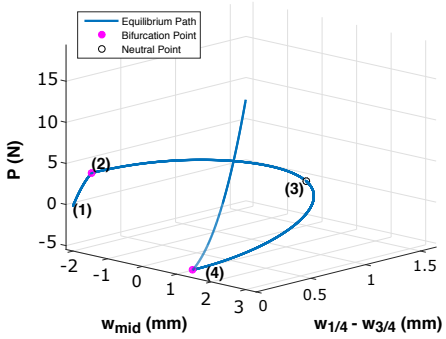

(d) 3-D equilibrium path (w_{mid} vs. $w_{1/4} - w_{3/4}$ vs. P).

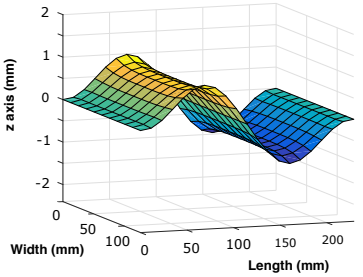

(e) Deflected shape at the neutral point (3).

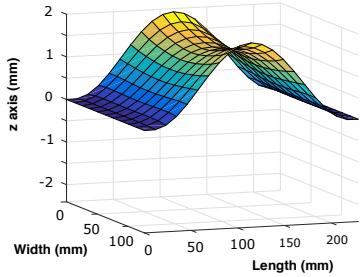

(f) Deflected shape at the second bifurcation point (4).

Figure 4.7: Equilibrium path and snapshots of corresponding deflected shapes of the post-buckled modeling plate (2 mm).

following that path, both w_{mid} and the asymmetry level (i.e., the influence of the second mode) increased. At the neutral point (3), the asymmetry level reached its maximum value and the second mode evidently dominated the response as shown in Figure 4.6e. As shown in Table 4.5, the 2 mm-buckled plate case exhibited significantly higher level of asymmetry and of axial loading at the neutral point than did the 1 mm-buckled plate case. After passing the neutral point, the asymmetry level decreased until the level reached zero at the second bifurcation point (4), where w_{mid} returned to its stable primary path and continued following the path.

4.5 Solution method for the nonlinear dynamic analysis of post-buckled plates

For time integration procedure, the Newmark-beta method [60] was applied to the nonlinear FEM shown in Equations (2.70) to (2.92), in which damping effects were not considered. Damping effects will be investigated in future works. In addition, the Newton-Raphson method was employed to solve nonlinear equations within each time step.

In this section, the Newmark-beta method is presented based on the works of Paultre and Chopra in [61] and [62], respectively. Using the sth-degree Taylor polynomial of f at t_n, the state of a dynamic system at a given time $t_{n+1} = t_n + \Delta t$ is given by

$$f(t_n + \Delta t) = f(t_n) + \Delta t f'(t_n) + \frac{\Delta^2}{2} f''(t_n) + ... + \frac{\Delta t^s}{s!} f^{(s)}(t_n) + R_s(t), \tag{4.20}$$

in which $R_s(t)$ is the integral form of the remainder of the Taylor series [63] and is given by

$$R_s(t) = \frac{1}{s!} \int_{t_n}^{t_n+\Delta t} (t_n + \Delta t - \tau)^s f^{(s+1)}(\tau) d\tau. \tag{4.21}$$

The velocity and displacement at time t_{n+1} can be represented using zeroth- and first-degree Taylor polynomials, respectively.

$$\{\dot{u}\}_{n+1} = \{\dot{u}\}_n + \int_{t_n}^{t_n+\Delta t} \{\ddot{u}(\tau)\} d\tau, \tag{4.22}$$

$$\{u\}_{n+1} = \{u\}_n + \Delta t \{\dot{u}\}_n + \int_{t_n}^{t_n+\Delta t} (t_{n+1} - \tau)\{\ddot{u}(\tau)\} d\tau, \tag{4.23}$$

in which $\{\dot{u}\}_{n+1} = \{\dot{u}(t_{n+1})\}$ and $\{u\}_{n+1} = \{u(t_{n+1})\}$. In order to find the expression of $\{\ddot{u}(\tau)\}$ in the remainder, finding the Taylor series of $\{\ddot{u}(\tau)\}$ at t_n and t_{n+1},

$$\{\ddot{u}(t_n)\} = \{\ddot{u}(\tau)\} + (t_n - \tau)\{u^{(3)}(\tau)\} + \frac{(t_n - \tau)^2}{2!}\{u^{(4)}(\tau)\} + ... , \tag{4.24}$$

$$\{\ddot{u}(t_{n+1})\} = \{\ddot{u}(\tau)\} + (t_{n+1} - \tau)\{u^{(3)}(\tau)\} + \frac{(t_{n+1} - \tau)^2}{2!}\{u^{(4)}(\tau)\} + ... \tag{4.25}$$

Multiplying Equations (4.24) and (4.25) by $(1-\gamma)$ and γ, respectively and summing those equations yields

$$\{\ddot{u}(\tau)\} = (1-\gamma)\{\ddot{u}\}_n + \gamma\{\ddot{u}\}_{n+1} + (\tau - t_n - \gamma\Delta t)\{u^{(3)}(\tau)\} + O\Big(\Delta t^2\{u^{(4)}(\tau)\}\Big). \quad (4.26)$$

In the same way, multiplying Equations (4.24) and (4.25) by $(1-2\beta)$ and 2β, respectively and summing those equations yields

$$\{\ddot{u}(\tau)\} = (1-2\beta)\{\ddot{u}\}_n + 2\beta\{\ddot{u}\}_{n+1} + (\tau - t_n - 2\beta\Delta t)\{u^{(3)}(\tau)\} + O\Big(\Delta t^2\{u^{(4)}(\tau)\}\Big). \quad (4.27)$$

Substituting Equation (4.26) into the integral term in Equation (4.22) and applying the generalized first mean value theorem for integrals [64] to the third and subsequent terms,

$$\begin{aligned}
\int_{t_n}^{t_{n+1}} \{\ddot{u}(\tau)\}d\tau =& \int_{t_n}^{t_{n+1}} \Big[(1-\gamma)\{\ddot{u}\}_n + \gamma\{\ddot{u}\}_{n+1} + (\tau - t_n - \gamma\Delta t)\{u^{(3)}(\tau)\} \\
&+ O\Big(\Delta t^2\{u^{(4)}(\tau)\}\Big)\Big]d\tau \\
=&(1-\gamma)\Delta t\{\ddot{u}\}_n + \gamma\Delta t\{\ddot{u}\}_{n+1} + \{u^{(3)}(\tilde{\tau})\}\int_{t_n}^{t_{n+1}} \Big[(\tau - t_n - \gamma\Delta t)\Big]d\tau \\
&+ \int_{t_n}^{t_{n+1}} \Big[O\Big(\Delta t^2\{u^{(4)}(\tau)\}\Big)\Big]d\tau \\
=&(1-\gamma)\Delta t\{\ddot{u}\}_n + \gamma\Delta t\{\ddot{u}\}_{n+1} + \Big(\frac{1}{2} - \gamma\Big)\Delta t^2\{u^{(3)}(\tilde{\tau})\} \\
&+ O\Big(\Delta t^3\{u^{(4)}(\tilde{\tau})\}\Big), \qquad t_n < \tilde{\tau} < t_{n+1}.
\end{aligned} \quad (4.28)$$

Following the same procedure by substituting Equation (4.27) into the integral term in Equation (4.23),

$$\begin{aligned}
\int_{t_n}^{t_{n+1}} (t_{n+1} - \tau)\{\ddot{u}(\tau)\}d\tau =& (\frac{1}{2} - \beta)\Delta t^2\{\ddot{u}\}_n + \beta\Delta t^2\{\ddot{u}\}_{n+1} + \Big(\frac{1}{6} - \beta\Big)\Delta t^3\{u^{(3)}(\tilde{\tau})\} \\
&+ O\Big(\Delta t^4\{u^{(4)}(\tilde{\tau})\}\Big), \qquad t_n < \tilde{\tau} < t_{n+1}.
\end{aligned} \quad (4.29)$$

Substituting Equations (4.28) and (4.29) into Equations (4.22) and (4.23),

$$\begin{aligned}\{\dot{u}\}_{n+1} =&\{\dot{u}\}_n + (1-\gamma)\Delta t\{\ddot{u}\}_n + \gamma\Delta t\{\ddot{u}\}_{n+1} + \Big(\frac{1}{2}-\gamma\Big)\Delta t^2\{u^{(3)}(\tilde{\tau})\} \\ &+ O\Big(\Delta t^3\{u^{(4)}(\tilde{\tau})\}\Big), \qquad t_n < \tilde{\tau} < t_{n+1},\end{aligned} \tag{4.30}$$

$$\begin{aligned}\{u\}_{n+1} =&\{u\}_n + \Delta t\{\dot{u}\}_n + (\frac{1}{2}-\beta)\Delta t^2\{\ddot{u}\}_n + \beta\Delta t^2\{\ddot{u}\}_{n+1} \\ &+ \Big(\frac{1}{6}-\beta\Big)\Delta t^3\{u^{(3)}(\tilde{\tau})\} + O\Big(\Delta t^4\{u^{(4)}(\tilde{\tau})\}\Big), \qquad t_n < \tilde{\tau} < t_{n+1}.\end{aligned} \tag{4.31}$$

Considering Δt is generally set small, terms having higher order than Δt and Δt^2 for the velocity and the displacement, respectively can be ignored for many cases. Thus, the velocity $\dot{u}_{n+1}$ and the displacement u_{n+1} at the end of the integration time step are estimated by

$$\{\dot{u}\}_{n+1} = \{\dot{u}\}_n + [(1-\gamma)\Delta t]\{\ddot{u}\}_n + (\gamma\Delta t)\{\ddot{u}\}_{n+1}, \tag{4.32}$$

$$\{u\}_{n+1} = \{u\}_n + (\Delta t)\{\dot{u}\}_n + \Big[\Big(\frac{1}{2}-\beta\Big)\Delta t^2\Big]\{\ddot{u}\}_n + [\beta\Delta t^2]\{\ddot{u}\}_{n+1}, \tag{4.33}$$

in which $\gamma = \frac{1}{2}$ and $\beta = \frac{1}{4}$ (i.e., the average acceleration method or trapezoidal rule) were chosen in this work to make time integration unconditionally stable.

The effective force vector at time step $n+1$, $\{\hat{F}^e\}_{n+1}$, is given by

$$\{\hat{F}\}_{n+1} = \{F\}_{n+1} + a_1\{u\}_n + a_2\{\dot{u}\}_n + [M]\{\ddot{u}\}_n, \tag{4.34}$$

in which

$$a_1 = \frac{4}{(\Delta t)^2}[M], \qquad a_2 = \frac{4}{\Delta t}[M]. \tag{4.35}$$

At each iteration j within the time step $n+1$, the residual force $\{\hat{R}\}^{(j)}_{n+1}$ is given by

$$\{\hat{R}\}^{(j)}_{n+1} = \{\hat{F}\}_{n+1} - \{f_s\}^{(j)}_{n+1} - a_1\{u\}^{(j)}_{n+1}, \tag{4.36}$$

in which $\{f_s\}_{n+1}^{(j)} = [K]_{n+1}^{(j)}\{u\}_{n+1}^{(j)}$. The effective tangent stiffness matrix is given by

$$[\hat{K}_T]_{n+1}^{(j)} = [K_T]_{n+1}^{(j)} + a_1. \tag{4.37}$$

The displacement vector increment $\{\Delta u\}_{n+1}^{(j)}$ can be obtained by solving

$$[\hat{K}_T]_{n+1}^{(j)}\{\Delta u\}_{n+1}^{(j)} = \{\hat{R}\}_{n+1}^{(j)}. \tag{4.38}$$

Thus, the displacement vector $\{u\}_{n+1}^{(j+1)}$ is given by

$$\{u\}_{n+1}^{(j+1)} = \{u\}_{n+1}^{(j)} + \{\Delta u\}_{n+1}^{(j)}. \tag{4.39}$$

At the end of the final iteration j within the time step $n+1$, velocity and acceleration vectors are given by

$$\{\dot{u}\}_{n+1} = \frac{2}{\Delta t}\Big(\{u\}_{n+1} - \{u\}_n\Big) - \{\dot{u}\}_n, \tag{4.40}$$

$$\{\ddot{u}\}_{n+1} = \frac{4}{(\Delta t)^2}\Big(\{u\}_{n+1} - \{u\}_n\Big) - \frac{4}{\Delta t}\{\dot{u}\}_n - \{\ddot{u}\}_n. \tag{4.41}$$

Equation (4.41) can be obtained by rearranging Equation (4.33) about $\{\ddot{u}\}_{n+1}$ while Equation (4.40) can be derived by substituting Equation (4.41) into Equation (4.32).

4.6 Nonlinear dynamic analysis of post-buckled plates: conforming elements

In this section, the nonlinear FEM was simulated using MATLAB with the Hermite interpolation functions for conforming elements to characterize the nonlinear dynamic behaviors of post-buckled plates modeled using rectangular conforming elements. Since the modeling plate was used as a specimen for this analysis, this analysis is exploratory due to the same reasons discussed for the static analysis with the identical plate.

The mesh illustrated in Figure 4.4 was utilized and the post-buckled plate specimen was generated using the data obtained from the equilibrium path of the initially-flat modeling plate (Figure 4.5). Considering the buckled depth of the midpoint of the post-buckled AFRL plate was -1.3896 mm as shown in Figure 3.19, the post-buckled modeling plate was modeled to have the same buckled depth at its midpoint. Figure 4.8 demonstrates the comparison of the buckled shapes between the DIC reconstruction of the AFRL plate and the conforming element model of the modeling plate (named *the CF model*). In the figure, the buckled shapes of the AFRL plate were presented by shifting and rotating the shapes shown in Figure 3.19 to be compared to the shapes of the CF model at the same angles. As observed from the figures on the right side, the CF model had buckled depth symmetric along both the width and the length, which is a critical limitation of FEMs consisting of rectangular conforming elements. Thus, the CF model could not reproduce the same buckled shape as the post-buckled AFRL plate.

To characterize the nonlinear dynamic response of the CF model, three types of force-dwell simulations were conducted by applying: (i) 4 g-75 Hz, (ii) 8 g-75 Hz, and (iii) 10 g-75 Hz harmonic loading. The dynamic response was analyzed at each time step using the aforementioned Newmark-beta method procedure.

Figure 4.9 illustrates w_{mid} and snapshots of corresponding deflected shapes when the CF model was subjected to 4 g-75 Hz harmonic loading. As shown in Figure 4.9a, the midpoint exhibited the nonlinear single-well response oscillating between w_{mid} = -1.1262 and -1.6352 mm and could not snap into the other equilibrium point since the forcing amplitude was not enough for snap-through. It was observed from the snapshots of the deflected shapes that the first mode dominated the response.

Maintaining the frequency, the amplitude was gradually amplified to find a chaotic snap-through boundary (i.e. the Chaotic snap starts (↑) boundary shown in Figure 3.15). When the amplitude reached 8 g, the CF model began to demonstrate chaotic snap-through as shown in Figure 4.10. When the model passed the neutral point at (3), (4), and (5), the plate exhibited different kinds of deflected shapes as illustrated in Figures 4.10d, 4.10e, and

4.10f, respectively. The model showed an asymmetric deflected shape at (4) where $w_{3/4}$ was higher than $w_{1/4}$; in contrast, at (5), $w_{1/4}$ of the deflected shape was higher than its $w_{3/4}$. The deflected shape at (3) appeared to be flat and this phenomenon was also observed in the full-field measurement shown in Figure 3.24e. Figure 4.10g indicates the influence of the third mode on the deflected shape.

The forcing amplitude was increased further to find a periodic snap-through boundary (i.e. the Periodic snap starts (↑) boundary shown in Figure 3.15). When the amplitude reached 10 g, nearly periodic snap-through was observed as shown in Figure 4.11. The midpoint persistently snapped into one of the two stable equilibria. Similar to the chaotic snap-through case, when the model passed through the neutral point, the periodic snap-through case also exhibited asymmetric (Figures 4.11f and 4.11h) and flat (Figure 4.11b) deflected shapes in addition to the influence of the third mode (Figure 4.11d).

From the dynamic simulation results of the CF model, the several characteristics of conforming elements were observed. While the CF model showed deflected shapes asymmetric along the length when the model was subjected to harmonic loading, all the deflected shapes were symmetric along the width and thus the model did not exhibit twisting deformation which was observed from the DIC full-field measurement of the dynamic response of the post-buckled AFRL plate. This phenomenon is caused by the inherent limitation of the models composed of conforming elements, which generated the motivation for modeling the post-buckled AFRL plate and simulating its dynamic behaviors using nonconforming elements.

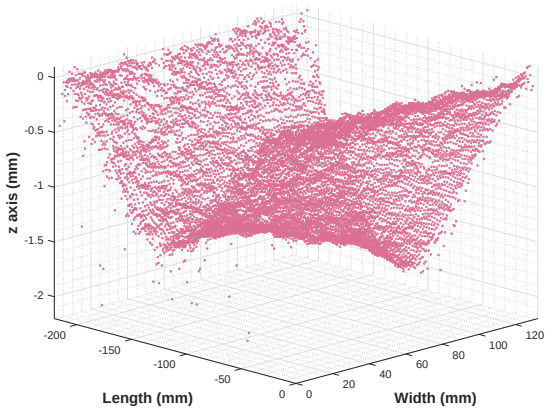

(a) DIC: 3-D buckled shape.

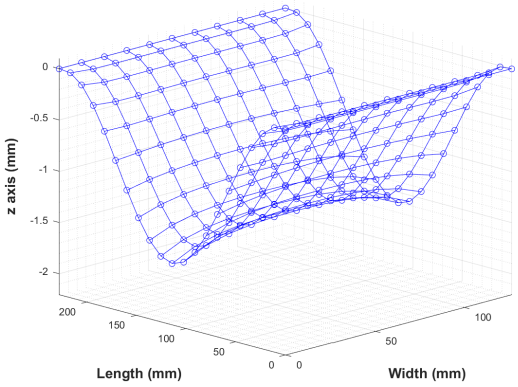

(b) CF model: 3-D buckled shape.

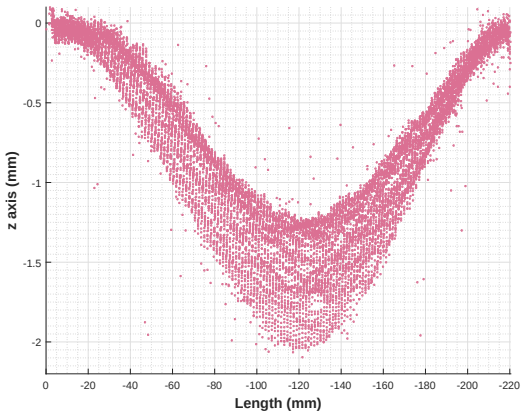

(c) DIC: buckled shape along the length.

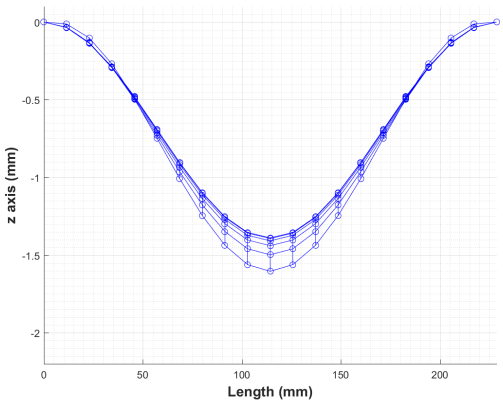

(d) CF model: buckled shape along the length.

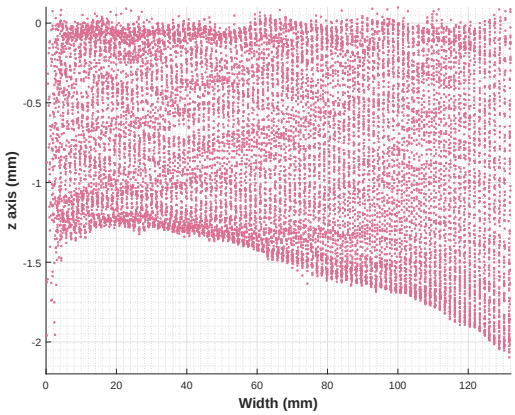

(e) DIC: buckled shape along the width.

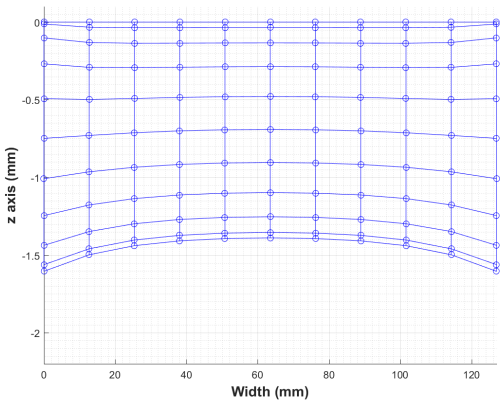

(f) CF model: buckled shape along the width.

Figure 4.8: Comparison of the buckled shapes between the DIC reconstruction of the AFRL plate and the conforming element model of the modeling plate (the CF model).

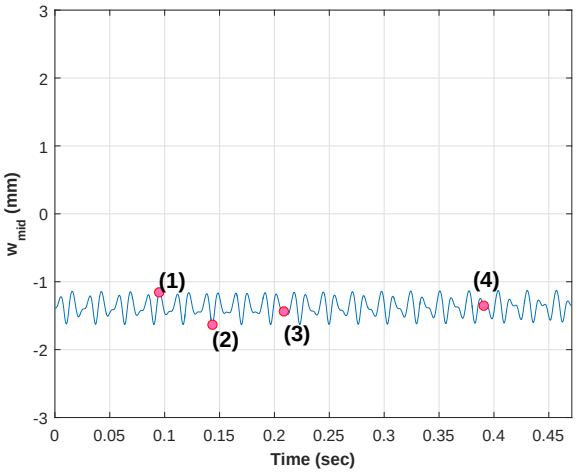

(a) A single-well response of the midpoint.

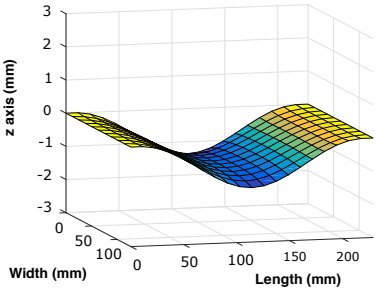

(b) Deflected shape at (1).

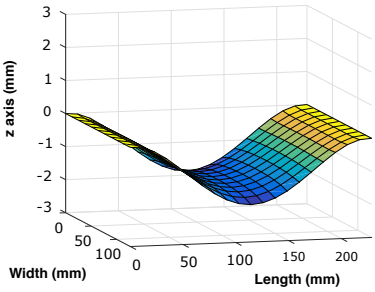

(c) Deflected shape at (2).

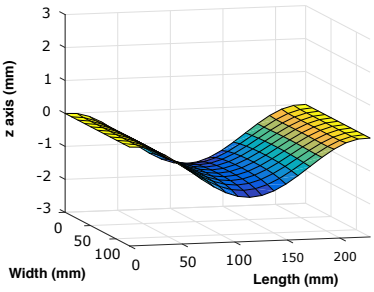

(d) Deflected shape at (3).

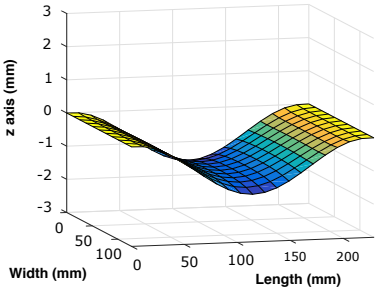

(e) Deflected shape at (4).

Figure 4.9: w_{mid} and snapshots of corresponding deflected shapes when the CF model was subjected to 4 g-75 Hz harmonic loading.

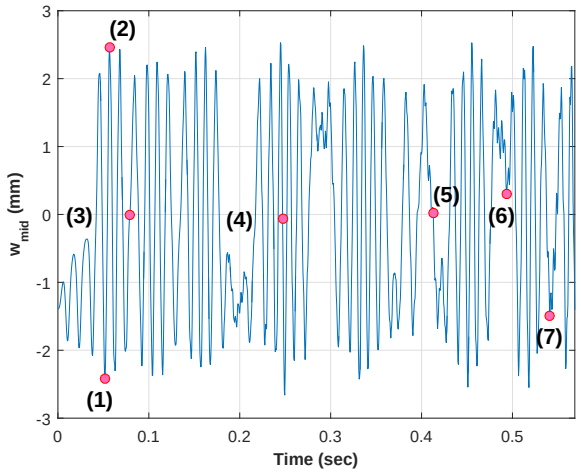

(a) Chaotic snap-through response of the midpoint. The numbers (3) and (4) are intentionally written away from their points not to obstruct the plot.

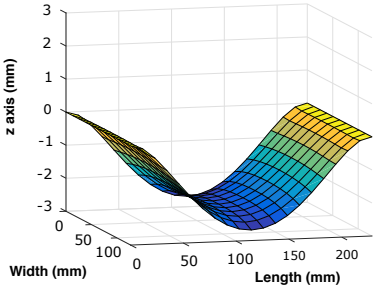

(b) Deflected shape at (1).

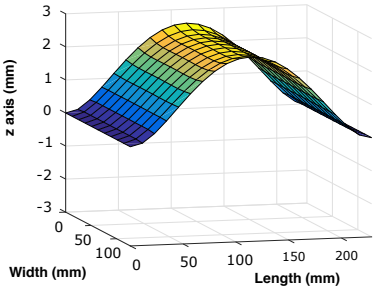

(c) Deflected shape at (2).

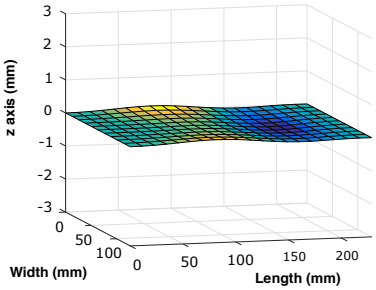

(d) Deflected shape at (3) and time = 0.0790 sec.

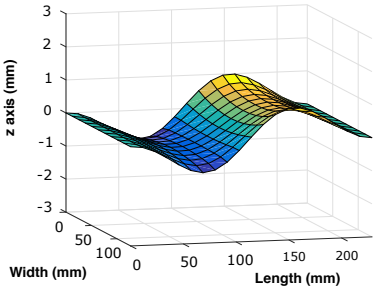

(e) Deflected shape at (4) and time = 0.2471 sec.

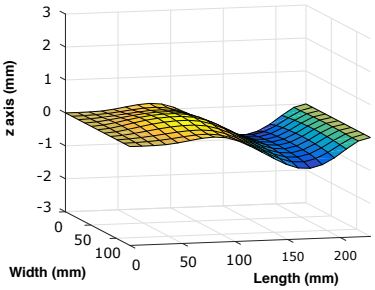

(f) Deflected shape at (5).

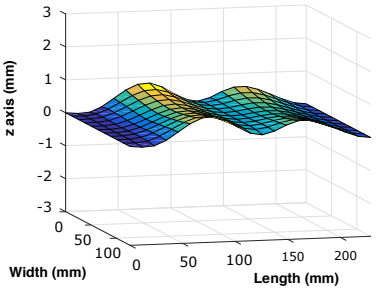

(g) Deflected shape at (6).

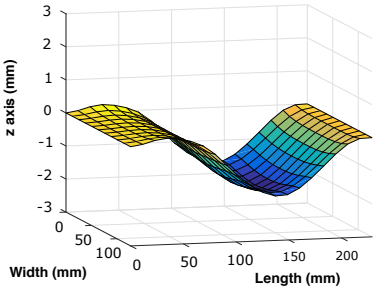

(h) Deflected shape at (7).

Figure 4.10: w_{mid} and snapshots of corresponding deflected shapes when the CF model was subjected to 8 g-75 Hz harmonic loading.

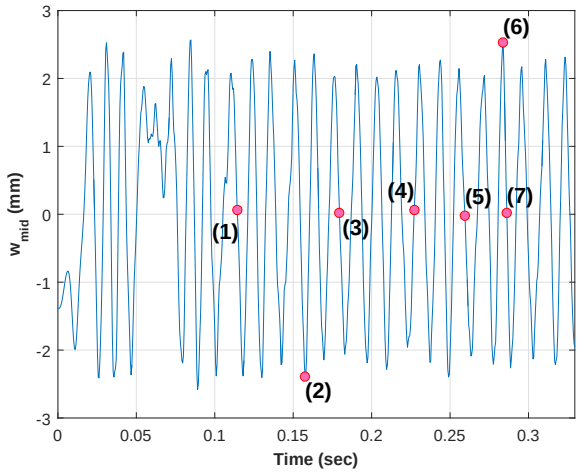

(a) Periodic snap-through response of the midpoint.

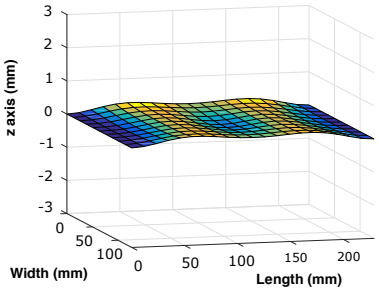

(b) Deflected shape at (1).

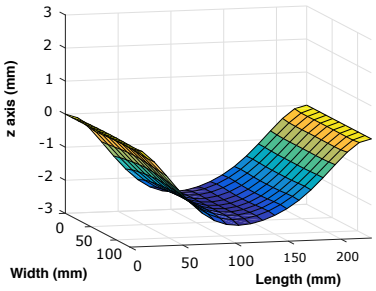

(c) Deflected shape at (2).

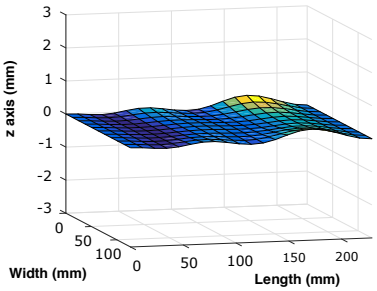

(d) Deflected shape at (3).

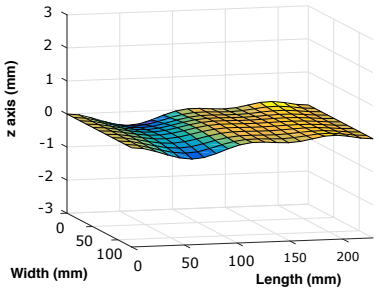

(e) Deflected shape at (4).

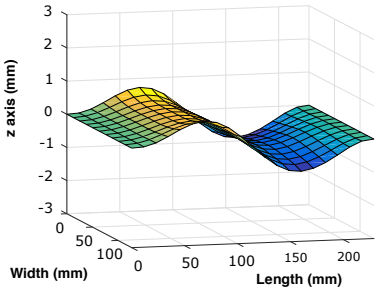

(f) Deflected shape at (5).

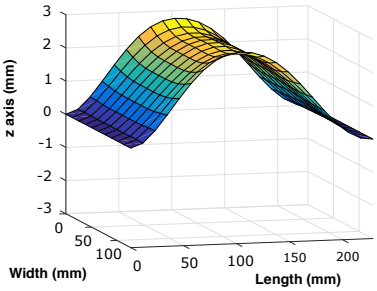

(g) Deflected shape at (6).

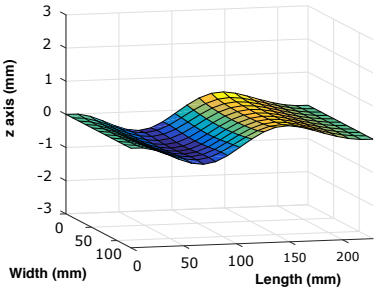

(h) Deflected shape at (7).

Figure 4.11: w_{mid} and snapshots of corresponding deflected shapes when the CF model was subjected to 10 g-75 Hz harmonic loading.

4.7 Nonlinear dynamic analysis of post-buckled plates: nonconforming elements

In this section, the AFRL plate was modeled using the Hermite interpolation functions for the nonconforming elements described in Table 4.3 and Equation (4.4), and the model is named *the NCF model*.

The NCF model was modeled with the FEM mesh having 21 × 10 elements (210 elements) and 242 nodes as shown in Figure 4.12. The nodes number 232 to 242 are indicated out of the mesh since those nodes generated very narrow elements which are enlarged in Figure 4.13. Among those 210 elements, the 200 elements were modeled as rectangular elements (the nodes number 1 to 231) whose total dimension is 228.6 mm × 127.0 mm while the other 10 elements (the nodes number 221 to 242) were modeled as trapezoidal elements whose dimension is 1.67 to 7.00 $\times 10^{-2}$ mm × 127.0 mm as shown in Figure 4.13. Those additional lengths were obtained by trial and error to reproduce the buckled shape of the AFRL plate.

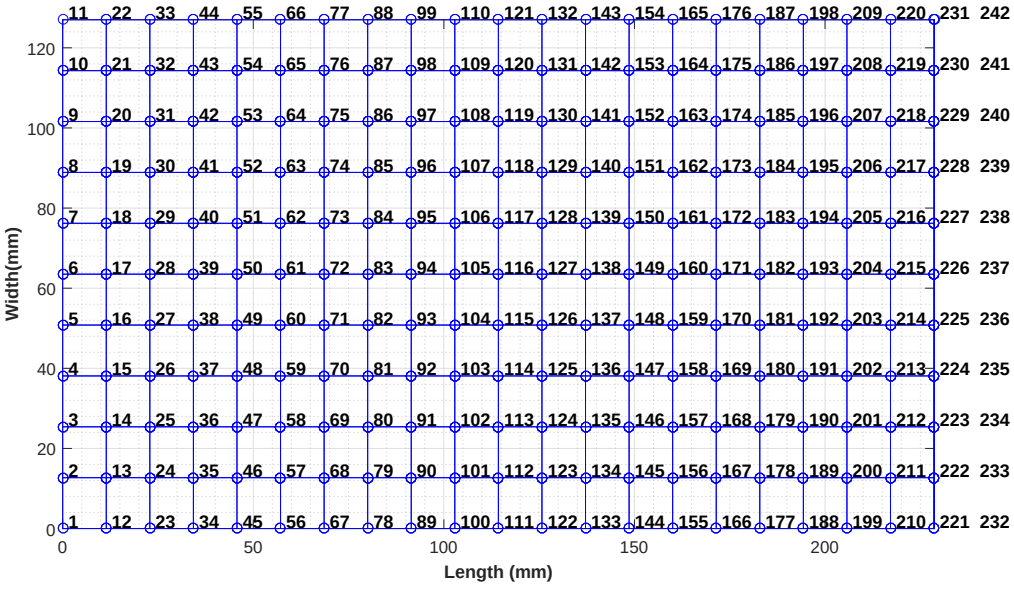

Figure 4.12: FEM mesh for the NCF model with 242 nodes and 210 elements. The narrow elements consisting of the nodes number 221 to 242 are enlarged in Figure 4.13.

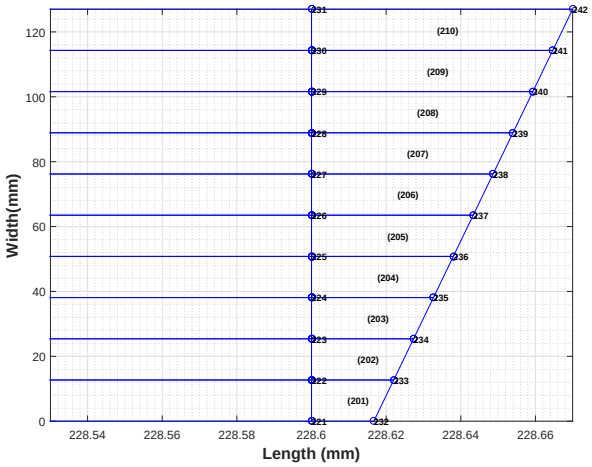

(a) Enlarged narrow edge elements of the initially-flat NCF model. The numbers next to the nodes (blue circles) are node numbers while the numbers inside the parentheses are element numbers.

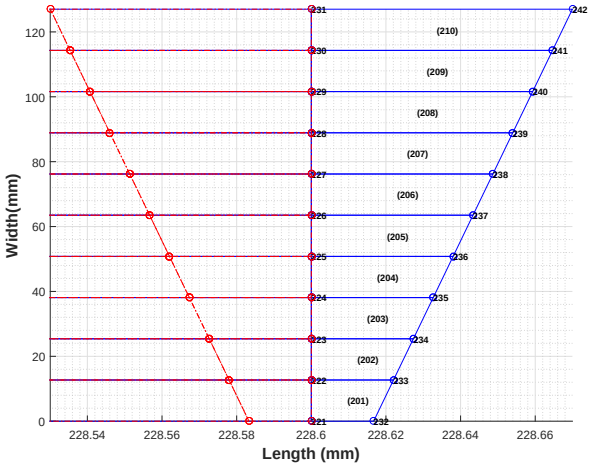

(b) Enlarged narrow edge elements of the buckled NCF model. The blue lines are the original mesh shape shown in (a) whereas the red lines are the deformed mesh.

Figure 4.13: Enlarged mesh of the edge of the initially-flat and buckled NCF models.

To buckle the initially-flat NCF model, the process used to physically buckle the AFRL plate at AFRL was employed and was simulated using MATLAB. The left-side edge along the nodes number 1 to 11 was set clamped in the program while the other edge along the nodes number 232 to 242 (named *the free edge*) was made free to move along the x-axis (i.e., length) direction. An axial loading was applied to the free edge of the original shape shown in Figure 4.13a and the edge was pushed until it matched the straight line along the nodes number 221 to 231, which is the clamp boundary. When the deformed free edge reached and matched the clamp boundary, the edge was set clamped at the position as demarcated as red lines shown in Figure 4.13b. The advantage of this method is that the free edge was maintained straight while being pushed and thus exactly matched the clamp boundary shown in Figure 3.16b. Figure 4.14 illustrates the superposition of the clamp and the deformed free edge. In addition, the buckled shape had the same horizontal length (along the x-axis) as the length of the hollow window of the clamp, 228.6 mm.

The buckled shape of the NCF model generated through the aforementioned process is

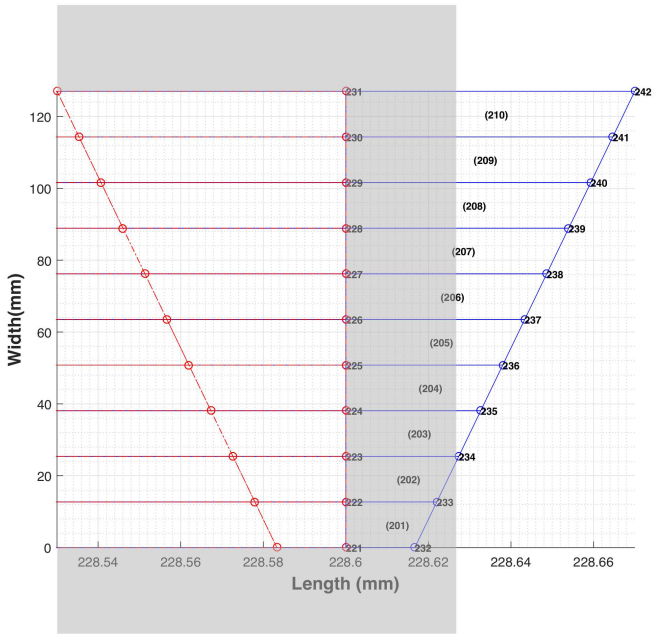

Figure 4.14: Superposition of the clamp (grey block) and the deformed free edge.

illustrated and is compared to the buckled shape of the AFRL plate as shown in Figure 4.15. Like the buckled shape comparison for the CF model, the length axis of the full-field measurement shown in the figures on the left side shows negative values since the figures illustrated in Figure 3.19 were shifted and rotated to be compared to the modeling results of the NCF model. Those negative values have the same meaning as the positive values in the length axis of the figures on the right side; that is, only absolute values in that axis are comparable.

The buckled shape of the NCF model well matched the full-field DIC measurement of the buckled shape of the AFRL plate. Similar to the buckled shape of the AFRL plate, the buckled shape of the NCF model was slightly biased to one side along the length as shown in Figure 4.15d. In addition, the buckled depth of the NCF model along the width was almost identical to the buckled depth of the AFRL plate, which varied from 1.3 to 2.1 mm. Figure 4.16 illustrates the superposition of the buckled shapes of the AFRL plate and NCF model at two different angles. This superposition was quantitatively analyzed as shown in Figure 4.17.

The figures illustrate cross-section views of the superposition and the numbers indicate the discrepancy as a percentage (%). The nodal values of the DIC measurement corresponding to the nodes of the NCF model were obtained by interpolating the values of the sampling points. It was observed from those figures that the DIC measurement was irregular for some parts and that the modeling result matched the measurement better for the parts having deeper buckled depth than the parts having smaller depth. Considering the irregularity of the DIC measurement, this modeling result of the NCF model was deemed acceptable based on the quantified discrepancies and thus this NCF model was used as a post-buckled plate specimen for dynamic analysis.

Using the NCF model, the forcing amplitude-ramp analysis was performed. Figure 4.18 demonstrates the modeling result of the dynamic response of the midpoint when the harmonic forcing amplitude gradually increased from 2 to 5.2 g maintaining the 85 Hz forcing frequency as shown in the bottom figure. The transition from the single-well response to the chaotic snap-through occurred at 3.6 g. With the further increase in the forcing amplitude, the chaotic snap-through shifted into the periodic snap-through at 4.8 g.

Figures 4.19 and 4.20 illustrate the enlarged chaotic and periodic snap-through parts of Figure 4.18 and the snapshots of the corresponding deflected shapes. The deflected shapes exhibited very similar patterns as observed from the DIC full-field measurement shown in Figure 3.24 including the twisting deformation.

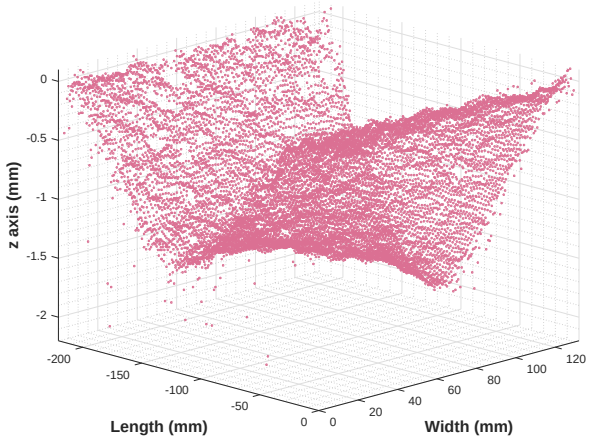

(a) DIC: 3-D buckled shape.

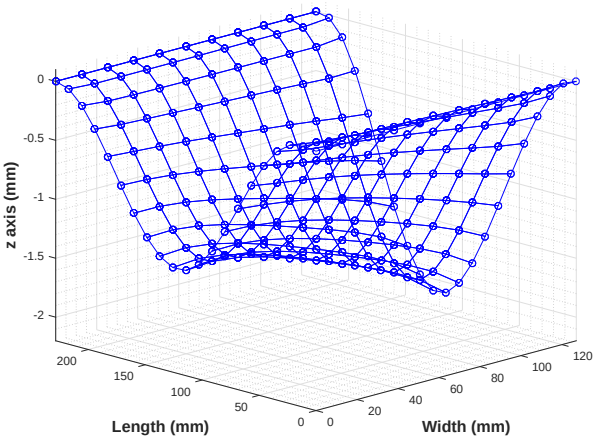

(b) NCF model: 3-D buckled shape.

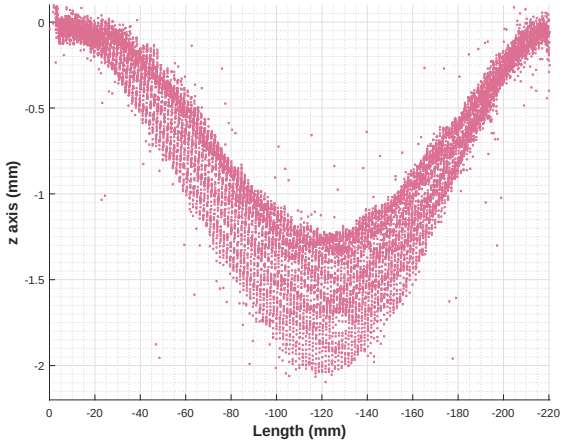

(c) DIC: buckled shape along the length.

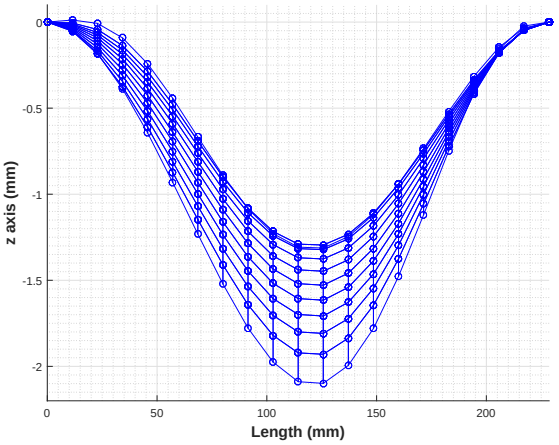

(d) NCF model: buckled shape along the length.

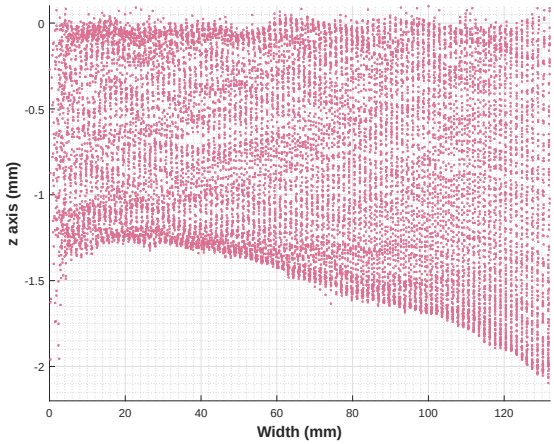

(e) DIC: buckled shape along the width.

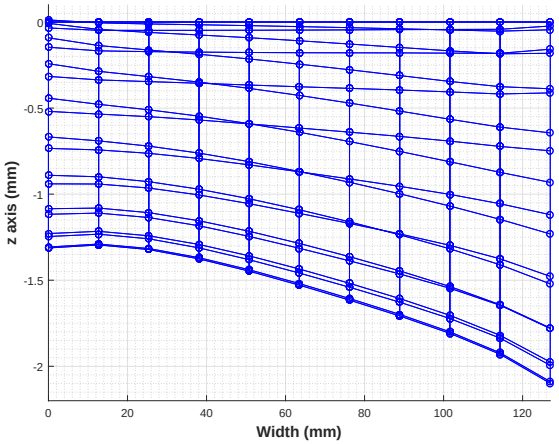

(f) NCF model: buckled shape along the width.

Figure 4.15: Comparison of the buckled shapes between the DIC reconstruction of the AFRL plate and the NCF model.

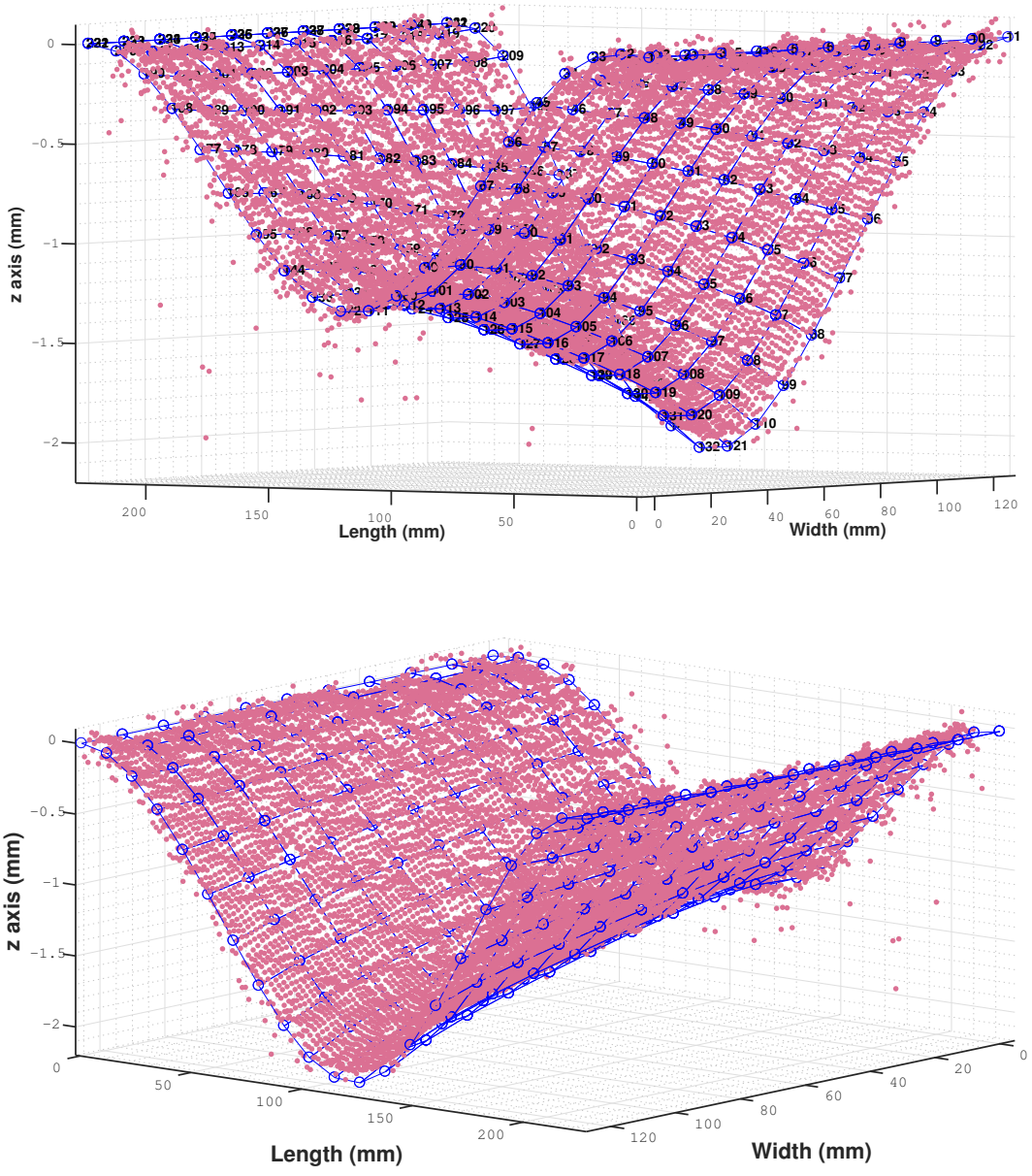

Figure 4.16: Superposition of the buckled shapes of the AFRL plate and NCF model.

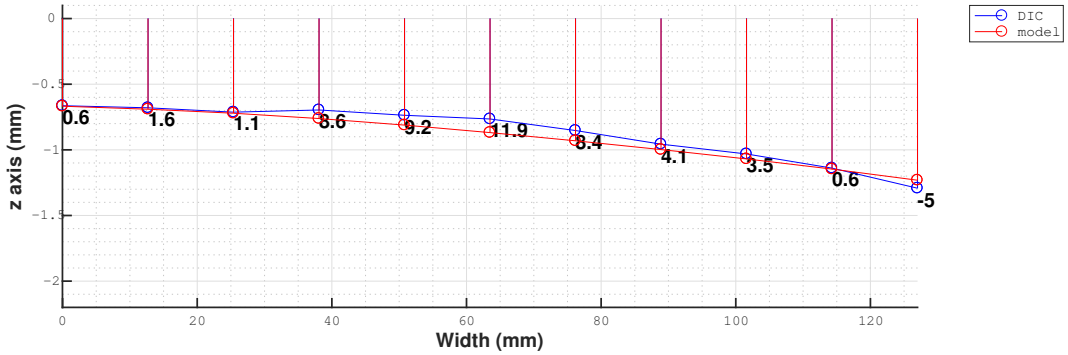

(a) Nodes number 67 to 77.

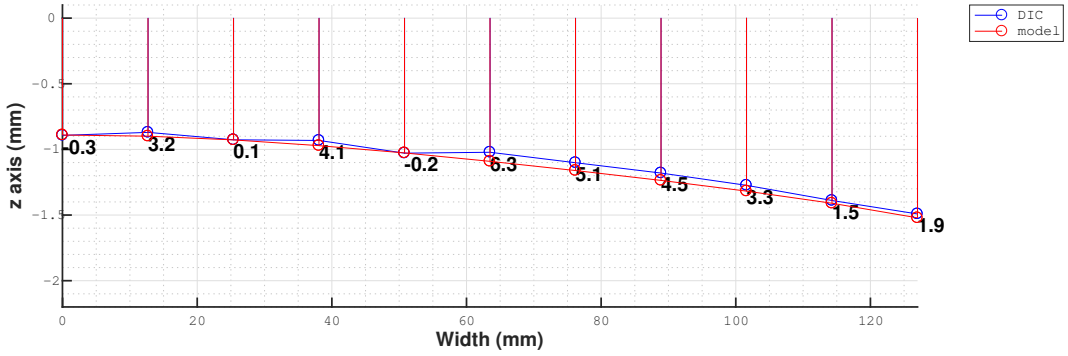

(b) Nodes number 78 to 88.

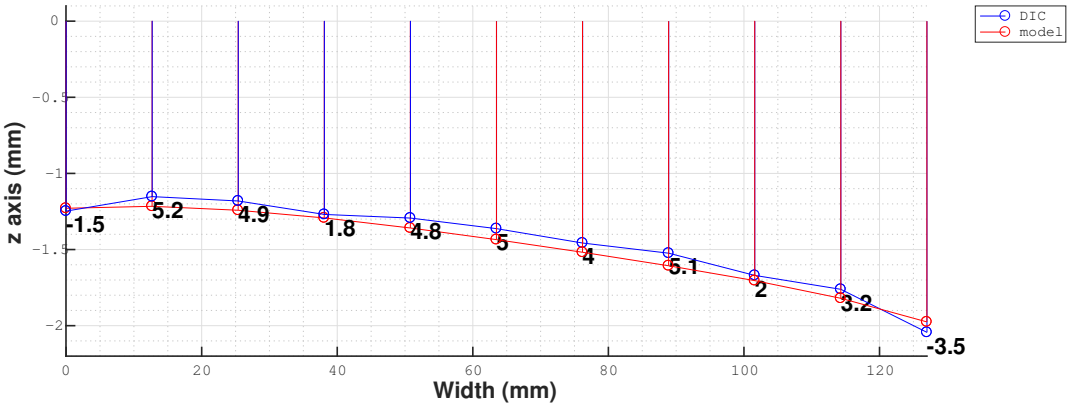

(c) Nodes number 100 to 110.

Figure 4.17: Cross-section view of the superposition shown in Figure 4.16. The circles are the positions of the nodes on the cross sections while the lines indicate buckled depth of the nodes. The blue lines are the cross sections of the DIC measurement of the AFRL plate while the red lines are the cross sections of the NCF model. The numbers written around the nodes indicate the discrepancy as a percentage (%).

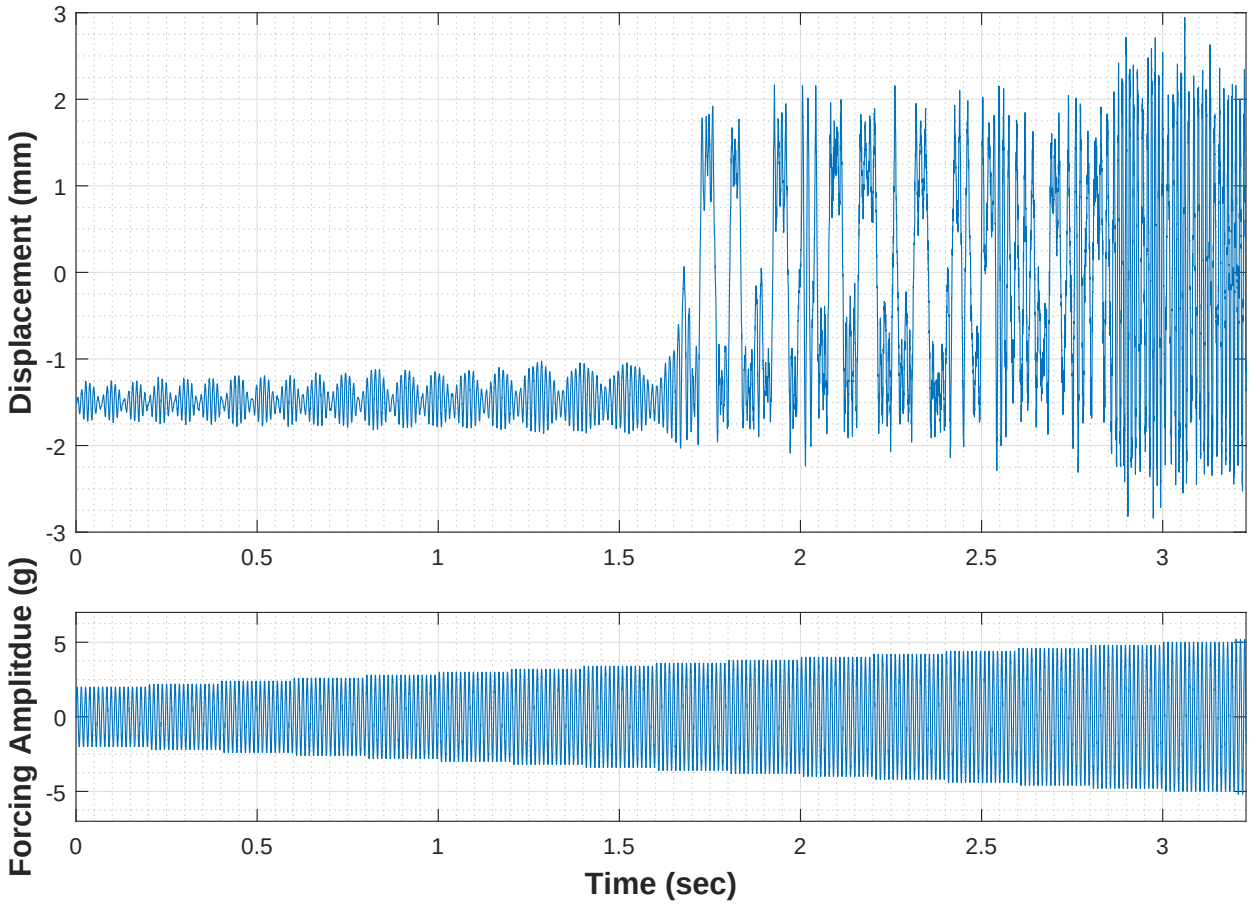

Figure 4.18: Dynamic response of the midpoint when the NCF model was subjected to the harmonic forcing (amplitude-ramp from 2 g- to 5.2 g-85 Hz).

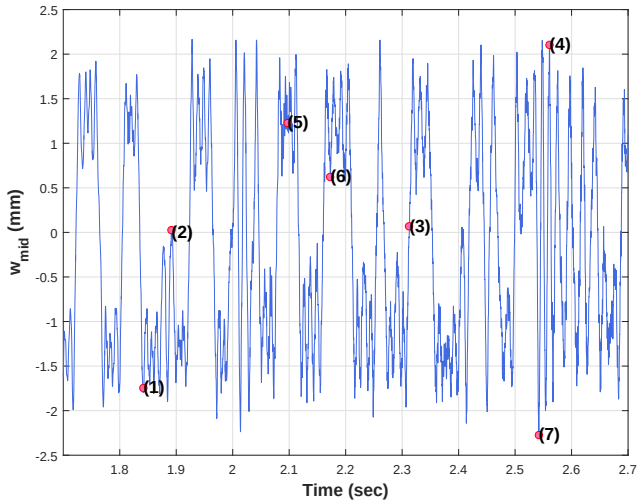

(a) Chaotic snap-through response (3.6 g- to 4.4 g-85 Hz).

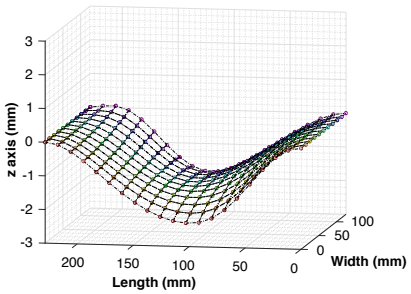

(b) Deflected shape at (1).

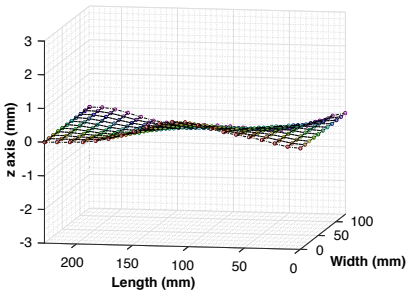

(c) Deflected shape at (2).

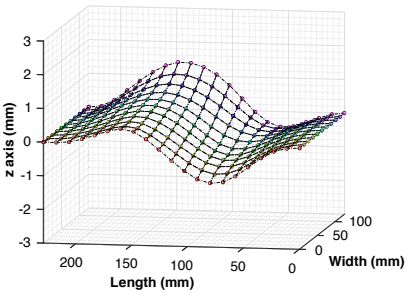

(d) Deflected shape at (3).

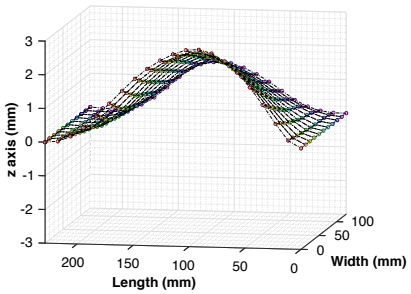

(e) Deflected shape at (4).

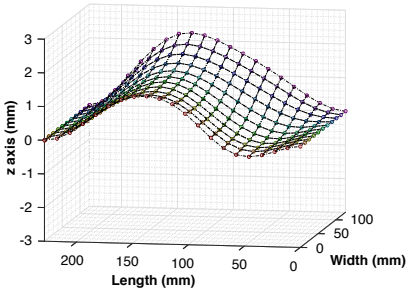

(f) Deflected shape at (5).

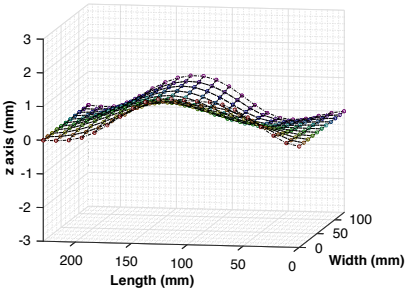

(g) Deflected shape at (6).

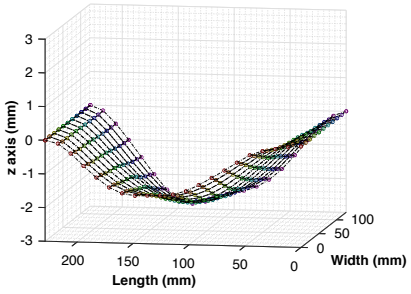

(h) Deflected shape at (7).

Figure 4.19: Enlarged chaotic snap-through part of Figure 4.18 and snapshots of corresponding deflected shapes.

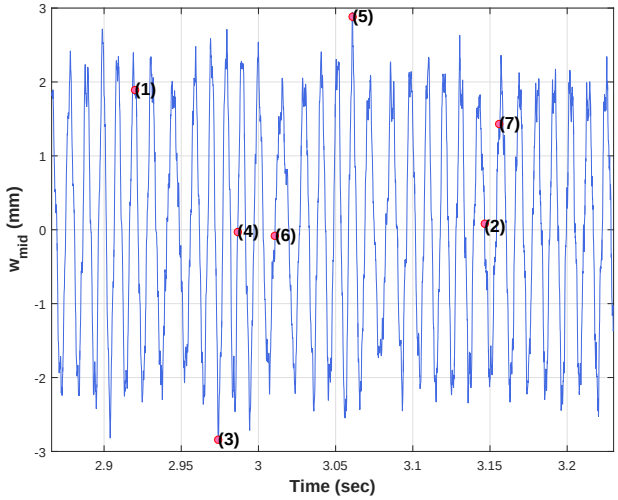

(a) Nearly periodic snap-through response (4.8 g-85 Hz).

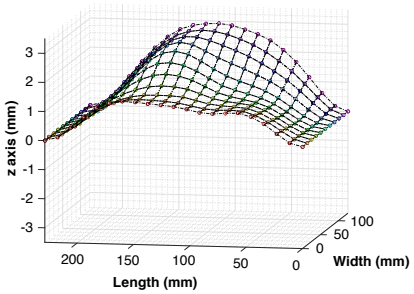

(b) Deflected shape at (1)

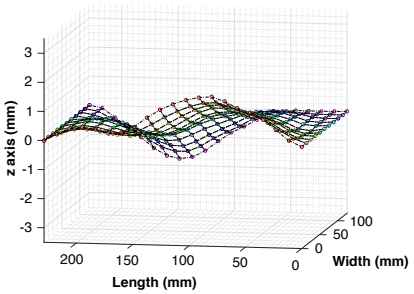

(c) Deflected shape at (2)

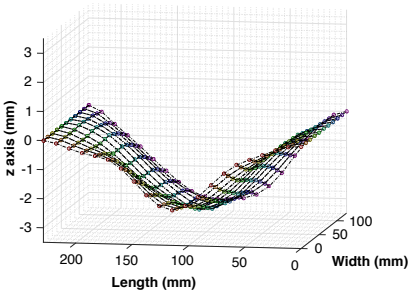

(d) Deflected shape at (3)

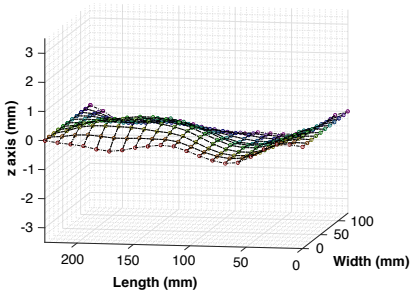

(e) Deflected shape at (4)

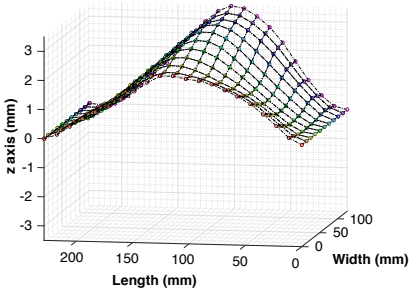

(f) Deflected shape at (5)

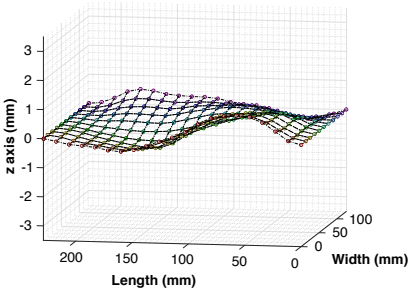

(g) Deflected shape at (6)

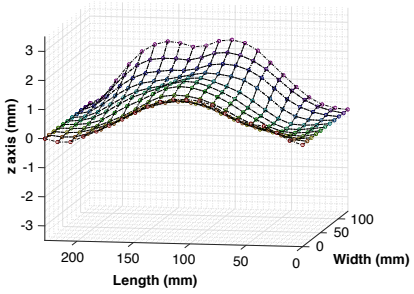

(h) Deflected shape at (7)

Figure 4.20: Enlarged nearly periodic snap-through part of Figure 4.18 and snapshots of corresponding deflected shapes.

4.8 Summary

In this chapter, the solution methods for the nonlinear static and dynamic analyses were discussed. Using those methods, the behaviors and characteristics of both conforming and nonconforming elements were investigated. The limitation of the FEM consisting of rectangular conforming elements was discussed. To remove the limitation, the buckled shape of the AFRL plate was modeled using nonconforming elements and the model showed a good agreement with the full-field measurement of the plate. Furthermore, the dynamic simulation of the model exhibited similar deflection patterns including twisting deformation as the dynamic response of the post-buckled AFRL plate. In Chapter 5, the frequency-sweep simulation results are presented and are compared with the vibrometer data.

Chapter 5

COMPARISON OF EXPERIMENTAL DATA AND MODELING RESULTS

5.1 Introduction

In Chapter 3, the methodology of data analysis and the experimental setup of the vibrometer experiment were discussed. In Chapter 4, the post-buckled AFRL plate was modeled using nonconforming elements and the model showed a good agreement with the full-field measurement of the buckled shape of the plate. In this chapter, the snap-through boundary of the post-buckled AFRL plate was investigated using the experimental data of forcing frequency-sweep tests collected from the vibrometer. In addition, using the model, forcing amplitude-ramp and frequency-sweep cases were simulated. The snap-through boundary of the model was generated based on the simulation results and was compared to the boundary found by the vibrometer measurement.

5.2 Vibrometer: frequency-sweep experiments

As discussed in Chapter 3, the vibrometer measured the dynamic response of the post-buckled AFRL plate during the frequency-sweep experiments, where the loading frequency was swept from 50 to 200 Hz. To investigate the boundary along the forcing amplitude axis in the harmonic forcing parameter (HFP) space, six data sets having distinct forcing amplitudes (2, 3, 4, 5, 6, and 7 g) were collected. Figures 5.1 to 5.6 demonstrate the transverse displacements of the vib-point (w_{vib}) responding to the changes in the forcing

frequency at each forcing amplitude.

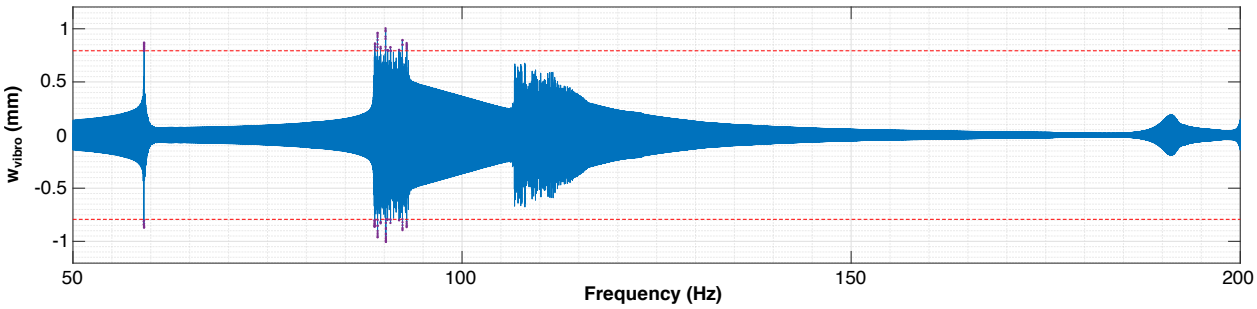

Figure 5.1: Response of the vib-point (w_{vib}) when 2 g harmonic loading was applied.

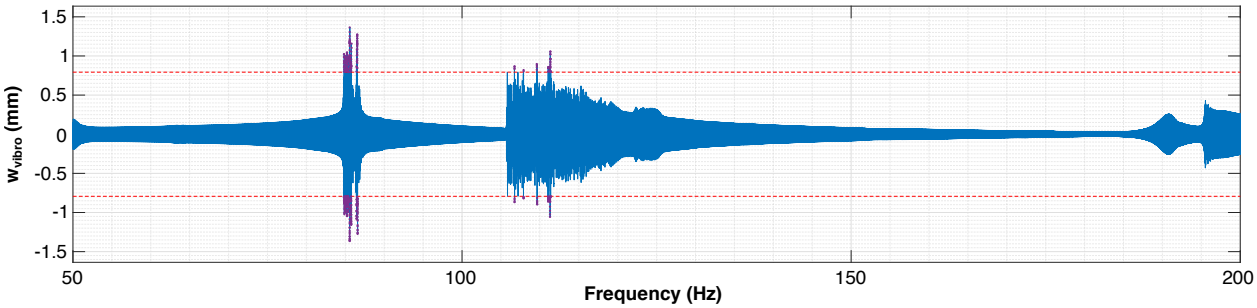

Figure 5.2: Response of the vib-point (w_{vib}) when 3 g harmonic loading was applied.

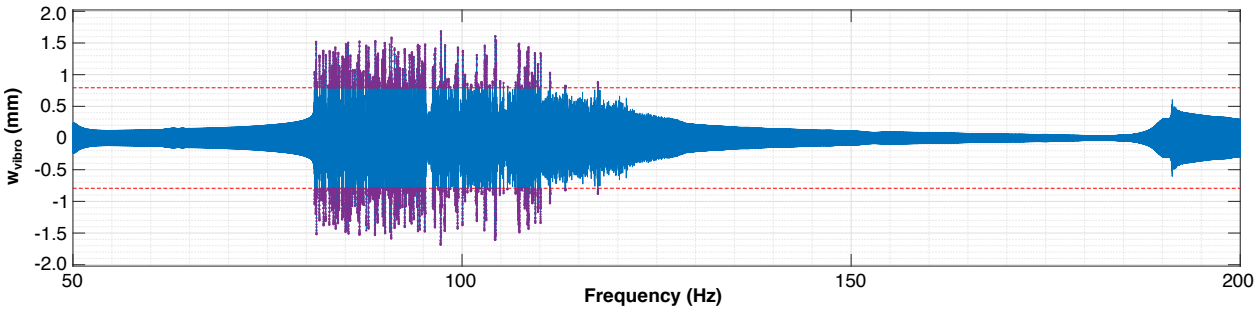

Figure 5.3: Response of the vib-point (w_{vib}) when 4 g harmonic loading was applied.

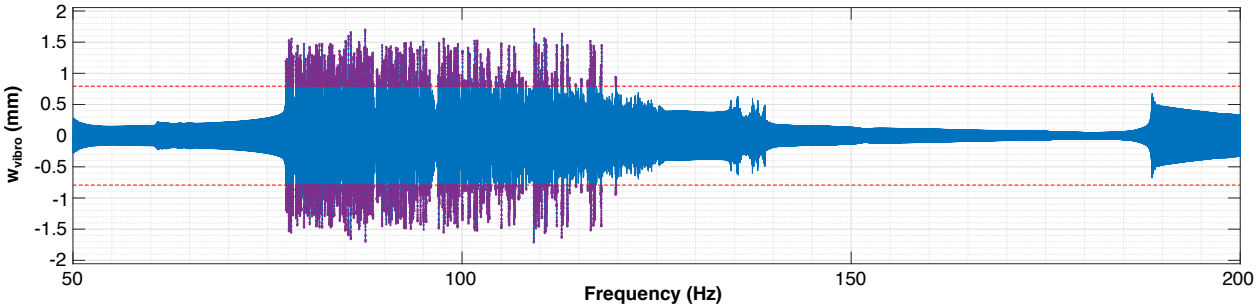

Figure 5.4: Response of the vib-point (w_{vib}) when 5 g harmonic loading was applied.

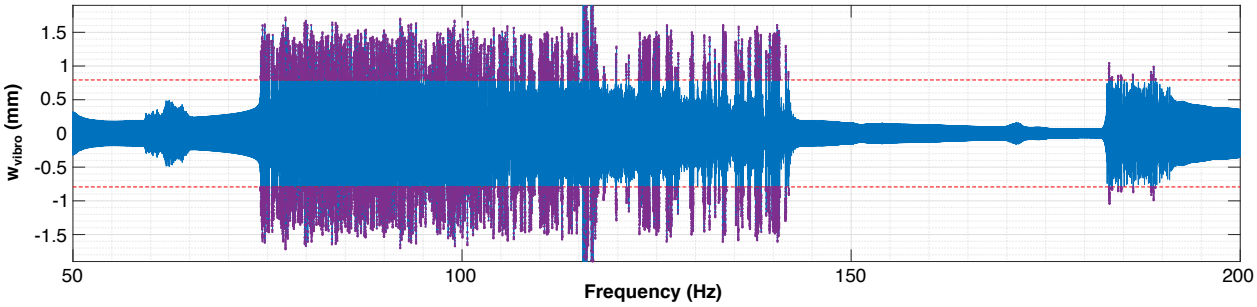

Figure 5.5: Response of the vib-point (w_{vib}) when 6 g harmonic loading was applied.

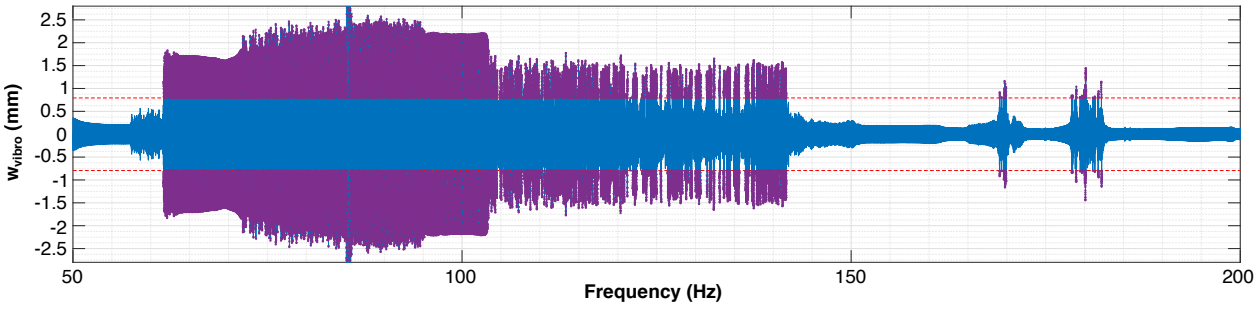

Figure 5.6: Response of the vib-point (w_{vib}) when 7 g harmonic loading was applied.

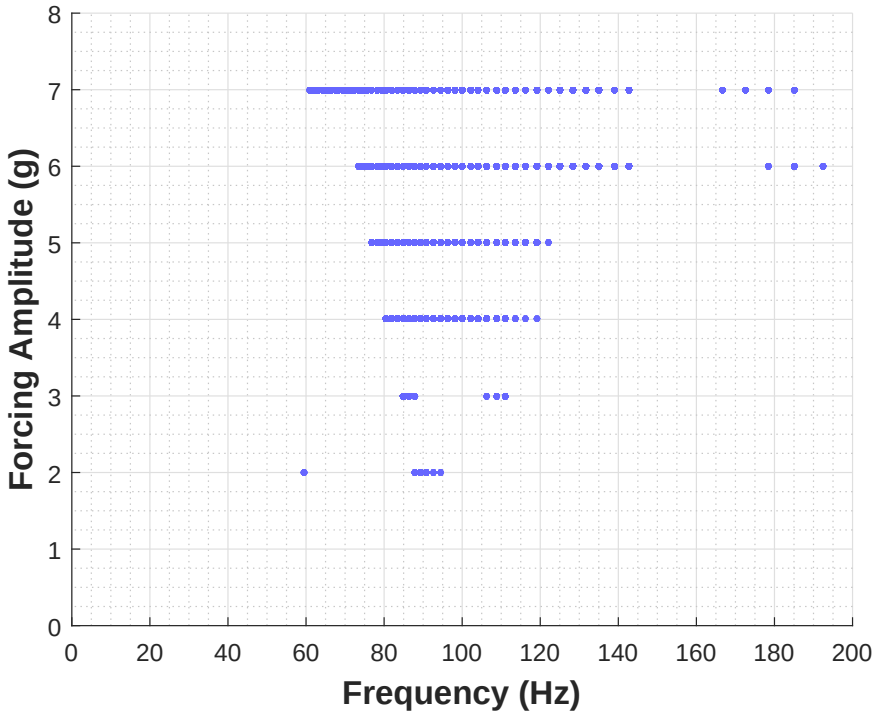

(a) Snap-through boundaries from the vibrometer data.

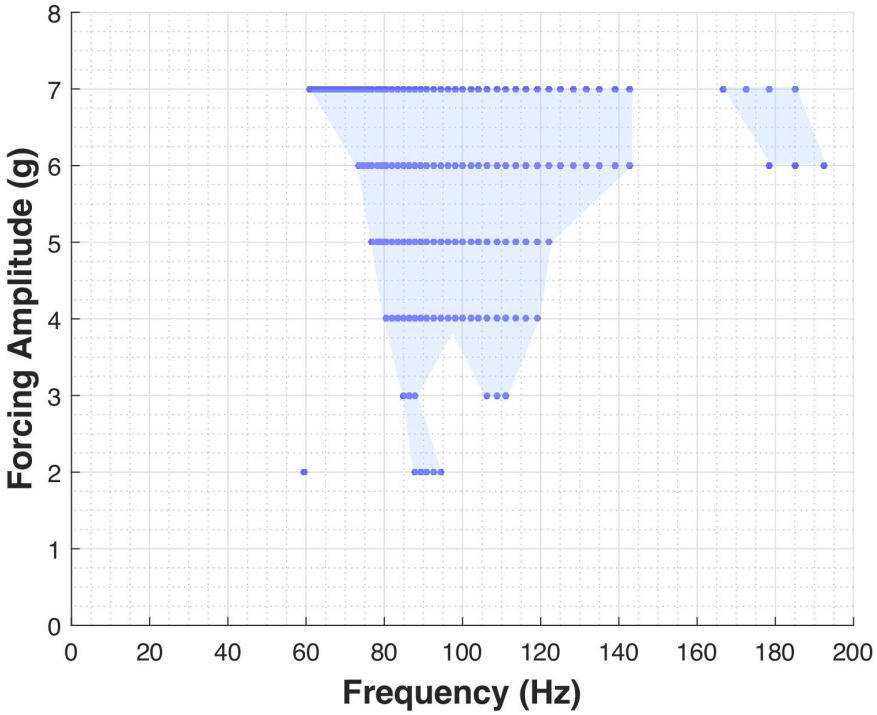

(b) Visualized snap-through boundaries.

Figure 5.7: Snap-through boundaries of the post-buckled AFRL plate in the harmonic forcing parameter space.

Collecting the purple points where snap-through likely occurred from those figures and marking them in the HFP space, the snap-through boundaries of the post-buckled AFRL plate were found and are illustrated in Figure 5.7. For visualization purposes, the edges of the discrete boundaries were connected and filled with color as shown in Figure 5.7b. The inner boundary between 3 g and 4 g was assumed in the figure since the data required to examine the part were not collected from the experiment. The purple point at 2 g-60 Hz appeared isolated from the two boundary regions and it was not confirmed whether the point was extended towards 3 g or 1 g and formed another region since the areas below 2 g and between 2 g and 3 g were not investigated in the experiments. Instead, the area was examined by the simulation results to find whether there was additional boundary region in that area.

5.3 Model: forcing amplitude-ramp analyses

In this section, the nonlinear dynamic response of the NCF model was simulated using MATLAB for the forcing amplitude-ramp cases. This simulation intended to investigate the areas not covered by the frequency-sweep simulation. Figures 5.8 to 5.12 illustrate the transverse displacement of the vib-point of the NCF model (w_{vibro}) responding to the changes in the forcing amplitude at the forcing frequencies: 60, 90, 110, 120, and 180 Hz. The 85 Hz case is presented in Chapter 4.

The analysis shown in Figure 5.8 was performed to investigate the area around the isolated point shown in Figure 5.7 and no snap-through was found in the area from the modeling result. For the 90 Hz case (Figure 5.9), the single-well response shifted to the chaotic snap-through response at 1.8 g and the snap-through continued through the simulation. In Figure 5.10 (the 110 Hz case), similar to the isolation point observed from the vibrometer measurement, the single snap-through at 3 g was observed before the chaotic snap-through started at 3.6 g. For the 120 Hz case (Figure 5.11), the chaotic snap-through started at 3.4 g and stopped in the middle of applying the 3.8 g forcing amplitude. The simulation illustrated

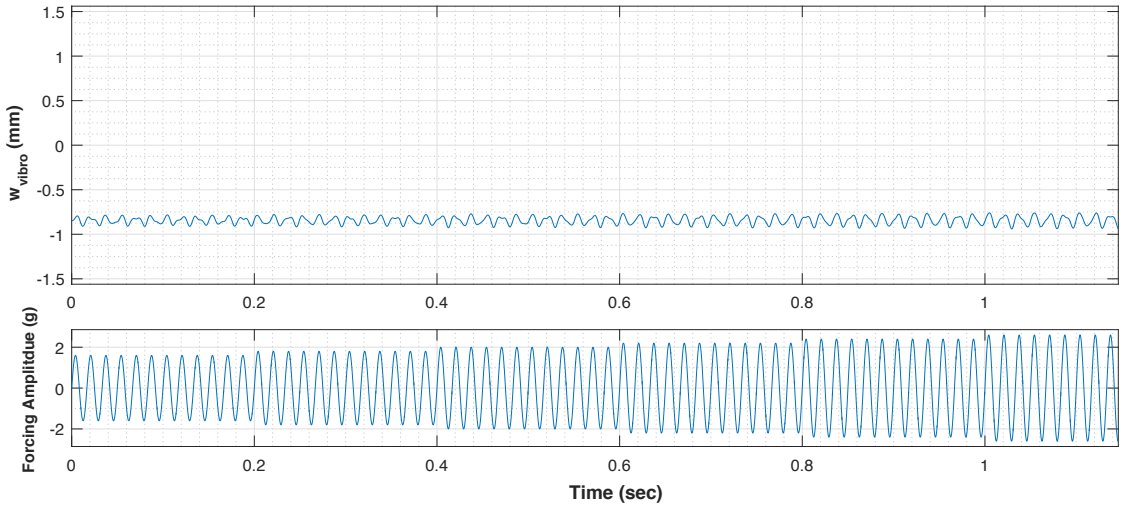

Figure 5.8: Response of the NCF model for 1.6 g- to 2.6 g-60 Hz harmonic loading.

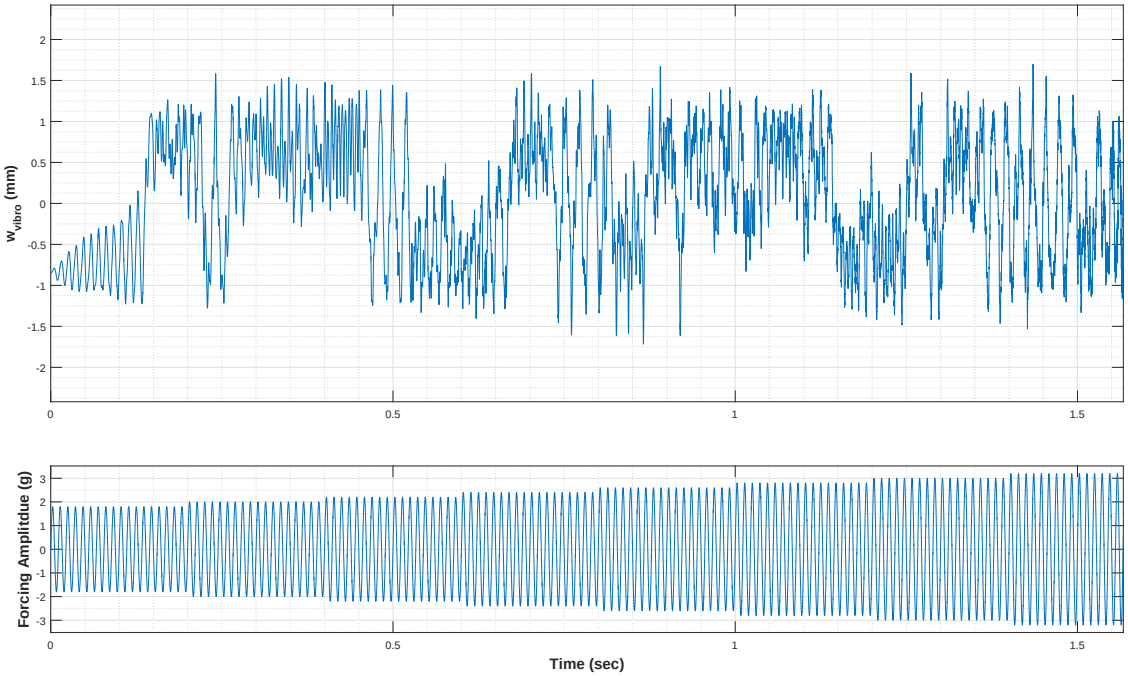

Figure 5.9: Response of the NCF model for 1.8 g- to 3.2 g-90 Hz harmonic loading.

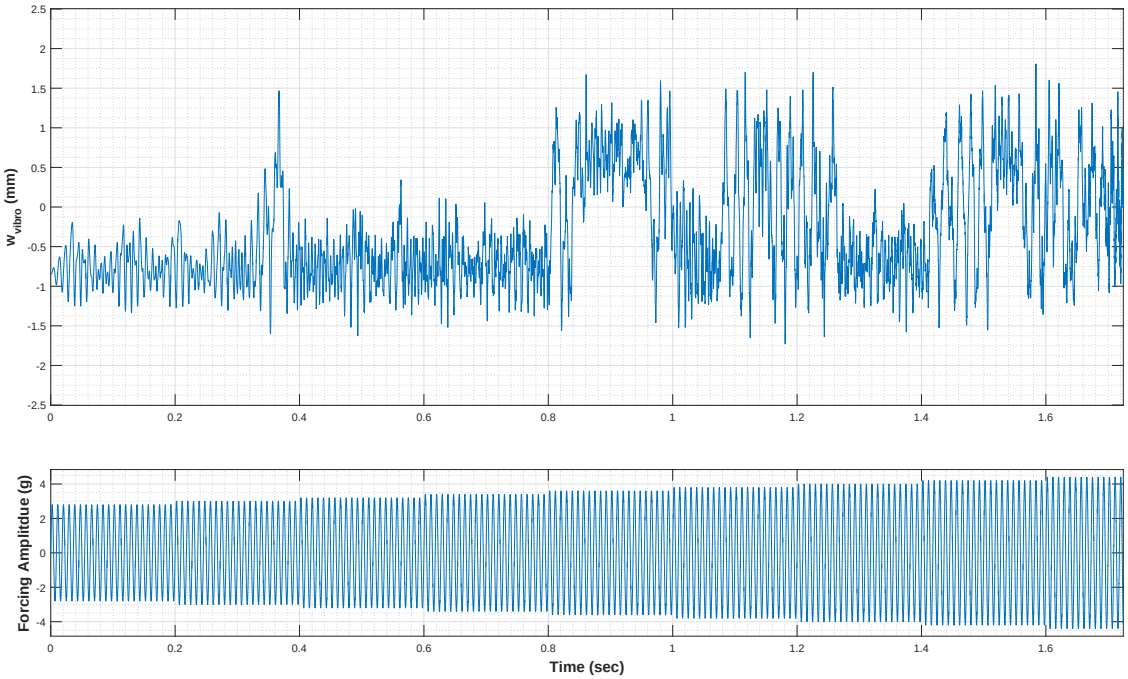

Figure 5.10: Response of the NCF model for 2.8 g- to 4.4 g-110 Hz harmonic loading.

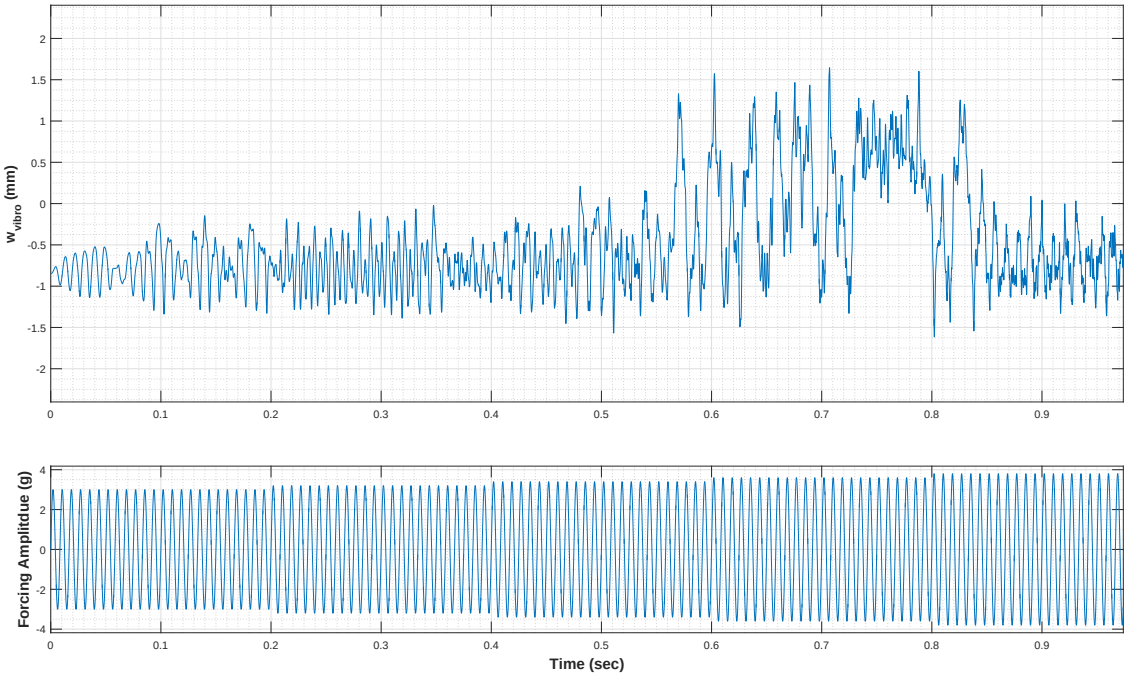

Figure 5.11: Response of the NCF model for 3 g- to 3.8 g-120 Hz harmonic loading.

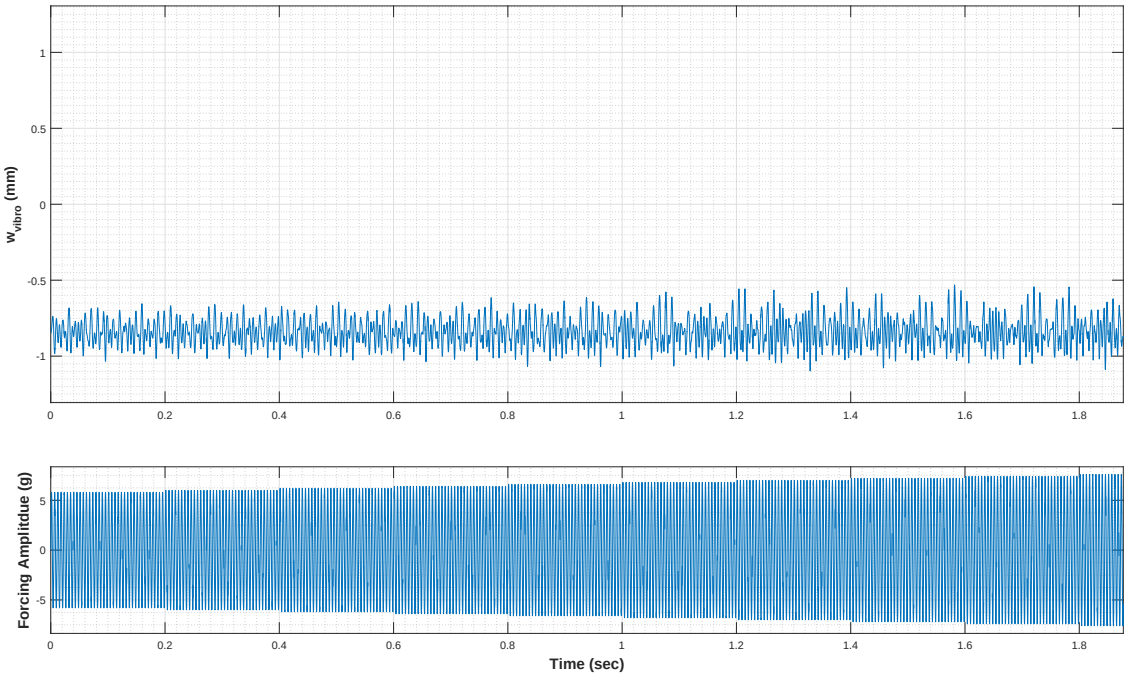

Figure 5.12: Response of the NCF model for 5.8 g- to 7.6 g-180 Hz harmonic loading.

in Figure 5.12 (the 180 Hz case) was conducted to examine the boundary formed between 165 Hz and 195 Hz shown in Figure 5.7. The model predicted no snap-through around that region.

5.4 Model: forcing frequency-sweep analyses

In this section, the forcing frequency-sweep cases were simulated. Compared to the frequency-sweep experiment, the simulation had additional forcing amplitude cases between the amplitudes used for the experiment to investigate the regions between the boundaries found from the experiment. Figures 5.13 to 5.23 illustrate the transverse displacement of the vib-point of the NCF model (w_{vibro}) responding to the changes in forcing frequency at the forcing amplitudes: 2, 2.5, 3, 3.5, 4, 4.5, 5, 5.5, 6, 6.5, and 7 g.

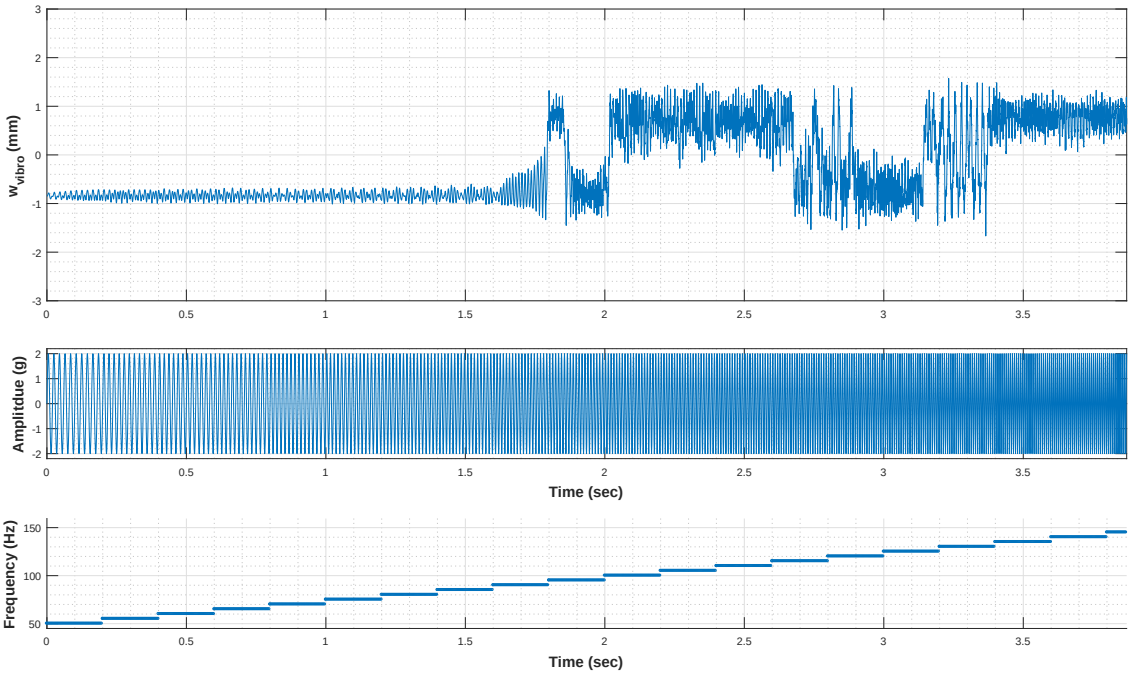

Figure 5.13: Response of the NCF model for 2 g-50 Hz to -160 Hz harmonic loading.

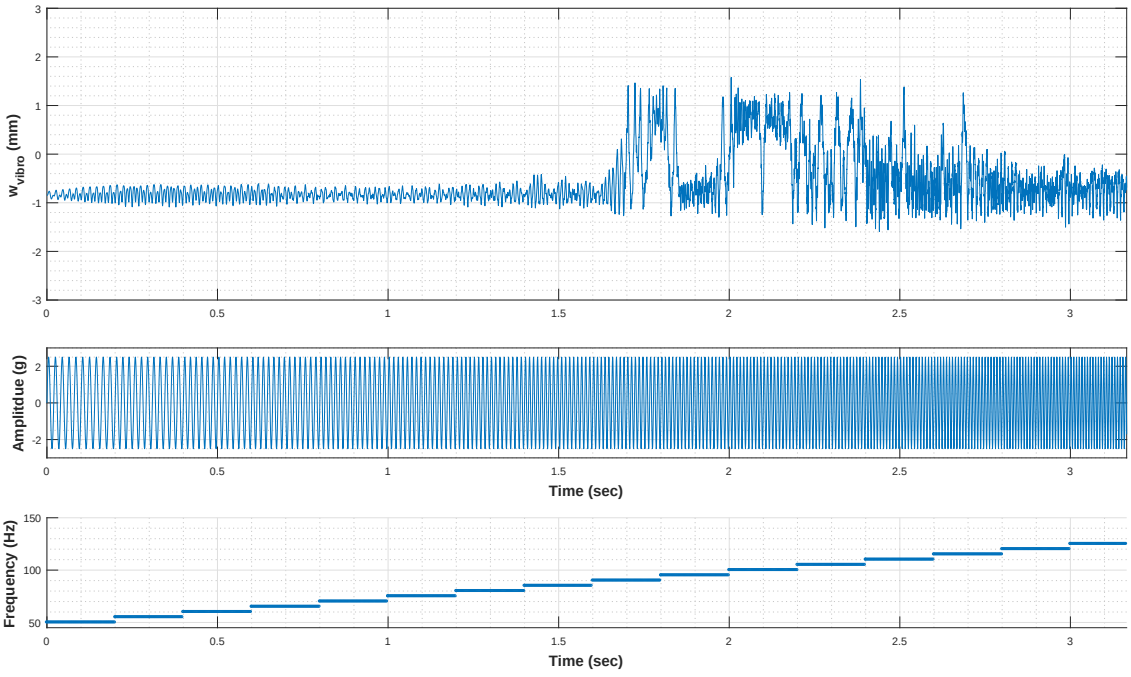

Figure 5.14: Response of the NCF model for 2.5 g-50 Hz to -135 Hz harmonic loading.

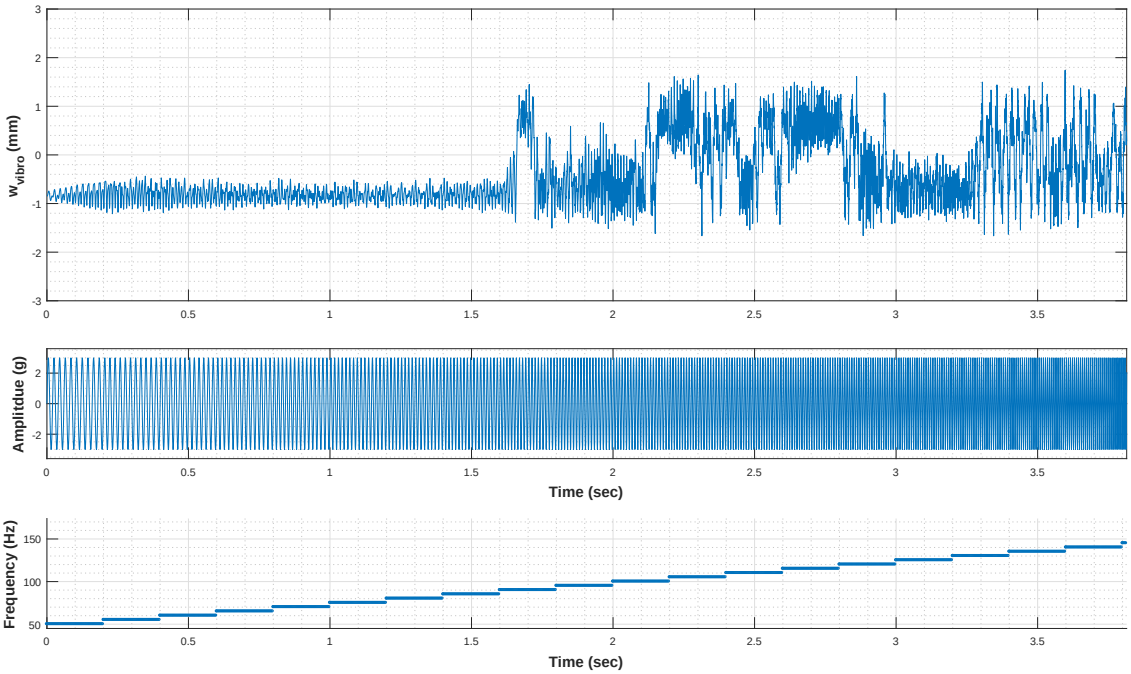

Figure 5.15: Response of the NCF model for 3 g-50 Hz to -155 Hz harmonic loading.

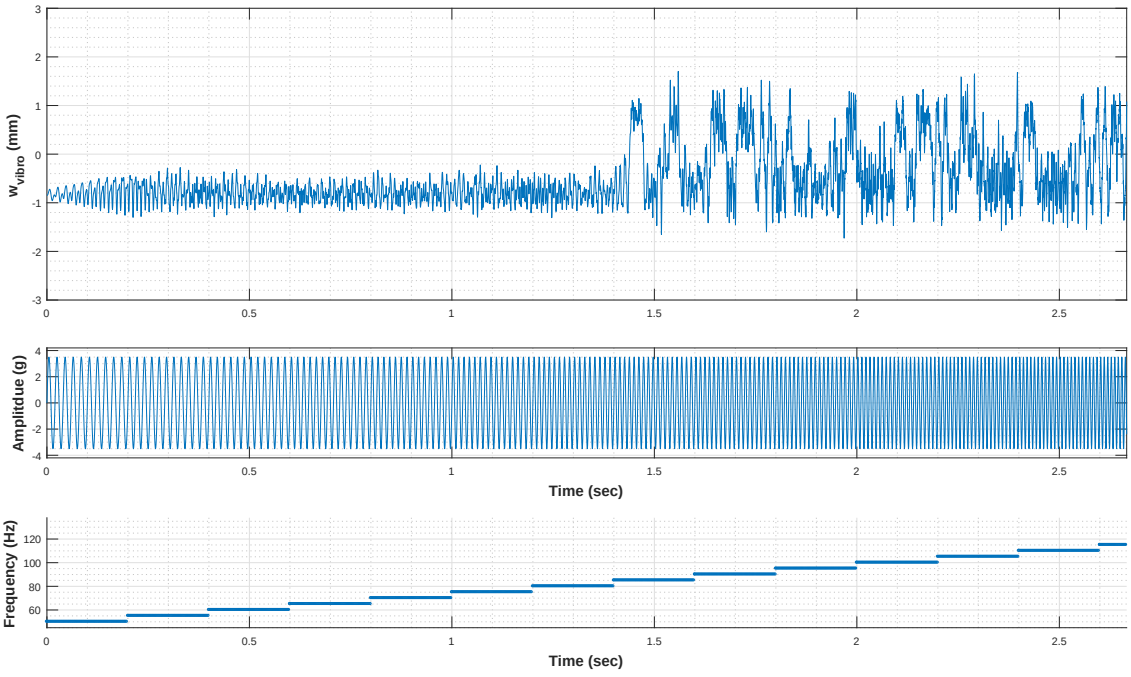

Figure 5.16: Response of the NCF model for 3.5 g-50 Hz to -130 Hz harmonic loading.

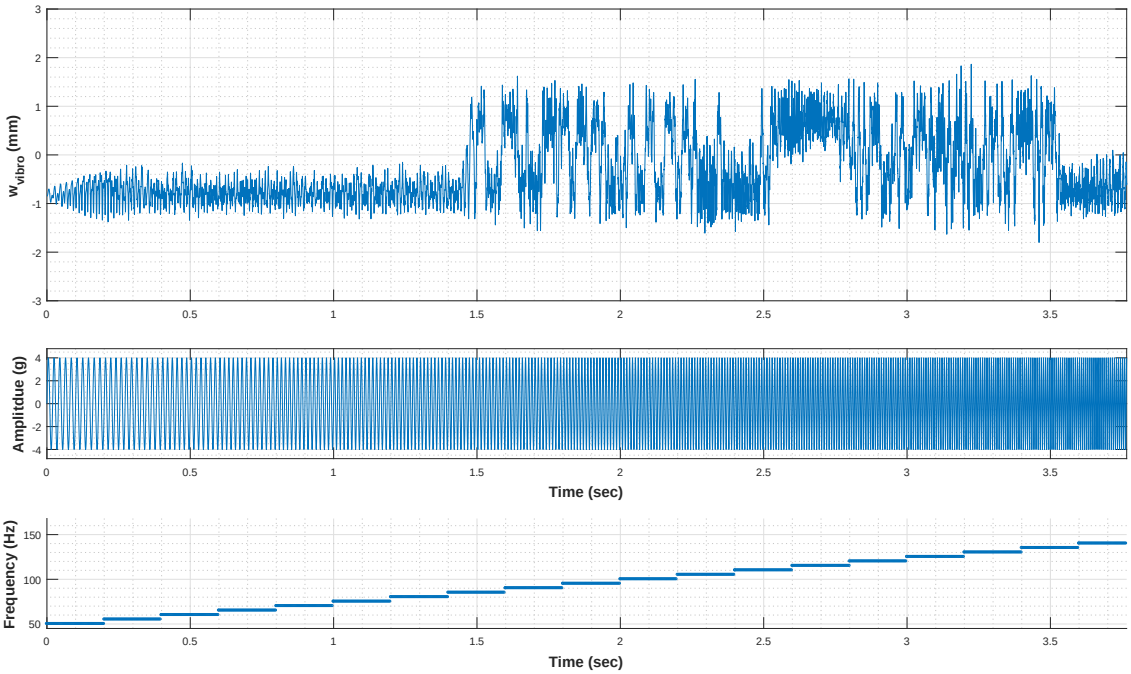

Figure 5.17: Response of the NCF model for 4 g-50 Hz to -150 Hz harmonic loading.

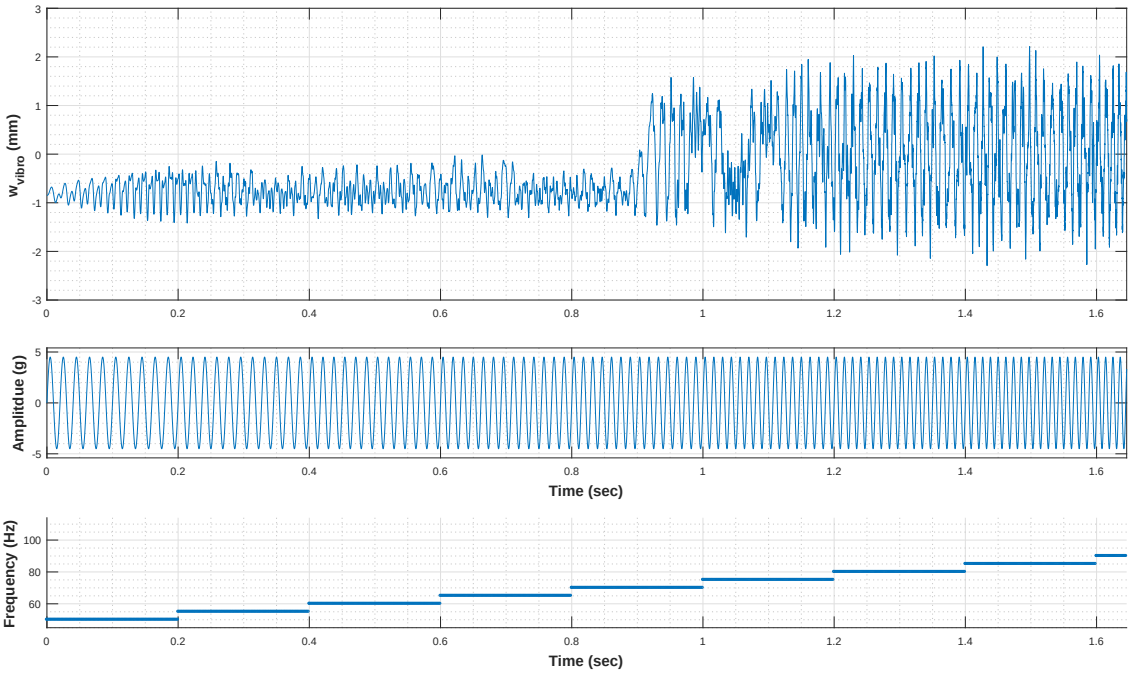

Figure 5.18: Response of the NCF model for 4.5 g-50 Hz to -65 Hz harmonic loading.

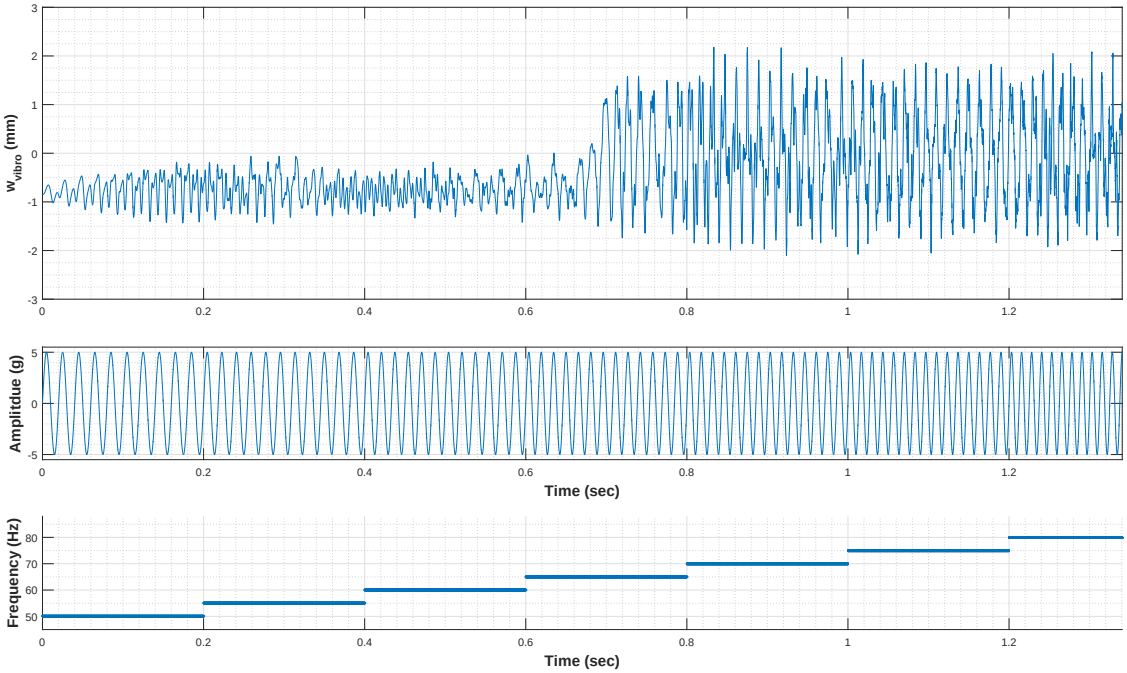

Figure 5.19: Response of the NCF model for 5 g-50 Hz to -80 Hz harmonic loading.

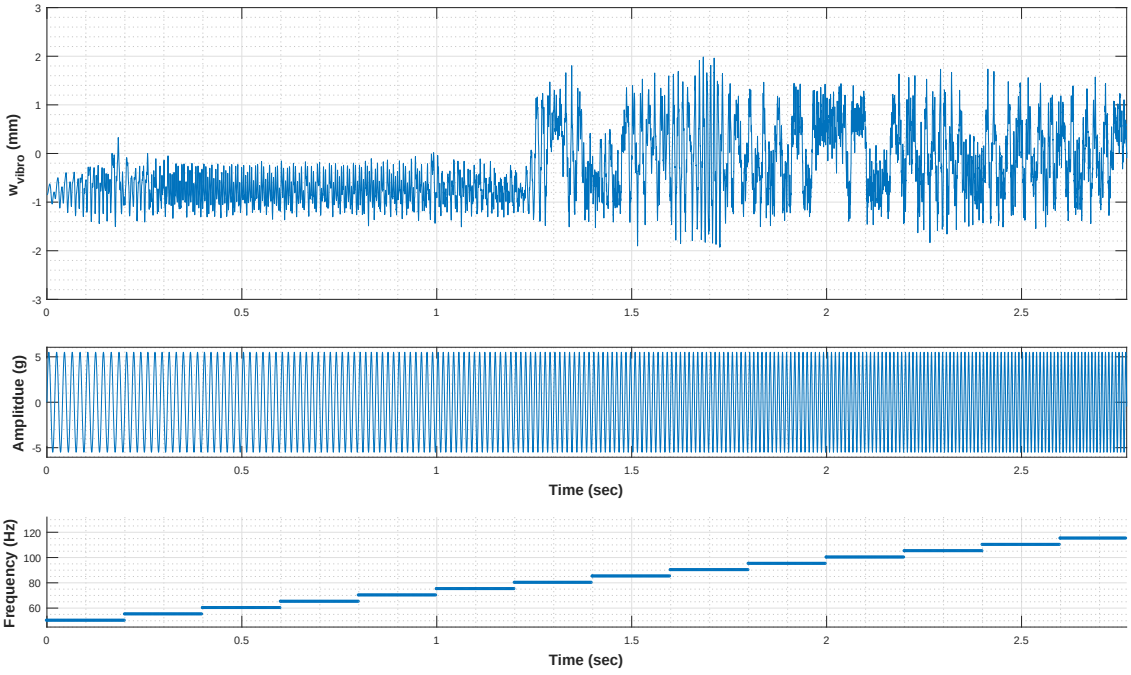

Figure 5.20: Response of the NCF model for 5.5 g-50 Hz to -100 Hz harmonic loading.

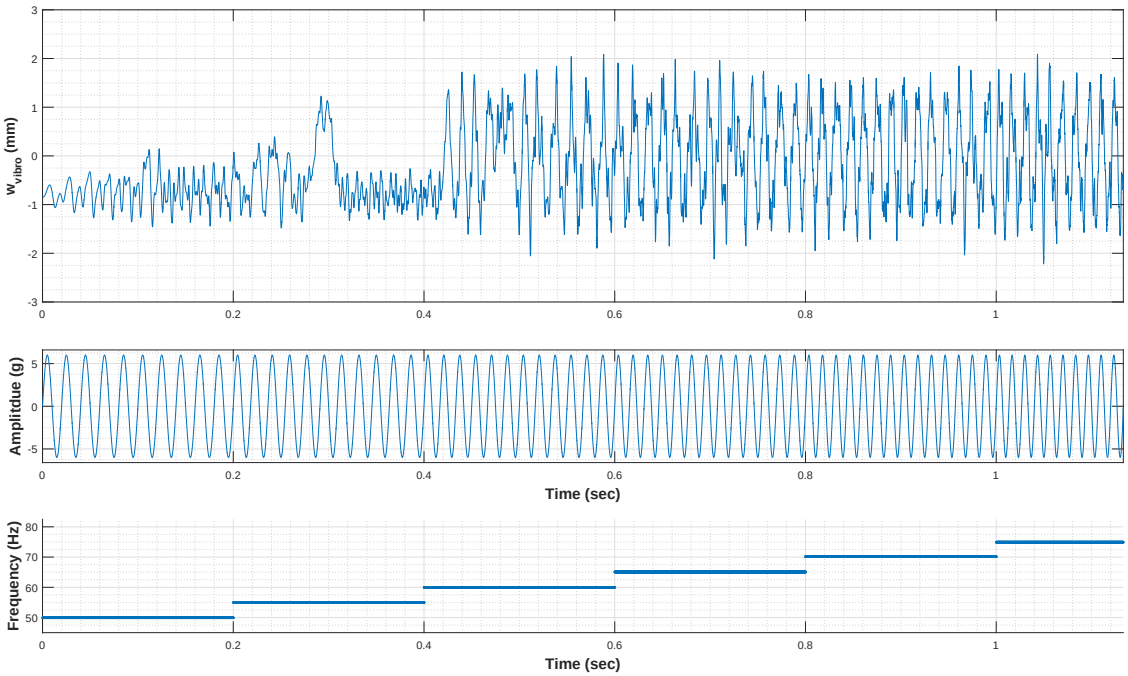

Figure 5.21: Response of the NCF model for 6 g-50 Hz to -75 Hz harmonic loading.

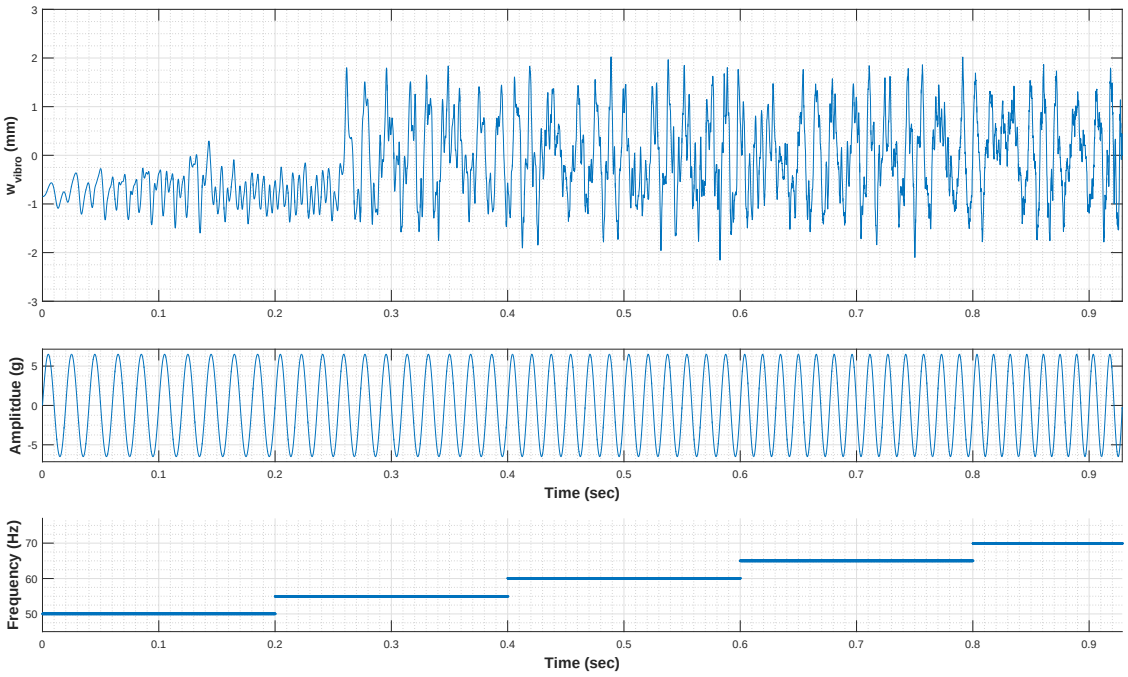

Figure 5.22: Response of the NCF model for 6.5 g-50 Hz to -70 Hz harmonic loading.

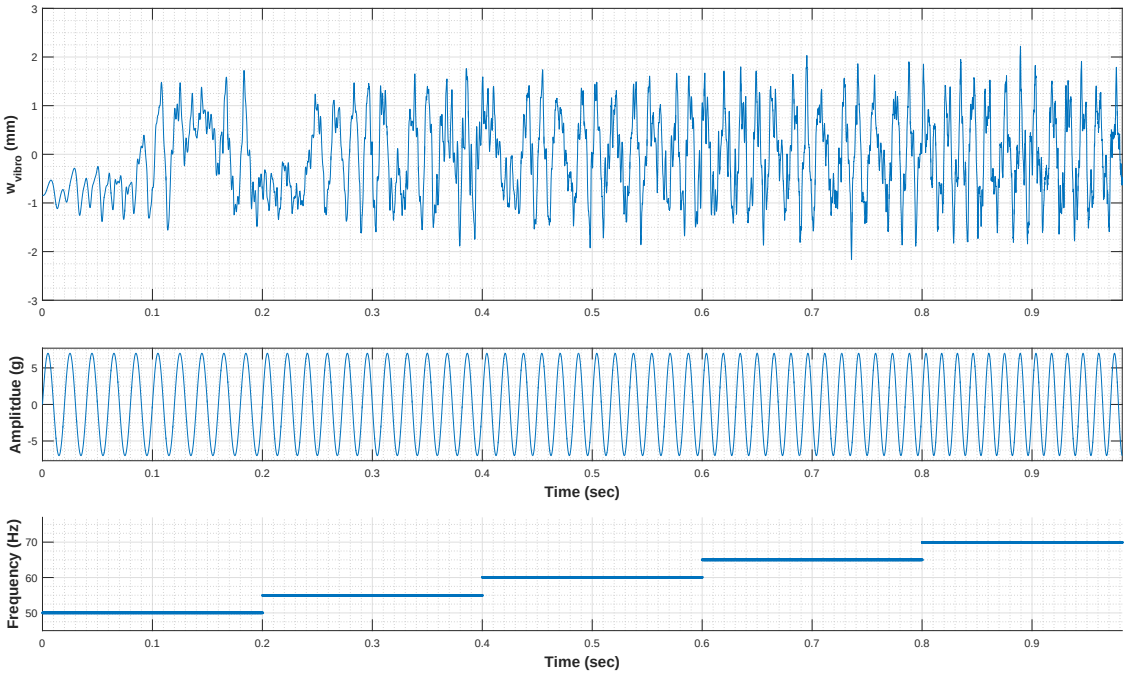

Figure 5.23: Response of the NCF model for 7 g-50 Hz to -70 Hz harmonic loading.

For the 2 g case (Figure 5.13), the chaotic snap-through was observed between 90 Hz and 95 Hz. This region matched the experimental result. However, the model predicted another region between 115 and 130 Hz which was not found from the experiment. A similar phenomenon was observed from the 2.5 g case (Figure 5.14). The chaotic snap-through was observed between 90 and 110 Hz. Another region was observed at 135 Hz. The 3 g case (Figure 5.15) exhibited the three chaotic snap-through regions at 90 Hz, 100 to 120 Hz, and 130 to 155 Hz. Considering the experimental snap-through regions at 3 g were located at 85 to 90 Hz and 105 to 110 Hz, the predicted regions are larger and include the experimental ones. For the 3.5 g case (Figure 5.16), the chaotic snap-through was observed at 85 to 120 Hz and 130 Hz. The first region showed a good agreement with the assumed boundary between 3 and 4 g shown in Figure 5.7. The 4 g case (Figure 5.17) exhibited the three chaotic snap-through regions at 85 to 110 Hz, 120 to 135 Hz, and 145 to 150 Hz. The first range and the beginning of the second range matched the experimental region but the other ranges were

not found from the experimental results. For the 4.5 and 5 g cases (Figures 5.18 and 5.19), the snap-through began at 70 and 65 Hz, respectively but the experimental boundaries were located at larger frequencies, 80 and 75 (assumed) Hz, respectively. The 5.5 g case (Figure 5.20) found the snap-through region between 80 and 100 Hz, which matched the experimental results. For the 6, 6.5, and 7 g cases (Figures 5.21, 5.22, and 5.23), the chaotic snap-through began at 60, 55, and 50 Hz, respectively, but the experimental boundaries were positioned at larger frequencies, 73, 67 (assumed), and 60 Hz, respectively.

5.5 Comparison of snap-through boundaries

The snap-through points observed from the aforementioned simulations were collected and were marked in the HFP space with the snap-through boundary of the post-buckled AFRL plate as illustrated in Figures 5.24 to 5.26.

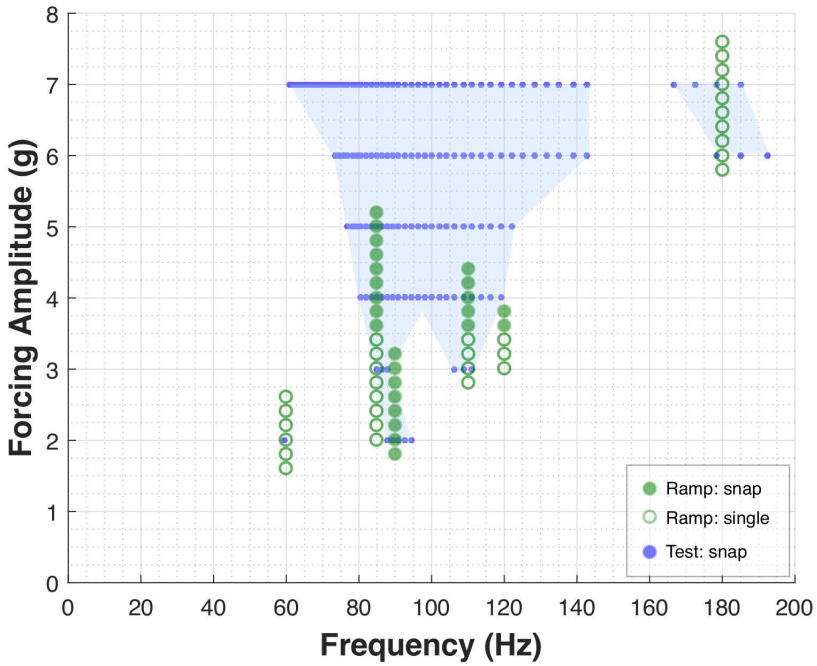

Figure 5.24: Superposition of the snap-through points observed from the forcing amplitude-ramp simulations and the experimental snap-through boundaries.

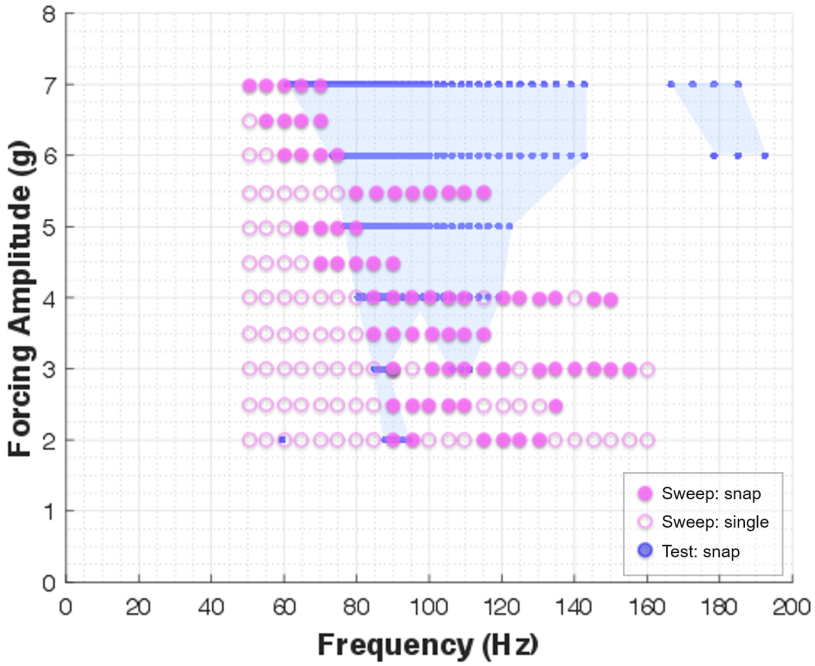

Figure 5.25: Superposition of the snap-through points observed from the forcing frequency-sweep simulations and the experimental snap-through boundaries.

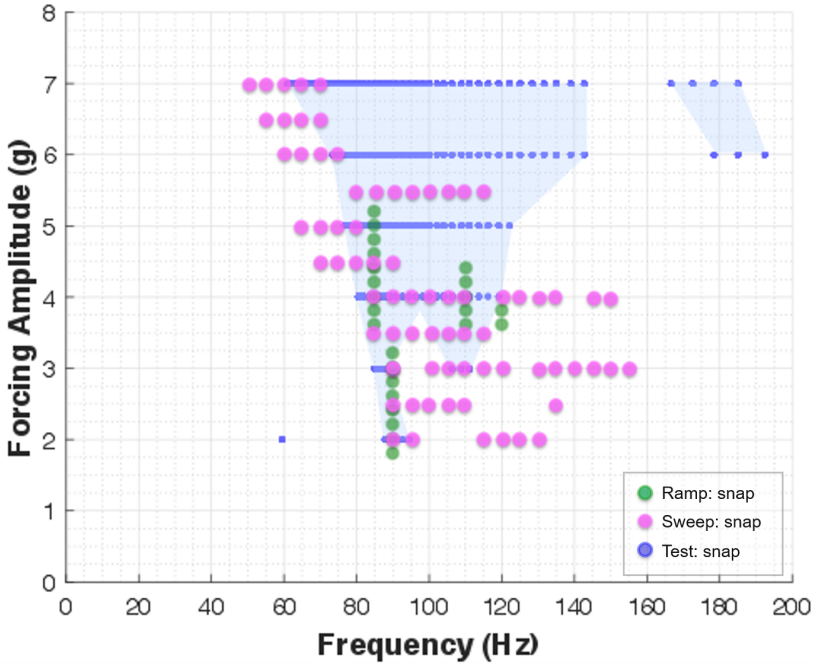

Figure 5.26: Comparison of the experimental and modeled snap-through boundaries.

In the legends of those figures, 'Ramp: snap' and 'Ramp: single' indicate the snap-through and the single-well response observed from the forcing amplitude-ramp simulations, respectively. Similarly, 'Sweep: snap' and 'Sweep: single' represent the snap-through and the single-well response observed from the forcing frequency-sweep simulations, respectively. 'Test: snap' indicates the snap-through observed from the forcing frequency-sweep experiments.

It was observed from Figure 5.26 that while both boundaries showed a good agreement at some regions, the NCF model formed larger bottom and left-side boundaries in the HFP space compared to the experimental boundaries. It is suspected that this discrepancy could be attributed to the following reasons:

- as discussed in Chapter 4, the damping effects were not included in the model,
- although the material properties of the AFRL plate were tested and were validated as described in Chapter 3, there were still possibilities that the predicted material properties did not exactly match the ones of the AFRL plate, and
- as observed from the snap-through boundaries of the post-buckled UW plate (discussed in Chapter 3), coexisting responses could be present between the snap-through boundaries in the HFP space and consequently the extreme sensitivity to the initial conditions (i.e., the states which were found at the end of each forcing amplitude or frequency step and were used as the initial conditions for the next amplitude or frequency step during the forcing amplitude-ramp or frequency-sweep tests or simulations) possibly caused the model to predict chaotic snap-through in the regions where chaotic snap-through coexisted with a single-well response while the experimental result exhibited a single-well response and vice versa.

The upper part of the experimental boundary could not be investigated by the model since the mode failed to converge at those areas during the forcing amplitude-ramp and frequency-sweep simulations due to the high-frequency twisting deformation. In addition, high compu-

tational cost of the CLPT model using nonconforming elements also restricted the attempt to conduct more simulations than presented in this work. To obtain the simulation results demonstrated in this chapter and investigate the modeled snap-through boundaries shown in Figures 5.24 to 5.26, the three personal computer processors and seven supercomputer nodes ran the model for a month. Although the model exhibited the sophisticated simulation results and successfully captured the complicated cases such as the irregularly-buckled shape and the twisting deformation, such a high computation cost could be impractical for many research and industrial projects.

The above-mentioned issues about modeling the dynamic response of post-buckled thin laminated composite plates will be further investigated in the future research, which is outlined in Chapter 6.

Chapter 6

SUMMARY AND FUTURE WORK

6.1 Summary

In this work, snap-through and the associated nonlinear dynamics of post-buckled composite plates were experimentally and computationally investigated.

For the experimental components, the processes for fabrication of composite specimens and for validation of their material properties were first introduced. The general characteristics and related nonlinear dynamics of snap-through boundaries were then examined through experiments conducted in the Structural Vibrations Lab in the University of Washington. As an example of the nonlinear dynamic phenomena observed from the experimental data, the distinct boundaries formed in the harmonic forcing parameter (HFP) space by collecting the thresholds for the initiation and termination of snap-through demonstrated the existence of various types of coexisting responses between the boundaries. To extend the findings, the digital image correlation (DIC) technique was employed at the Air Force Research Laboratory (AFRL) to measure the full-field buckled and deflected shapes of a post-buckled plate. The buckled shape reconstructed based on the full-field measurement provided the comprehensive data required for the accurate input geometry used in the modeling. The diverse mode shapes during snap-through and high-frequency twisting deformation due to the irregularly-buckled shape of the specimen were observed from the DIC data. The snap-through boundaries of the post-buckled plate were found using the experimental data collected by the vibrometer during the frequency-sweep tests.

For the modeling components, the nonlinear equations of motion and finite element model (FEM) were derived using the classical laminated plate theory (CLPT) and von Kármán strains. Conforming and nonconforming elements and associated Hermite interpolation functions were introduced to develop the FEM. The nonlinear equilibrium paths of the model using the conforming elements (named *the CF model*) were found using a linearized arc-length method, a semi-direct approach for singular point identification, and a branch-switching technique. The dynamic analysis results of the CF model revealed the limitation of models consisting of rectangular conforming elements and consequently the CF model was deemed to be incapable of reproducing the irregularly-buckled and deflected shapes of the post-buckled plate specimen used at AFRL (named *the AFRL plate*). To overcome this inherent problem of the CF model, another model composed of nonconforming elements (named *the NCF model*) was proposed. The NCF model successfully replicated the buckled shape of the AFRL plate and exhibited the nonlinear dynamic behaviors comparable with the dynamic responses observed from the full-field measurement including twisting deformation.

The snap-through boundaries established based on the simulation results of the NCF model showed a good agreement at some regions with the experimentally-found boundaries but extended to the areas in the HFP space where snap-through was not observed in the experiments. It is suspected that this discrepancy could be attributed to: (i) the fact that damping effects were not considered in the model, (ii) the probable discrepancy between the actual and predicted material properties, and (iii) the coexisting responses between the snap-though boundaries and consequent extreme sensitivity to the initial conditions in the HFP space. To validate the contribution of the first item, new models which include damping effects will be developed and be simulated in future works. However, the investigation of the third item would require collection and analysis of a large amount of experimental and computational data at each point in the HFP space, whose practical feasibility could remain uncertain for future works.

The NCF model based on CLPT demonstrated its capability of modeling sophisticated specimens like the irregularly-buckled plate and capturing their complicated responses such

as the twisting deformation and the various mode shapes during snap-through events. However, considerable computational costs required for its simulation as shown in this work would restrict the practical applications of this model, which provided the strong motivation for developing more efficient models for future works.

6.2 Future work

6.2.1 Shear deformation theories and layerwise theories

As briefly discussed in Chapter 2, various types of theories have been developed and been discussed in the literature to model laminated composite plates. In this section, some laminated plate theories are introduced based on Reddy's description in [25].

The shear deformation theories (SDT) relax the normality restriction of CLPT (i.e., the transverse plane remains straight and normal to the midplane after deformation) by including shear deformation. For example, the first-order shear deformation theory (FSDT) assumes constant transverse shear strain while the third-order shear deformation theory (TSDT) assumes quadratic variation of transverse shear strain and vanishing of transverse shear stress on the top and bottom of plates. Based on the coordinate system and plate dimensions shown in Figure 2.1, the displacement fields of FSDT and TSDT are introduced in Equations (6.1) and (6.2), respectively.

$$u = u_0 + z\phi_x, \quad v = v_0 + z\phi_y, \quad w = w_0, \tag{6.1}$$

in which ϕ_x and ϕ_y are rotations about the y and x axes, respectively.

$$\begin{aligned} u &= u_0 + z\phi_x + z^3\Big(-\frac{4}{3h^2}\Big)\Big(\phi_x + \frac{\partial w_0}{\partial x}\Big), \\ v &= v_0 + z\phi_y + z^3\Big(-\frac{4}{3h^2}\Big)\Big(\phi_y + \frac{\partial w_0}{\partial y}\Big), \\ w &= w_0. \end{aligned} \tag{6.2}$$

Other higher-order SDTs such as the second-order SDT, the trigonometric SDT, the hyperbolic SDT, and many others also exist [10].

While CLPT and SDT are categorized as the equivalent single layer (ESL) theories, layerwise theories (LTs) are classified as the 3-D elasticity theories, in which each layer is modeled as a 3-D solid. In LTs, the displacement components are continuous along the thickness of plates whereas their derivatives can be discontinuous along the thickness. LTs can be divided into the full and partial LTs. The former use layerwise expansion for all displacement components (u, v, and w) while the latter use the expansion only for the in-plane displacement components (u and v).

In future works, the above-mentioned theories will be explored and their performance will be compared to the experimental data and modeling results presented in this work to find optimum theories to model the snap-through behaviors of post-buckled composite plates.

6.2.2 Delamination growth in laminated composite plates due to dynamic snap-through

This work concentrated on characterizing and modeling nonlinear dynamic behaviors of particular interest in the snap-through of post-buckled composite plates. Naturally, the implication of these phenomena on composite structures, especially in terms of the impact on their structural safety, will be a central research topic of future works.

As discussed in Chapter 1, delamination is a common and important failure mode in laminated composite structures. Large-amplitude deformations and in-plane compressive loading generated during snap-through may accelerate delamination growth in those structures, which possibly entails considerable risks associated with the structural integrity.

In future works, the impact of the mode I, mode II, and mixed mode I/II fatigue loading induced by snap-through on delamination growth will be experimentally and computationally investigated. The delamination growth will be detected and be measured using a 3-D computed tomography (CT) scan system as shown in Figure 6.1.

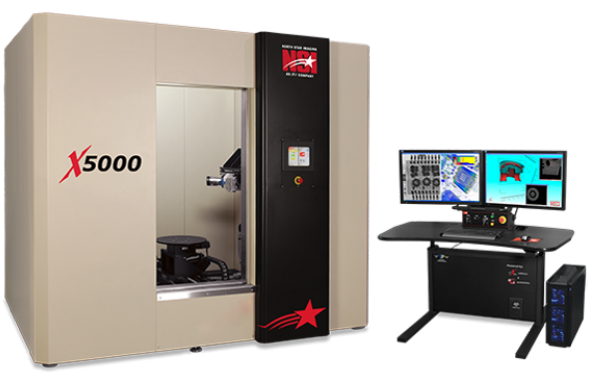

(a) 3-D CT scan system NSI X5000.

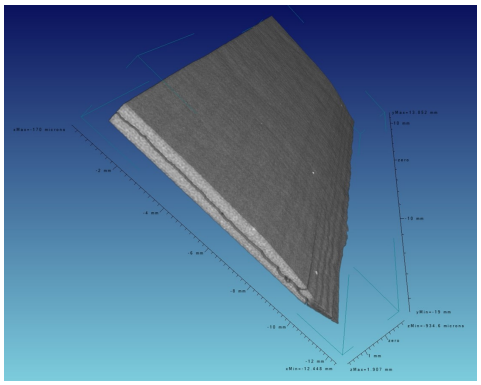

(b) 3-D CT scan of delamination in a composite beam.

Figure 6.1: 3-D CT scan system and scanned delamination.

6.2.3 Nonlinear reduced-order modeling

In this work, high computational cost of the NCF model was identified as a serious hindrance to the practical applications of the model. To address this issue, the nonlinear reduced-order model (ROM) will be employed in future works. ROMs enable a few degrees of freedom of structures to capture the nonlinear behaviors of the structures and can be constructed by the proper orthogonal decomposition and nonlinear normal modes methods [29]. The applications of ROMs were extensively discussed in [65, 66, 67, 68, 69].

In future works, a ROM based on CLPT will be built using the experimental data presented in this work and will be compared to the simulation results of the NCF model to validate the effectiveness of ROMs. In addition, ROMs constructed using SDTs and LTs will be used to investigate the impact of the fatigue loading induced by snap-through on delamination growth since the theories consider the interlaminar stresses (τ_{xz}, τ_{yz}, σ_{zz}) which are responsible for delamination growth but are disregarded in CLPT.

Bibliography

[1] K. D. Murphy, L. N. Virgin, and S. A. Rizzi. Experimental snap-through boundaries for acoustically excited thermally buckled plates. *Experimental mechanics*, 36(4):312–317, 1996.

[2] A. Przekop, S. A. Rizzi, and K. A. Sweitzer. An investigation of high-cycle fatigue models for metallic structures exhibiting snap-through response. *International Journal of Fatigue*, 30(9):1579–1598, 2008.

[3] R. Wiebe. *Nonlinear dynamics of discrete and continuous mechanical systems with snap-through instabilities*. PhD thesis, Duke University, 2012.

[4] Y. Chandra, R. Wiebe, I. Stanciulescu, L. N. Virgin, S. M. Spottswood, and T. G. Eason. Characterizing dynamic transitions associated with snap-through of clamped shallow arches. *Journal of Sound and Vibration,*, 332(22):5837–5855, 2013.

[5] R. Wiebe, L. N. Virgin, I. Stanciulescu, S. M. Spottswood, and T. G. Eason. Characterizing dynamic transitions associated with snap-through: a discrete system. *Journal of Computational and Nonlinear Dynamics*, 8(1):011010, 2013.

[6] R. Wiebe and L. N. Virgin. A harmonic balance approximation of dynamic snap-through boundaries in a single-degree-of-freedom structure. In *Proceedings of Proceedings of the ASME 2013 International Design Engineering Technical Conferences and Computers and Information in Engineering Conference, Oregon, USA*, 2013.

[7] R. Wiebe and S. M. Spottswood. Co-existing responses and stochastic resonance in post-buckled structures: a combined numerical and experimental study. *Journal of Sound and Vibration*, 333(19):4682–4694, 2014.

[8] J. Hale. Boeing 787 from the ground up. *AERO magazine*, Q406:16–23, 2006.

[9] *http://www.stablwall.com/civil-commercial-infrastructure/*. StablWall, 2017.

[10] R. Khandan, S. Noroozi, P. Sewell, and J. Vinney. The development of laminated composite plate theories: a review. *Journal of Materials Science*, 47(16):5901–5910, 2012.

[11] R. F. Gibson. *Principles of Composite Material Mechanics, Third Edition*. Taylor & Francis, Boca Raton, USA, 2012.

[12] M. Zoghi. *The International Handbook of FRP Composites in Civil Engineering*. CRC Press, Boca Raton, USA, 2014.

[13] A. S. Kaddour, M. J. Hinton, P. A. Smith, and S. Li. The background to the third world-wide failure exercise. *Journal of Composite Materials*, 47(20-21):2417–2426, 2013.

[14] William Ko. Thermal buckling analysis of rectangular panels subjected to humped temperature profile heating, NASA/TP-2004-212041. Technical report, 2004.

[15] K. D. Murphy and D. Ferreira. Thermal buckling of rectangular plates. *International Journal of Solids and Structures*, 38(22):3979–3994, 2001.

[16] T. J. Beberniss, S. M. Spottswood, D. A. Ehrhardt, and R. A. Perez. Nonlinear response of a thin panel subjected to a shockwave impingement. In *Proceedings of the 35th IMAC, Society for Experimental Mechanics, Orange County, USA*, 2017.

[17] R. A. Perez, S. M. Spottswood, and T. J. Beberniss. Nonlinear response prediction of a buckled panel in a supersonic flow. In *Proceedings of the 35th IMAC, Society for Experimental Mechanics, Orange County, USA*, 2017.

[18] H. Chai, C. D. Babcock, and W. G. Knauss. One dimensional modelling of failure in laminated plates by delamination buckling. *International Journal of Solids and Structures*, 17(11):1069–1083, 1981.

[19] Y. Zou, L. Tong, and G. P. Steven. Vibration-based model-dependent damage delamination identification and health monitoring for composite structures - a review. *Journal of Sound and Vibration*, 230(2):357–378, 2000.

[20] S. H. Strogatz. *Nonlinear Dynamics and Chaos: with Applications to Physics, Biology, Chemistry, and Engineering, Second Edition*. Westview Press, Boulder, USA, 2015.

[21] S. Timoshenko and S. Woinowsky-Krieger. *Theory of Plates and Shells, Second Edition*. McGraw-Hill, New York, USA, 1959.

[22] J. M. Whitney. *Structural Analysis of Laminated Anisotropic Plates*. Technomic Pub. Co., Lancaster, USA, 1987.

[23] A. W. Leissa. *Vibrations of Plates*. National Aeronautics and Space Administration, Washington, D.C., USA, 1969.

[24] C.-Y. Chia. *Nonlinear Analysis of Plates*. McGraw-Hill, New York, USA, 1980.

[25] J. N. Reddy. *Mechanics of laminated composite plates and shells: Theory and Analysis, Second Edition*. CRC Press, Boca Raton, USA, 2004.

[26] A. B. Strong. *Fundamentals of Composites Manufacturing: Materials, Methods and Applications, Second Edition*. Society of Manufacturing Engineers, Dearborn, USA, 2008.

[27] M. H. Datoo. *Mechanics of Fibrous Composites.* Elsevier Science Pub. Co., New York, USA, 1991.

[28] J. N. Reddy. *Theory and Analysis of Elastic Plates and Shells.* Taylor & Francis, Philadelphia, USA, 1999.

[29] M. Amabili. *Nonlinear Vibrations and Stability of Shells and Plates.* Cambridge University Press, New York, USA, 2008.

[30] M. Petyt. *Introduction to Finite Element Vibration Analysis, Second Edition.* Cambridge University Press, New York, USA, 2010.

[31] J. N. Reddy. *An Introduction to the Finite Element Method, Third Edition.* McGraw-Hil, New York, USA, 2006.

[32] M. E. Tuttle. *Structural Analysis of Polymeric Composite Materials, Second Edition.* CRC Press, Boca Raton, USA, 2013.

[33] J. N. Reddy. *An Introduction to Nonlinear Finite Element Analysis.* Oxford University Press, New York, USA, 2004.

[34] J. N. Reddy. *An Introduction to Nonlinear Finite Element Analysis: with Applications to Heat Transfer, Fluid Mechanics, and Solid Mechanics, Second Edition.* Oxford University Press, New York, USA, 2015.

[35] O. C. Zienkiewicz, R. L. Taylor, and J. Z. Zhu. *The Finite Element Method: its Basis and Fundamentals, Seventh Edition.* Butterworth-Heinemann, Waltham, USA, 2013.

[36] G. Dhatt, G. Touzot, and E. Lefrancois. *Finite Element Method.* Wiley, Hoboken, USA, 2012.

[37] Z. Penava, D.S. Penava, and Z. Knezic. Determination of the elastic constants of plain woven fabrics by a tensile test in various directions. *Fibres & Textiles in Eastern Europe*, 22(2):57–63, 2014.

[38] S. Kobayashi, S. Ogihara, and N. Takeda. Experimental characterization of the effects of stacking sequence on the transverse crack behavior in quasi-isotropic interleaved CFRP laminates. *Advanced Composite Materials*, 9(3):241–251, 2000.

[39] S. Kobayashi, S. Ogihara, and N. Takeda. Experimental and analytical characterization of matrix cracking in quasi-isotropic CFRP laminates with interlaminar-toughened layers under fatigue loading. *Science and Engineering of Composite Materials*, 9(2):45–54, 2000.

[40] N. Takeda, L. N. McCartney, and S. Ogihara. The application of ply-refinement technique to the analysis of microscopic deformation in interlaminar toughened laminates with transverse cracks. *Composites Science and Technology*, 60(2):231–240, 2000.

[41] *MATLAB R2015b*. MathWorks, Inc., 2015.

[42] L. N. Virgin, J. J. Waite, and R. Wiebe. Co-existing responses in a harmonically-excited nonlinear structural system. In *Proceedings of the 32nd IMAC, Society for Experimental Mechanics, Orlando, USA*, 2014.

[43] M. Grediac and F. Hild. *Full-Field Measurements and Identification in Solid Mechanics*. Wiley, Hoboken , USA, 2012.

[44] J. M. T. Thompson and H. B. Stewart. *Nonlinear Dynamics and Chaos, Second Edition*. Wiley, New York, USA, 2002.

[45] M. A. S. Masoum and E. F. Fuchs. *Power Quality in Power Systems and Electrical Machines, Second Edition*. Academic Press, Waltham, USA, 2015.

[46] K. Worden and G. R. Tomlinson. *Nonlinearity in Structural Dynamics: Detection, Identification and Modelling*. Institute of Physics, Philadelphia, USA, 2001.

[47] F. K. Bogner, R. L. Fox, and Jr. L. A. Schmidt. The generation of inter-element-compatible stiffness and mass matrices by the use of interpolation formulas. In *Proceedings of the Conference on Matrix Methods in Structural Mechanics, AFFDL-TR-66-80, Dayton, USA*, 1965.

[48] R. J. Melosh. Basis of derivation of matrices for the direct stiffness method. *AIAA Journal*, 1(7):1631–1637, 1963.

[49] O. C. Zienkiewicz and Y. K. Cheung. The finite element model for analysis of elastic isotropic and orthotropic slabs. In *Proceeding of the institute of civil engineers, London, UK*, 1964.

[50] J. L. Meek and S. Loganathan. Large displacement analysis of space-frame structures. *Computer Methods in Applied Mechanics and Engineering*, 72(1):57–75, 1989.

[51] W. F. Lam and C. T. Morley. Arc-length method for passing limit points in structural calculation. *Journal of Structural Enginering*, 118(1):169–185, 1992.

[52] Y. T. Feng, D. Peric, and D. R. J. Owen. A new criterion for determination of initial loading parameter in arc-length methods. *Computer and Structures*, 58(3):479–485, 1996.

[53] J. Shi and M. A. Crisfield. Combining arc-length control and line searches in path following. *Commnications in Numerical Methods in Engineering*, 11(10):793–803, 1995.

[54] H.-B. Hellweg and M. A. Crisfield. A new arc-length method for handling sharp snap-backs. *Computer and Structures*, 66(5):704–709, 1998.

[55] M. Ritto-Correa and D. Camotim. On the arc-length and other quadratic control methods: established, less known and new implementation procedures. *Computer and Structures*, 86(11):1353–1368, 2008.

[56] K. H. Schweizerhof and P. Wriggers. Consistent linearization for path following methods in nonlinear FE analysis. *Computer Methods in Applied Mechanics and Engineering*, 59(3):261–279, 1986.

[57] M. A. Crisfield. *Non-Linear Finite Element Analysis of Solids and Structures, Volume 1: Essentials*. Wiley, New York, USA, 1991.

[58] J. Shi and M. A. Crisfield. A semi-direct approach for the computation of singular points. *Computer and Structures*, 51(1):107–115, 1994.

[59] M. A. Crisfield. *Non-Linear Finite Element Analysis of Solids and Structures, Volume 2: Advanced Topics*. Wiley, New York, USA, 1997.

[60] N. M. Newmark. A method of computation for structural dynamics. *Journal of the Engineering Mechanics Division*, pages 67–94, 1959.

[61] P. Paultre. *Dynamics of Structures*. Wiley, Hoboken , USA, 2005.

[62] A. K. Chopra. *Dynamics of Structures: Theory and Applications to Earthquake Engineering, Fourth Edition*. Prentice Hall, Upper Saddle River, USA, 2012.

[63] J. Stewart. *Calculus, Fifth Edition*. Thomson, Belmont, USA, 2003.

[64] J. H. Heinbockel. *Introduction to Finite and Infinite Series and Related Topics*. Trafford Pub., Bloomington, USA, 2010.

[65] R. W. Gordon and J. J. Hollkamp. Reduced-order models for acoustic response prediction, AFRL-RB-WP-TR-2011-3040. Technical report, United States Air Force Research Laboratory, Dayton, USA, 2011.

[66] R. A. Perez. *Multiscale reduced order models for the geometrically nonlinear response of complex structures*. PhD thesis, Arizona State University, 2012.

[67] J. J. Hollkamp, P. J. O'Hara, and T. A. Wyen. Modeling damage within a reduced-order model framework: an application. In *Proceedings of the 54th AIAA/ASME/ASCE/AHS/ASC Structures, Structural Dynamics and Materials Conference, Boston, USA*, 2013.

[68] P. J. O'Hara and J. J. Hollkamp. Modeling crack propagation within a reduced-order model framework. In *Proceedings of the 55th AIAA/ASME/ASCE/AHS/ASC Structures, Structural Dynamics and Materials Conference, National Harbor, USA*, 2014.

[69] J.J. Hollkamp, R. A. Perez, and S. M. Spottswood. Design sensitivities of components using nonlinear reduced-order models and complex variables. In *Proceedings of the 35th IMAC, Society for Experimental Mechanics, Orange County, USA*, 2017.